

Local Characterisation of Solid Oxide Fuel Cells

A thesis accepted by the Faculty of Energy Technology, Process Engineering and Biological Engineering of the University of Stuttgart in partial fulfilment of the requirements for the degree of

Doctor of Engineering Sciences (Dr.-Ing.)

by

Caroline Willich

born in Munich

Main referee: Prof. Dr. rer. nat. K. Andreas Friedrich

Co-referee: Prof. Dr.-Ing. Lorenz Singheiser

Date of defence: 16.07.2012

Institute of Thermodynamics and Thermal Engineering

University of Stuttgart

2012

Acknowledgement

I am very glad to have found a multitude of people at the Institute of Technical Thermodynamics of the German Aerospace Center who were interested in my work and supported me in various respects. All these people have contributed in different ways and in different degrees to make the accomplishment of this work possible for me.

I thank my thesis supervisor Prof. Andreas Friedrich for providing the topic of my thesis and the possibility to work in his department. Thanks are also due to Dr. Günter Schiller for the opportunity to work in his group, for supporting me when things got difficult, and for allowing me much scientific freedom. I also thank Prof. Singheiser for co-refereeing the thesis.

I am very grateful to Prof. Wolfgang Bessler for his continuous interest in my work, his valuable scientific advice, many fruitful discussions and good tips that were very helpful for my work. I also thank him for the possibility to work with the software DENIS. Thanks also go to Dr. Stefan Gewies for adapting the model to the segmented setup.

Further I am indebted to Ralf Bähnisch for his help with the measuring technology and Markus Schilder for repeatedly rescuing the test rig computer. I thank Gudrun Steinhilber for preparing the SEM samples, Ina Plock for the SEM pictures and the nice time in the office and Dr. Norbert Wagner for his great advice on impedance spectra.

Special thanks are also due to my colleges and friends Dr. Sebastian Altmann, Alexander Bauder, Stephanie Seidler, Max Eschenbach, Florian Leucht, Moritz Henke, Til Weckesser, Christian Hellwig from the DENIS Help Desk, Zeynep Ilhan, Torsten Knöri, Steffen Wolf, Michael Lang, Corinna Auer and Patric Szabo to name but a few for their helpfulness, for scientific discussions and recreative activities. But also to all my other colleges at the institute who supported me and helped me with their advice, support and cooperation.

“More men are beaten than fail”

„Es gibt mehr Leute, die aufgeben, als solche, die scheitern“

Henry Ford, “My Life and Work”

Contents

Contents	III
Abbreviations.....	VI
Symbols.....	VII
Abstract	X
Zusammenfassung	XII
1 Introduction	1
2 Fundamentals	3
2.1 Definition of a fuel cell.....	3
2.2 Fuel cell types.....	3
2.3 Thermodynamics and electrochemistry	5
2.4 Efficiencies and losses of a fuel cell	6
2.5 SOFC.....	8
2.5.1 Functional principle.....	9
2.5.2 Types of SOFC	9
2.5.3 Materials	10
2.6 Internal reforming.....	12
2.6.1 Steam reforming	13
2.6.2 Partial oxidation (POX)	13
2.6.3 Autothermal reforming	13
2.6.4 Dry reforming	13
2.7 Coking	13
2.8 Sulphur poisoning.....	15
2.9 Nickel oxidation in the anode.....	15
3 Experimental setup	19
3.1 Sealing.....	21
3.2 Cells.....	22

3.3	Gas controlling system	23
3.4	Data logging	23
3.5	Electronic load and average voltage.....	23
3.6	Impedance analyser	24
3.6.1	Impedance spectroscopy.....	24
3.7	Gas chromatograph.....	28
3.8	Reproducibility of setup	28
3.9	Comparison to non-segmented cell.....	28
4	Simulations.....	31
4.1	Gas transport.....	31
4.2	Electrochemistry	32
4.3	Segmentation	36
4.4	Model parameters.....	37
5	H ₂ measurements for the calibration of model parameters.....	39
5.1	Measuring conditions.....	39
5.2	Calibration measurements.....	40
5.2.1	Variation of water content.....	41
5.2.2	Dilution with nitrogen	42
5.2.3	Variation of cathode gas.....	43
5.3	Temperature variations.....	44
5.4	Correlation with model.....	45
5.5	High fuel utilisation	46
5.6	Parameter variations in simulation.....	49
5.6.1	Variation of gas channels	50
5.6.2	Anode thickness	50
5.6.3	Cathode thickness	52
5.6.4	Non-segmented cell.....	54
6	Measurements with CO.....	58

6.1	I-V curves	59
6.2	Comparison of measurements and simulations under CO/CO ₂ conditions	60
6.3	Nickel oxidation at observed plateaus	61
6.3.1	Impedance measurements at the plateau	63
7	Methane as fuel.....	66
7.1	Experiments and simulations.....	66
7.1.1	Carbon deposition.....	66
7.1.2	Current voltage curves.....	67
7.2	Gas composition at OCV - Reforming along the cell	72
7.3	Polarisation	74
7.4	Influence of flow rate and water content.....	76
7.5	Influence flow rate on reforming	78
7.6	Influence of nickel contact net on reforming reaction	79
8	Flow rate and temperature variations.....	80
8.1	Flow rate variations.....	80
8.2	Temperature variations.....	81
8.3	Gas composition	83
8.4	Influence of cell edge.....	84
8.5	Influence of LSCF cathode	88
8.6	Hysteresis	90
8.7	Electrolyte defects	91
9	Cell behaviour under negative voltages	96
10	Obtaining a more even distribution.....	102
11	Summary	103
12	References	105
	Curriculum vitae	109

Abbreviations

1-D	One dimensional
AFC	Alkaline fuel cell
an	Anode
ASC	Anode supported cell
ca	Cathode
CHP	Combined heat and power
CSC	Cathode supported cell
DLR	Deutsches Zentrum für Luft- und Raumfahrt, German Aerospace Centre
DMFC	Direct methanol fuel cell
ESC	Electrolyte supported cell
GDC	Gadolinium doped ceria
H/C ratio	Hydrogen to carbon ratio
i-V curve	Current voltage curve
LSCF	Lanthanum strontium cobalt ferrite
LSM	Strontium-doped lanthanum-manganese-oxide
ma	Mesh anode
mc	Mesh cathode
MCFC	Molten carbonate fuel cell
MEA	Membrane electrolyte assembly
MSC	Metall supported cell
OCV	Open circuit voltage
PAFC	Phosphoric acid fuel cell
ox	Oxidation
PEMFC	Polymer electrolyte membrane fuel cell
POX	Partial oxidation
red	Reduction

S/C ratio	Steam to carbon ratio
SEM	Scanning electron micrograph
SOFC	Solid oxide fuel cell
vol%	Percentage by volume
YDC	Yttria doped ceria
YSZ	Yttria stabilised zirconia

Symbols

α	Activity	[-]
C_D	Double layer capacitance	[F]
E^0	Voltage between two electrodes	[V]
E^{act}	Activation energy	[J/mol]
E_{eq}	Equilibrium voltage	[V]
f	Frequency	[Hz]
F	Faraday constant	[C/mol]
f_u	Fuel utilisation	[-]
i	Current density	[A/cm ²]
I	Current	[A]
$\hat{i}(t)$	Complex alternating current	[A]
i_0	Exchange current density	[A/cm ²]
I_F	Theoretical current	[A]
I_i	Segment current	[A]
i_L	Limiting current density	[A/cm ²]
K	Equilibrium constant of reaction	[-]
$k_{f,ct}^0, k_{r,ct}^0$	Preexponential factor of forward/backward charge transfer reaction	[mol/(m s)]

$k_{r,ct}^0$	Preexponential factor of backward charge transfer reaction	[mol/(m s)]
$k_{f,ct}, k_{r,ct}$	Forward/backward charge transfer reaction rate	[mol/(m s)]
$k_{f,m}, k_{r,m}$	Forward/backward rate constant of surface reactions	[m ⁿ /(mol s)]
m_{fuel}	fuel mass flow	[g/s]
p	Partial pressure	[Pa]
$p_{O_2}^0$	Parameter associated with oxygen reduction	[Pa]
R	Universal gas constant	[J/(mol·K)]
r	resistivity	[Ω cm ²]
R_c	Charge transfer resistance	[Ω]
R_i	Resistors	[-]
R_Ω	Ohmic losses	[Ω]
S_i	Switches	[-]
t	Time	[s]
T	Temperature	[K]
$\hat{u}(t)$	Complex alternating voltage	[V]
U_{cell}	Operating cell voltage	[V]
U_{local}	Local segment voltage	[V]
$V^{\cdot\cdot}$	Interstitial vacancy	[-]
z	number of exchanged electrons	[-]
Z	Impedance	[Ω]
Z'	Real part of impedance	[Ω]
Z''	Imaginary part of impedance	[Ω]
Z_{local}	Local impedance	[Ω]
α	transfer coefficient	[-]
α	Symmetry factor of reaction	[-]
ΔG	molar free enthalpy change	[J/mol]
ΔG^0	Gibbs free enthalpy change	[J/mol]
ΔH	molar enthalpy difference	[J/mol]

ΔH^0_R	Standard molar reaction enthalpy	[J/mol]
ΔS	molar entropy change	[J/(K mol)]
$\Delta\Phi$	Potential difference	[V]
ε	Efficiency	[-]
ε_{th}	Thermodynamic efficiency	[-]
ε_V	Voltage efficiency	[-]
η_{act}	Activation overpotential	[V]
η_{dif}	Diffusion overpotential	[V]
η_{ohm}	Ohmic overpotential	[V]
μ	Chemical potential	[J/mol]
ν	Stoichiometric coefficients	[-]
σ	Conductivity	[S/m]
φ	Electrode potential	[V]
φ	Phase	[°]
Φ	Potential	[V]
ω	Angular frequency	[rad/s]
\square	Free surface site	[-]

Abstract

Fuel cells offer high electrical efficiencies and the solid oxide fuel cell is particularly interesting because easily accessible fuels containing hydrocarbons like natural gas and reformates can be used. Nevertheless the desired high efficiency and high fuel utilisation lead to strong gradients in gas composition along the cell which can in turn lead to lower power densities and increased local degradation.

To better understand the local distribution and its effects a combined experimental and modelling study was done. Segmented planar anode-supported cells were characterised in a setup with 4 x 4 segments and a detailed two-dimensional model representing this setup was developed and validated.

The model was calibrated for hydrogen/nitrogen mixtures with various water contents as well as for reformat gases and internal reforming of methane. A very good agreement between the model and the experiments was achieved. Measurements with CO/CO₂ were done to validate the CO oxidation in the model. Here the influence of very high fuel dilution could also be observed that led to a plateau-like behaviour in the current-voltages curves. This behaviour was attributed to the oxidation of nickel at the anode. Methane reforming leads to an additional variation in gas phase species along the flow path. A great part of the reforming process takes place at the nickel contact mesh and not at the anode of the cell which could be seen in comparison to experiments with a non-catalytic contact mesh. It was also shown that a dilution of the fuel with water or nitrogen can lead to a more homogenous distribution within the cell depending on control parameters.

The model was used to assess the influence of cell parameters. A variation of the gas channels did not show a significant influence. A variation of the electrode thickness showed an increase of power density for thinner electrodes. The model was also used to assess the effect of the segmentation in comparison to a non-segmented cell. A non-segmented cell shows a more even distribution of voltage and a greater variance of current density while the gas composition along the flow path is similar for segmented and unsegmented cells. The validated model can be used further to estimate optimal and critical operating parameters.

Through a variation of fuel flow rate and temperature the influence on gas composition along the cell and differences in fuel distribution at the side and in the middle of the flow field could be seen as well as its influence on cell performance. Higher load and higher temperatures lead to a stronger decrease of fuel along the cell. The segments located at the side of the cell showed a different performance than those in the middle, due to an unequal distribution of the fuel into the flow field. This influence increases with lower flow rates. During these

experiments a correlation between poor local performance and electrolyte defects as well as local nickel oxidation at the anode was observed. It was also shown that extreme local conditions can lastingly damage the cell and local distributions have to be taken into account for stack development.

Zusammenfassung

Festelektrolytbrennstoffzellen haben hohe elektrische Wirkungsgrade und bieten zudem den Vorteil, dass Kohlenwasserstoffe z. B. aus Erdgas oder Reformatgasen als Brenngase verwendet werden können. Diese Brenngase haben den Vorteil, dass die Verfügbarkeit hoch ist. Allerdings führen die erwünschten hohen Wirkungsgrade und Brenngasnutzungen zu starken Gradienten in der Brenngaszusammensetzung entlang der Zelle, was wiederum zu niedrigen Leistungsdichten und erhöhter lokaler Degradation führen kann.

Um die lokale Verteilung und ihre Auswirkungen besser zu verstehen, wurde in dieser Arbeit ein kombinierter Ansatz aus Experimenten und Modellierung gewählt. Segmentierte, planare, anodengetragene Zellen wurden in einem Aufbau mit 4 x 4 Segmenten charakterisiert und ein detailliertes zweidimensionales Modell dieses Aufbaus entwickelt und validiert. Das Modell wurde für Wasserstoff/Stickstoff Mischungen mit verschiedenen Wassergehalten sowie für Reformatgase und interne Reformierung von Methan kalibriert. Eine gute Übereinstimmung zwischen Modell und Experiment wurde erreicht.

Messungen mit CO/CO₂ wurden durchgeführt um die CO Oxidation im Modell zu validieren. Dabei konnte auch der Einfluss einer starken Verdünnung des Brenngases beobachtet werden, was zu einem Plateau in der Strom-Spannungskurve führte. Dieses Verhalten wurde auf die Oxidation von Nickel an der Anode zurückgeführt.

Die interne Reformierung von Methan führt zu einer zusätzlichen Änderung der Gaszusammensetzung entlang des Strömungswegs. Ein Großteil der Reformierung findet am Nickelkontaktnetz und nicht an der Anode selbst statt. Dies konnte im Vergleich mit Versuchen mit einem nicht-katalytischen Kontaktnetz beobachtet werden. Es wurde außerdem gezeigt, dass eine Verdünnung des Brenngases mit Wasser oder Stickstoff je nach Kontrollparameter zu einer gleichmäßigeren Verteilung entlang der Zelle führen kann.

Das Modell wurde weiterhin verwendet, um den Einfluss verschiedener Zellparameter zu untersuchen. Eine Änderung der Größe der Gaskanäle zeigte keine signifikanten Auswirkungen. Die Änderung der Elektrodendicke führte zu einer höheren Leistungsdichte für dünnere Elektroden. Das Modell wurde außerdem verwendet, um den Einfluss der Segmentierung im Vergleich mit einer nicht-segmentierten Zelle zu untersuchen. Eine nicht-segmentierte Zelle weist eine gleichmäßigere Verteilung der Spannung und einen stärkeren Gradienten in der Stromdichte aus, während die Gaszusammensetzung entlang des Strömungsweg für segmentierte und nicht-segmentierte Zellen ähnlich ist. Das validierte Modell kann für weitere Untersuchungen der optimalen und kritischen Betriebsbedingungen verwendet werden.

Durch die Variation der Brenngasflussrate und der Temperatur wurde der Einfluss auf die Gaszusammensetzung entlang der Zelle, Unterschiede in der Gasverteilung am Rand und in der Mitte des Strömungsfeldes, sowie der Einfluss auf die Zelleistung sichtbar. Eine größere Last und höhere Temperaturen führen zu einer stärkeren Abnahme des Brenngases entlang der Zelle. Die Segmente an der Seite der Zelle zeigten aufgrund einer ungleichen Gasverteilung ein anderes Verhalten als die in der Mitte. Dieser Unterschied nimmt mit sinkenden Durchflüssen zu. Während dieser Versuche wurde ein Zusammenhang zwischen niedriger lokaler Leistung, Elektrolytdefekten und lokaler Nickeloxidation in der Anode beobachtet. Es wurde außerdem gezeigt, dass extreme lokale Bedingungen wie lokal negative Spannungen die Zelle dauerhaft schädigen und lokale Verteilungen von Strom, Spannung und Brenngaszusammensetzung bei der Stackentwicklung berücksichtigt werden müssen.

1 Introduction

The solid oxide fuel cell (SOFC) is a high temperature ceramic fuel cell. It has the advantage compared to other types of fuel cells that not only hydrogen can be used as fuel but also fuels containing hydrocarbons like natural gas, biogas or reformat gases. An infrastructure for the distribution of these fuels already exists which facilitates an introduction of the technology. Because of the high operating temperature SOFCs may be used in stationary applications for decentralised combined heat and power but also in mobile applications.

For the commercial use of fuel cells a high electrical efficiency and a sufficient life-time of the cells are necessary. A high fuel utilisation is required, that is, ideally the entire fuel should be converted electrochemically in the cell. Under these technically relevant operating conditions, that is high power densities and high fuel utilisation, planar solid oxide fuel cells show a spatially inhomogeneous distribution of the electrochemical performance. There is a strong variation of gas composition along the flow path due to the successive consumption of the fuel and dilution by reaction products. This in turn leads to an inhomogeneous distribution of current density, voltage and temperature. These local conditions can be expected to contribute significantly to accelerated electrode degradation, thermomechanical stresses and reduced efficiency. If reformat gases or methane-steam mixtures are used as fuel, water-gas shift and reforming reactions at the anode are coupled to diffusive and convective transport processes, leading to a variation of temperature and gas-phase species along the flow channel and through the anode thickness.

To improve the understanding of the local effects, detailed information about the spatial distribution of the chemical and electrical cell properties is necessary. Very few spatially resolved measurements have yet been done for SOFC mainly due to the difficulties the elevated operating temperatures present. The conditions measured in a segmented setup do not correspond directly to those in a non-segmented setup, still, if the differences are kept in mind, the obtained information is valuable for improving cell, stack and flow field designs. Mathematical models can often help to understand experimental results and provide an insight into non-measurable quantities, as for example the distribution of current and gases within the porous electrodes. These distributions can have important effects on performance and degradation behaviour of the cell. It also offers the possibility to assess the influence the segmentation has in comparison to a non-segmented cell and is therefore useful in improving cell and stack design.

In this thesis a combined experimental and modelling study of the spatially resolved performance of a planar segmented SOFC was performed. A planar anode-supported SOFC

single cell was locally characterised in a 4x4 segmented cell arrangement and a detailed two-dimensional elementary kinetic electrochemical model representing the segmented cell setup along the flow path and through the thickness of the membrane-electrode assembly and interconnector was developed and validated. This model was then used to interpret and predict the local behaviour and conditions of the cell.

At first the model was validated for measurements with hydrogen/nitrogen mixtures as this is the least problematic fuel in the SOFC since only the cell reaction takes place at the anode and no depositions of carbon can occur. Then successively other fuels were used. First carbon monoxide which is contained in natural gas and in reformat gas. Afterwards the model was also validated for methane-steam mixtures where not only the oxidation of fuel, but also steam reforming and water-gas-shift reactions take place at the anode.

Furthermore, a variation of flow rate and temperature was performed to assess the influence on the gas composition along the cell and differences in the fuel distribution at the side and in the middle of the flow field and its influence on cell performance. The last chapter examines the local degradation under extreme operating conditions.

2 Fundamentals

In this chapter the principle of a fuel cell is explained. Different fuel cell types are shortly presented and the main aspects of thermodynamics and electrochemistry are described. Afterwards the functional principle of solid oxide fuel cells (SOFC), their different forms and the standard materials are presented.

2.1 Definition of a fuel cell

Fuel cells convert chemical energy directly into electrical energy. A typical fuel cell consists of an electrolyte, the anode and the cathode as shown in Figure 2-1. The fuel and oxidant are continuously fed to the respective sides where they react electrochemically. The electrolyte separates the two gas phases and is ion conducting. At the anode the fuel is oxidised and electrons are set free, which can pass through the external circuit towards the cathode where the oxidant is reduced.

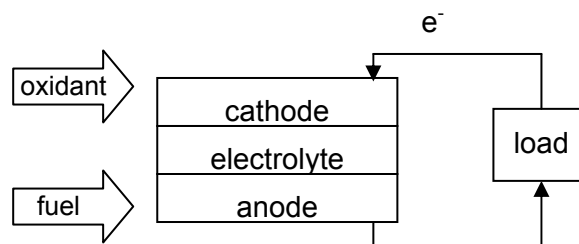


Figure 2-1: Scheme of a fuel cell

The conversion of energy in a fuel cell does not include a conversion into thermal energy and is therefore not limited by the efficiency of a Carnot-cycle, thus high theoretical efficiencies can be achieved.

2.2 Fuel cell types

There are different types of fuel cells which can be classified by the operating temperature, the electrolyte or the charge carriers.

- The alkaline fuel cell (AFC) is operated at temperatures below 100 °C. Hydrogen is used as fuel. Both air and fuel have to be free from CO₂. The electrolyte is aqueous

alkaline solution, such as potassium hydroxide (KOH) and the charge carriers through the electrolyte are OH^- ions. Platinum is used as catalyst. This type of fuel cell was used in space vehicles like Apollo.

- The polymer electrolyte membrane fuel cell (PEMFC) is operated at temperatures between 60 – 100 °C. Pure hydrogen is required as fuel. The electrolyte is a proton conducting polymer membrane and the charge carriers through the electrolyte are H^+ ions. It uses platinum as catalyst. It is suitable for vehicles and mobile applications and even for low power combined heat and power (CHP) systems.
- The direct methanol fuel cell (DMFC) is a PEMFC, but uses methanol as a fuel. The operating temperature ranges from 20 to 90 °C. It is suitable for portable electronic systems of low power.
- The phosphoric acid fuel cell (PAFC) is operated at temperatures around 220 °C. It also uses pure hydrogen as fuel. The electrolyte is concentrated phosphoric acid and the charge carriers are H^+ ions. Platinum is used as catalyst. Its development is very advanced and it was the first commercially available fuel cell for 200 kW CHP systems.
- The molten carbonate fuel cell (MCFC) is operated at temperatures around 650 °C. Reformate gases containing CO_2 are used as fuel. The electrolyte consists of molten alkali carbonate and the charge carriers through the electrolyte are CO_3^{2-} ions. It needs CO_2 for operation. Due to the high operating temperatures it does not need platinum as catalyst but uses the far cheaper nickel. It is suitable for CHP systems with medium to large (MW) capacities.
- The solid oxide fuel cell (SOFC) is operated at 600 to 1000 °C [1]. Hydrogen as well as CO and hydrocarbons can be used as fuel. The charge carriers are O^{2-} ions. It will be further described in chapter 2.5. It is suitable for CHP systems up to several MW and also for some mobile applications.

High temperature fuel cells (SOFC and MCFC) have the advantage that hydrocarbons like methane can be reformed internally into hydrogen and carbon monoxide. Of course the high operating temperature brings additional challenges and has an influence on the efficiency, the cell design and the materials used for the periphery [1].

2.3 Thermodynamics and electrochemistry

In the following chapter the fundamental electrochemical mechanisms and thermodynamics of a fuel cell are summarised.

The overall reaction in a fuel cell consists of the partial reactions at the anode and the cathode. Because of the partial reactions at anode and cathode different chemical potentials are formed at the electrodes. This difference in potential results in an electrical voltage E^0 between the electrodes, which is the electromotoric force moving the charge carriers between the electrodes, where φ is the potential at the respective electrodes.

$$E^0 = \varphi_{\text{cathode}} - \varphi_{\text{anode}} \quad (2-1)$$

Potentials can only be measured in relation to another potential, which is why standard potentials of different reaction are always given with respect to the hydrogen potential at a platinum electrode. These standard potentials can be found in tables in literature. The higher the standard potential of a reaction is the more energy is needed for oxidation. Table 2-1 shows the half cell reactions and the corresponding standard potentials for a hydrogen-oxygen cell.

Reaction	Standard potential / V
$2\text{H}^+ + 2\text{e}^- \rightleftharpoons \text{H}_2$	0
$\text{O}_2 + 4\text{H}^+ + 4\text{e}^- \rightleftharpoons 2\text{H}_2\text{O}$	1.229

Table 2-1: Standard potentials of a fuel cell reaction

The total cell reaction consists of the two half cell reactions at the anode and at the cathode, so the potential of a hydrogen/nitrogen cell under standard conditions is:

$$E^0 = 1.23 \text{ V} - 0 \text{ V} = 1.23 \text{ V}$$

The theoretical maximum of the electrical work that can be obtained from a chemical reaction is given by the Gibbs free enthalpy ΔG^0 .

$$\Delta G^0 = -zFE^0 \quad (2-2)$$

Here F is the Faraday constant and z the number of exchanged electrons.

The theoretical equilibrium voltage E_{eq} of a fuel cell depends also on the concentration of the reactants and the temperature. The Nernst equation describes this dependence.

$$E_{eq} = E^0 + \frac{RT}{nF} \ln \frac{\prod a_{ox}^{\nu}}{\prod a_{red}^{\nu}} \quad (2-3)$$

Here ν are the corresponding stoichiometric coefficients of the reaction. For gaseous fuels the activity a can be replaced by the partial pressure p of each gas [1, 2] .

2.4 Efficiencies and losses of a fuel cell

The thermodynamic efficiency ε_{th} is given by the relation between the free enthalpy change ΔG of the cell reaction which is the maximum that can be transformed into electrical work and the maximum available thermal energy ΔH .

$$\varepsilon_{th} = \frac{\Delta G}{\Delta H} = \frac{\Delta H - T\Delta S}{\Delta H} = 1 - \frac{T\Delta S}{\Delta H} \quad (2-4)$$

This efficiency is not reached in reality. For instance, when only part of the fuel is used during operation of the cell, it follows that the resulting current I is lower than the theoretical current I_F , which is given by Faraday's law. The fuel utilisation f_u can be calculated using the mass flow of fuel entering and leaving the cell ($m_{fuel,out}$ and $m_{fuel,in}$) or by using the molar flow rate \dot{n} and the number of exchanged electrons z .

$$f_u = 1 - \frac{m_{fuel,out}}{m_{fuel,in}} = \frac{I}{I_F} = \frac{I}{\dot{n} \cdot z \cdot F} \quad (2-5)$$

In a real fuel cell the open circuit voltage (OCV) also is lower than the theoretical value E_{eq} . Reasons for this difference are for example internal currents and a non-ideal impermeability of the electrolyte.

As soon as a current is drawn, the voltage of the cell drops as can be seen in Figure 2-2 which shows a characteristic current voltage curve of a fuel cell.

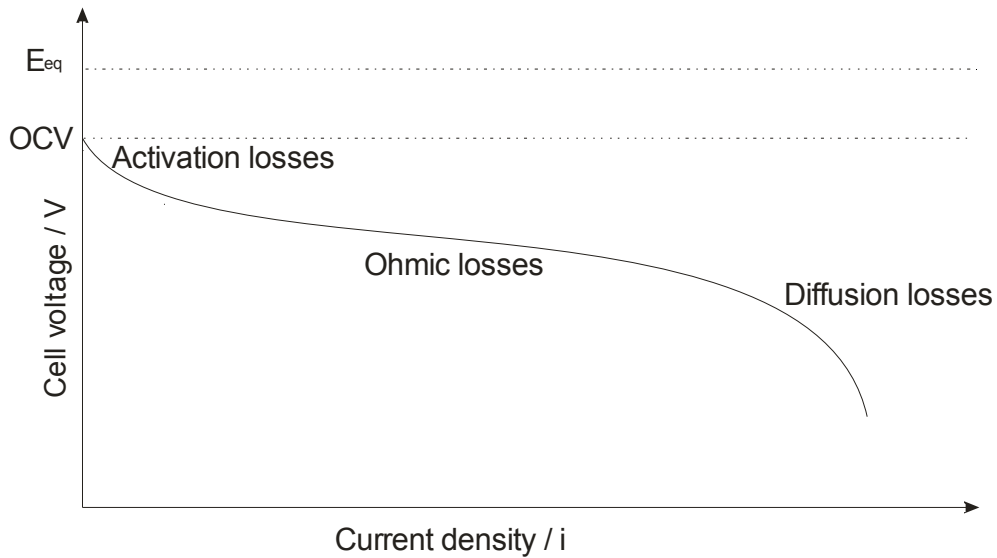


Figure 2-2: Schematic current-voltage characteristic of a fuel cell

The voltage efficiency ε_v is defined as the ratio between the operating cell voltage U_{cell} under load and the theoretic equilibrium voltage E_{eq} .

$$\varepsilon_v = \frac{U_{\text{cell}}}{E_{\text{eq}}} \quad (2-6)$$

The total efficiency ε of the cell is given by the product of the thermodynamic efficiency ε_{th} , the voltage efficiency ε_v and the fuel utilisation f_u [3].

$$\varepsilon = \varepsilon_{\text{th}} \cdot \varepsilon_v \cdot f_u \quad (2-7)$$

It can be seen in Figure 2-2 that at small current densities the voltage drop is exponential and the losses dominant in this region are referred to as activation polarisation or charge transfer polarisation. This loss is due to the activation energy of the electrochemical reaction and the transfer of the electrons to or from the electrode. The relationship between the current density i and the voltage drop η_{act} at one electrode-electrolyte interface is given by the Butler-Volmer equation. The exchange current density i_0 increases with temperature, which explains why the activation losses are smaller in high temperature fuel cells than in low temperature cell [1].

$$i = i_0 \left(\exp\left(\alpha_1 \frac{F}{RT} \eta_{act}\right) - \exp\left(\alpha_2 \frac{F}{RT} \eta_{act}\right) \right) \quad (2-8)$$

α_1 and α_2 are the reduction and oxidation transfer coefficients of the electron transfer at the interface [4] and η_{act} the activation overvoltage.

The linear part of the curve is dominated by ohmic losses in the cell and current conductor. These losses are proportional to the current density i , r being the ohmic resistivity.

$$\eta_{ohm} = i \cdot r \quad (2-9)$$

At high current densities the voltage drops again exponentially. This concentration polarisation is determined by mass transport to and from the electrodes. If the reaction at the electrodes is faster than the transport of reactants and products the concentration of fuel at the electrode drops. This overpotential η_{diff} can be described by (2-10) where i_L is the limiting current density which depends on the diffusion coefficient or the reactants, their concentration and the thickness of the diffusion layer [2].

$$\eta_{diff} = \frac{RT}{zF} \cdot \ln\left(1 - \frac{i}{i_L}\right) \quad (2-10)$$

The single losses of the cell under load sum up to the total loss of the cell.

2.5 SOFC

The Solid Oxide Fuel Cell (SOFC) is a high temperature fuel cell. Operating temperatures vary between 600 °C and 1000°C. Efforts are being made to reduce the temperature. SOFCs may be used in stationary applications for decentralised combined heat and power but also in mobile applications.

A great advantage of SOFC in comparison with other types of fuel cells are that the elevated temperatures and the materials used make internal reforming possible and gaseous hydrocarbons can be used as fuel. It also does not need an expensive catalyst like platinum as low temperature fuel cells do. Another advantage compared to low temperature fuel cells is that CO does not poison the anode but is a fuel and is oxidised at the anode. A removal of CO from the fuel gas is therefore not necessary.

Difficulties arise because of the high temperatures. All materials have to be physically and chemically stable at operating temperatures and the coefficients of expansion of the different

materials must match to avoid fracturing of the cell. The sealing of the components is another challenge. Glass or solder sealing may be used for stack sealing.

2.5.1 Functional principle

In SOFC O^{2-} ions are the charge carriers that pass through the electrolyte as shown schematically in Figure 2-3. At the cathode oxygen is reduced and negatively charged oxygen ions are formed which then pass through the electrolyte.



At the anode side the fuel gas (H_2 or CO) reacts with the oxygen ions and water or respectively CO_2 is formed.



The surplus electrons pass through the external circuit.

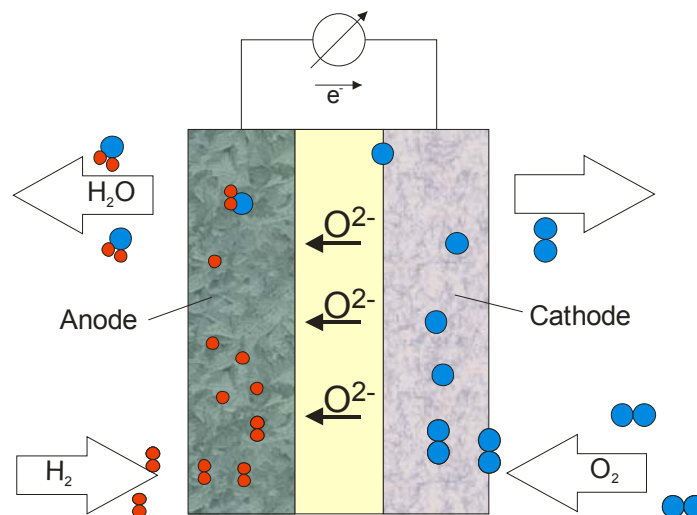


Figure 2-3: Principle of an SOFC

2.5.2 Types of SOFC

The active layers of the cell should be very thin to reduce resistances. Therefore some kind of support is needed to give the necessary mechanical strength to the cell. Several configurations are possible.

Anode supported cells (ASC) consist of a thick anode that is usually subdivided into a substrate giving the mechanical stability and a functional layer. The substrate usually has a higher porosity than the functional layer but consist of the same material. The development of this type is the most advanced and ASC are widely used. They are usually fabricated via tape casting and subsequent sintering and screen printing.

Electrolyte supported cells (ESC) have a thick electrolyte that gives mechanical strength to the cell. The thick electrolyte leads to higher ohmic resistances within the cell but due to the thin electrode the reacting gases are easily supplied to the functional layers.

In cathode supported cells (CSC) a thick cathode gives the required stability. This type was used in the Siemens concept of tubular cells.

In metal supported cells (MSC) the functional layers are applied onto a porous metal support. This makes it possible to keep all functional layers thin. MSC offer a better resistance to thermal and redox cycles. The development is not as advanced as for the other cell types and they reach lower power densities than ASC. At DLR such cells are produced via plasma spraying.

2.5.3 *Materials*

Below the materials of the different components are described. To get a high performance a high conductivity of the materials is needed. All materials used have to have a high chemical and physical stability to endure the reducing or oxidising atmospheres and strains due to thermal cycling or external mechanical stress. The expansion coefficients of the different materials have to be similar in order not to destroy the cell when temperature changes take place as in the initial heating or during thermo cycles. The materials also have to be chemically compatible with other components in the system.

2.5.3.1 *Electrolyte*

The electrolyte must be ion conducting and has to electrically separate the cathode and the anode. It therefore needs high ion conductivity and the electron conductivity needs to be as small as possible. The electrolyte needs to be thin to keep the ohmic resistance low. The thickness depends on the manner of fabrication of the cell. Furthermore the electrolyte has to be gas-tight to separate the reactants from each other.

The usual material for the electrolyte is yttria-stabilised zirconia (YSZ) consisting of zirconia (ZrO_2) with 8 mol% of yttria (Y_2O_3). The ion conductivity of pure ZrO_2 is low. The doping with Y_2O_3 creates oxygen vacancies in the lattice causing a higher conductivity for O^{2-} ions by

replacing Zr^{4+} ions with Y^{3+} ions [5]. Yttria also stabilises the cubic structure at room temperatures [6]. The ion conductivity of zirconium oxide is influenced by the doping material and its amount. YSZ has a maximum ion conductivity at an yttria concentration of 8 mol% [7].

2.5.3.2 Anode

At the anode the reforming reaction as well as the oxidation of hydrogen and carbon monoxide takes place. The anode must contain a catalyst for those reactions. The electrons and the O^{2-} -ions have to reunite so that good electron conductivity as well as high ion conductivity is required. The anode is exposed to a reducing atmosphere and high temperatures. Anode material therefore must have a very good chemical and thermal stability under those conditions. Research also aims at improving the tolerance of impurities in the anode gas and improving the lifetime.

A porous mixture of YSZ and nickel is commonly used for the anode which is referred to as cermet (ceramic and metal). The YSZ forms a porous matrix in which nickel particles are embedded. The YSZ secures the ion conductivity while nickel is electron conducting and is also a catalyst for the reforming as well as the cell reaction. The cell reaction takes place at the so called triple phase boundary where ions, electrons and gas phase meet. The porous structure of the anode enlarges the triple phase boundary so that the reaction can take place within the structure and not only at the interface of electrolyte and anode.

The conductivity of a mixture of two components with different conductivities may change dramatically once the fraction of one component is above the percolation limit. If the nickel content is below that value the transport of the electrons is inhibited since the nickel particles have no connection amongst themselves and the current collector. The resistance also increases if the content of YSZ is too small. The conductivity of the anode cermet changes strongly when the nickel content is between 20 vol% and 30 vol% [8]. The value also depends on the diameter of the particles.

At the high operating conditions of SOFC the nickel particles start sintering reducing the power of the cell. A fine structure of the YSZ matrix helps to reduce the sintering of the nickel particles and adapts the expansion coefficient of the anode to that of the electrolyte.

The anode is fabricated using nickel oxide which is reduced to nickel prior to the first operation of the cell. The volume of nickel oxide is about 51 vol% greater than the volume of nickel [9]. Due to the volume change the porosity is increased.

2.5.3.3 Cathode

The cathode material has to be a catalyst for the reduction of oxygen and a good ion as well as electric conductivity is needed.

The material most widely used is strontium-doped lanthanum-manganese-oxide (LaSrMnO_3) which is referred to as LSM. It has a perovskite-type structure and is an electronic conductor. The doping with strontium improves the electrical conductivity. To achieve a sufficient triple phase boundary and sufficient ion conductivity, a porous mixture of LSM and YSZ is used enabling the transport of ions and electrons. The mixture also helps adapting the different coefficients of thermal expansion [10].

The other material that is currently prevalent is lanthanum strontium cobalt ferrite (LSCF), also a perovskite, which is a mixed ion and electronic conductor. This improves the performance in comparison to LSM cathodes leading to a higher power density in SOFC with LSCF cathodes. LSCF can react with the electrolyte material which is why cells with a LSCF cathode usually have an additional layer between cathode and electrolyte made of yttria doped ceria (YDC) or gadolinium doped ceria (GDC) to inhibit a rapid degradation of the cell.

2.6 Internal reforming

An advantage of SOFC in comparison with other fuel cells is the possibility to use not only hydrogen as a fuel but also fuels containing hydrocarbons e.g. methane or methanol. These can either be prereformed (external reforming) or because of the elevated operating temperatures of SOFC these hydrocarbons can be internally reformed in the cell. An external reformer is not necessary in this case.

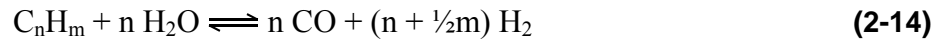
There is a difference between direct and indirect internal reforming. During indirect internal reforming the fuel is reformed before it enters the cell. The area where the reforming takes place and the cell are thermally connected, and the surplus heat of the fuel cell is used for the endothermic reforming. During direct internal reforming the reforming reaction takes place directly at the cell and is catalysed by the nickel in the anode. Tanaka and Kato state the temperature for the reforming of hydrocarbons in an SOFC to be above 650°C [11].

The internal reforming of methane (CH_4) is of great interest, since it is the main component of natural gas and biogas. The availability is therefore good and an infrastructure for its distribution already exists.

Subsequently, the possible reforming mechanisms are explained. For external reforming all of them are applicable, for internal reforming only steam reforming and to a certain extent dry reforming is used.

2.6.1 Steam reforming

The most important reaction for the reforming of hydrocarbons is the steam reforming reaction. In the steam reforming process hydrocarbons react with steam to give a hydrogen and carbon monoxide rich synthesis gas. The reaction is endothermic and at high temperatures the equilibrium is on the side of the products. For methane the standard reaction enthalpy ΔH_R^0 is 206 kJ/mol [12] at 293.15 K and 1.013 bar.

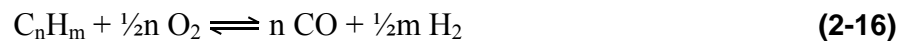


The CO produced can react further in the water-gas shift reaction. This increases the hydrogen yield of the reforming process. The water-gas shift reaction is slightly exothermic and takes place at lower temperatures [12].



2.6.2 Partial oxidation (POX)

Partial oxidation is the substoichiometric partial combustion of a fuel. It is an exothermic reaction. For methane the reaction enthalpy ΔH_R^0 is -37 kJ/mol [13].



2.6.3 Autothermal reforming

The autothermal reforming reaction is a combination of the two reactions mentioned above. The exothermic partial oxidation process can supply the heat required for the steam reforming reaction [14].

2.6.4 Dry reforming

Another way of reforming CH_4 is by adding CO_2 [15, 16]. The reaction (2-17) by which CO and H_2 is formed is endothermic



2.7 Coking

A difficulty that might arise from the internal reforming of methane or other hydrocarbons is the deposition of solid carbon at the anode.

The carbon can be deposited on the surface of the anode blocking the gas diffusion paths and can also lead to irreversible degradation of the anode by the formation of Ni carbides inactivating the catalyst or lead to the mechanical destruction of the anode when carbon settles between Ni and YSZ [17].

Carbon deposition happens at low water contents via the Boudouard reaction (2-18) [18]



or via the cracking reaction of methane (2-19)



Cracking happens at temperatures above 600°C while the Boudouard reaction is favoured at lower temperatures [9].

The formation of carbon depends on the chemical equilibrium of the fuel gas at the given conditions. Therefore the important parameters are the composition of the fuel gas and the temperature [17] on which the equilibrium strongly depends. The risk for carbon deposition at equilibrium for different gas compositions and temperatures can be rated from C-H-O ternary phase diagrams as shown by [19] or calculated with the help of thermodynamic data. In this thesis calculations were done with the CANTERA software package [20] to appraise the risk of carbon formation for the chosen measurement conditions.

Carbon deposition at the fuel cell can be prevented by adding sufficient water in the fuel gas. The water content is either given by the H/C ratio which is the hydrogen atoms in relation to the carbon atoms, or by the S/C ratio which is the steam to carbon ratio.

Pressure also has an influence on the formation of solid carbon. A decrease of partial pressure can shift the critical temperature to a lower value [21], which is why a dilution of the gas with an inert gas like nitrogen can help to avoid carbon formation.

The velocity of the reactions at a given temperature also has an effect on the formation of carbon in the cell. If the reaction rate is slow it inhibits the formation of coke. Timmermann et al. found the coke formation to be one order of magnitude lower in experiments than in thermodynamic equilibrium [17]. For example the Boudouard reaction (2-18) is slow at room temperatures which is why CO may be regarded as semi-stable at room temperature [18].

2.8 Sulphur poisoning

Natural gas and bio gas contain sulphur which is a catalyst poison for SOFC anodes. H_2S is adsorbed on the nickel surface and by forming Ni_3S_2 it inhibits the catalytic activity of nickel. Anode poisoning starts at contents smaller than 1 ppm [22]. The performance loss caused by sulphur poisoning is reversible at low H_2S contents but becomes irreversible at higher concentrations over 100 ppm [23]. To avoid damage to the cell sulphur has to be removed before the gas is used in an SOFC. There is also research going on to find more sulphur tolerant materials for the anode. In this work only synthetic gases without sulphur impurities are used, so that no sulphur poisoning can occur.

2.9 Nickel oxidation in the anode

A reoxidation of nickel in the anode can seriously damage the cell. The volume of nickel oxide is about 51 vol % greater than the volume of nickel. The ceramic structure of the anode in which the nickel is imbedded does not change its volume under the different atmosphere. If there is not enough room for the volume change during nickel oxidation the YSZ matrix can be destroyed and cracks appear in the anode and/or the electrolyte. Conductive nickel pathways in the anode are thus destroyed and the conductivity of the anode is thereby reduced [9]. Nickel oxide is an inferior electronic conductor and represents an extra resistance within the cell. Nevertheless nickel oxidation does not lead immediately to the destruction of the cell. Sarantaridis et al. states that up to 3% of oxidation can be recovered by subsequent reduction without damage to the cell [24]. It can even improve the performance of the cell. The risk for cracking also depends on the housing of the cell. If there are no external constraints that inhibit the change in volume the cell can support higher percentages of nickel oxide up to 75%. A non uniform oxidation increases the risk for cell destruction. Sarantaridis et al. found a particularly strong oxidation in regions of the cell where the contact to the current collector was good which was mainly in the middle of the cell [24]. The risk of cell destruction because of reoxidation of the anode can be reduced by a very fine porous structure and slow oxidation [9].

Nickel oxidation may happen during a shut down of the system or during operation when oxygen reaches the anode from the outside through a leak in the sealing or the electrolyte. If the cell is no longer supplied with sufficient fuel the nickel in the anode is oxidised electrochemically. This effect occurs in the case of fuel starvation.

Nickel oxidation is an important aspect for the local characterisation of SOFC since a local gradient in gas composition might lead to local fuel starvation and consequently to locally oxidising conditions.

In literature, e.g. Sarantaridis et al. and Nehter [24, 25] it is generally assumed that nickel oxidation occurs once the voltage of the cell is below that of the nickel oxidation potential which corresponds to the OCV a cell would have if no fuel is fed to the anode. The OCV of the cell is then determined by the equilibrium of the nickel oxidation reaction which is given in equation (2-20) [24].



The theoretical OCV for the absence of fuel can be calculated by equation (2-21) [24].

$$\text{OCV} = \frac{RT}{2F} \ln \frac{\sqrt{p_{\text{O}_2, \text{cathode}}}}{\sqrt{p_{\text{O}_2, \text{anode}}}} \quad (2-21)$$

$p_{\text{O}_2, \text{cathode}}$ is given by the gas composition on the cathode; $p_{\text{O}_2, \text{anode}}$ can be calculated from the equilibrium constant K of the reaction using equation (2-22).

$$K = \exp\left(\frac{-\Delta G}{RT}\right) = \sqrt{\frac{1}{p_{\text{O}_2, \text{anode}}}} \quad (2-22)$$

ΔG may be obtained from the chemical potentials μ of the reactants as in equation (2-23) [2]

$$\Delta G = \mu_{\text{NiO}} - \mu_{\text{Ni}} - 0.5\mu_{\text{O}_2} \quad (2-23)$$

With the chemical potentials taken from equations (2-24) to (2-26) [26, 27] the nickel oxidation potential can be calculated.

$$\mu_{\text{Ni}} = -29.87 \frac{\text{J}}{\text{mol} \cdot \text{K}} \cdot (T - 298.15\text{K}) \quad (2-24)$$

$$\mu_{\text{NiO}} = -211.71 \frac{\text{kJ}}{\text{mol}} - 37.99 \frac{\text{J}}{\text{mol} \cdot \text{K}} (T - 298.15\text{K}) \quad (2-25)$$

$$\mu_{\text{O}_2} = -205.02 \frac{\text{J}}{\text{mol} \cdot \text{K}} \cdot (T - 298.15\text{K}) \quad (2-26)$$

Figure 2-4 shows the resulting nickel oxidation potential for temperatures between 600 °C and 900°C. A lower temperature increases the risk for nickel oxidation; higher temperatures reduce the risk. For 800°C the nickel oxidation potential is 0.679 V as is marked in blue in Figure 2-4.

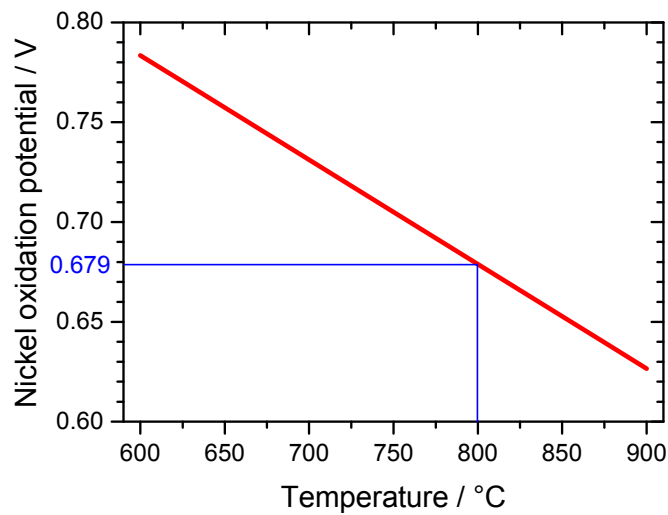


Figure 2-4: Theoretical nickel oxidation potential over temperature at ambient pressure

The risk for nickel oxidation due to the surrounding gas composition may also be taken from the Ellingham diagram shown in Figure 2-5. The H_2/H_2O , the CO/CO_2 ratios and the partial pressure of oxygen that lead to oxidation of nickel can be seen in the diagram. The lines represent the boundaries between oxidising and reducing conditions. Above the lines oxide is formed. To determine e.g. the limit H_2/H_2O ratio at $800^\circ C$ the point on the nickel-nickel oxide line corresponding to $800^\circ C$ is connected to the point denominated H on the left scale. The intersection of this connecting line (blue) with the H_2/H_2O scale gives the sought ratio with a value of 10^{-2} . For the CO/CO_2 ratio the proceeding is the same but the point C on the left-hand scale is used instead of H (red line). For the O_2 pressure the point in the upper left corner is used.

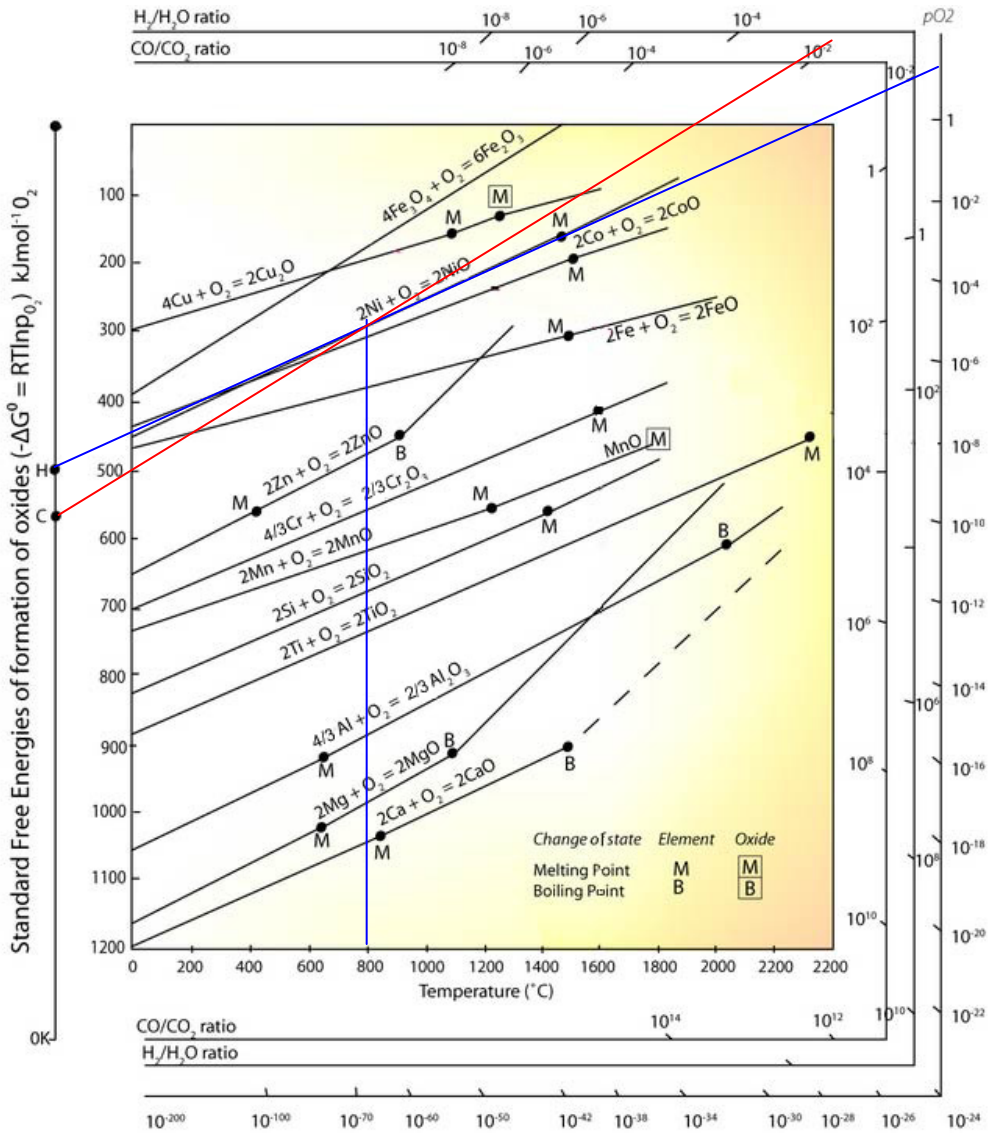


Figure 2-5: Ellingham diagram [28, 29]

3 Experimental setup

The setup used for the experiments allows for integral as well as spatially resolved measurements of current density and voltage, the local and integral determination of impedance data, the local measurement of temperature and the spatially resolved analysis of the fuel gas concentrations along the flow path.

Two test rigs were used for the measurements. They differ in the geometries of the cell and gas channels, as well as in the segmentation. The cell geometries are shown schematically in Figure 3-1. On the left a square shaped cell can be seen. The setup in which this geometry is used will be referred to as the square design, while the setup for the rectangular cell on the right side will be referred to as the cassette design, because it is modelled after the cassettes that are used in stacks.

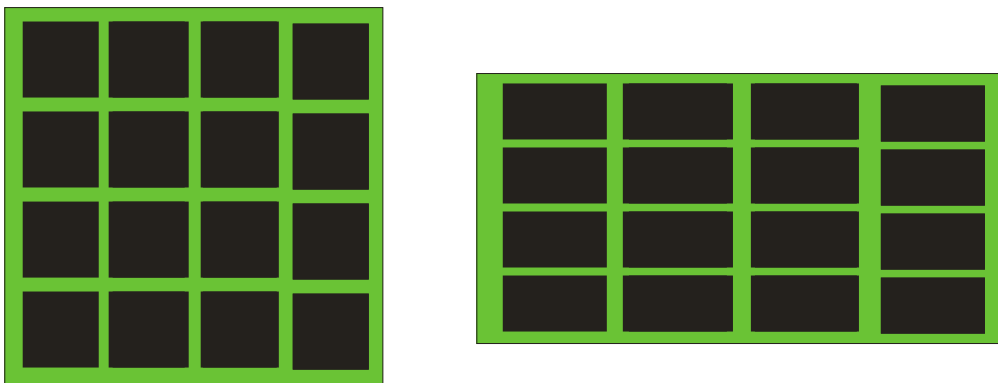


Figure 3-1: Scheme of the two segmented cell designs

In both setups the cells have a total area of 100 cm^2 and the cathode of the anode-supported cells is divided into 16 segments. In the case of the square cells each segment has an active area of 4.84 cm^2 , while the cassette design cells have got segments with an active area of 3.78 cm^2 each.

The cells are mounted in a metallic housing (Crofer 22APU) and sealed with glass seal. The housing has 16 galvanically isolated segments that include the flow field on the cathode side. The setup for the square cells also has 16 galvanically isolated segments on the anode side, which makes it possible to use also electrolyte supported cells with segmented electrodes on both sides. The cassette design has no anodic segmentation, since that test bench is only used for anode or metal supported cells in which case an anodic segmentation is superfluous. A schematic cross section of both setups can be seen in Figure 3-2.

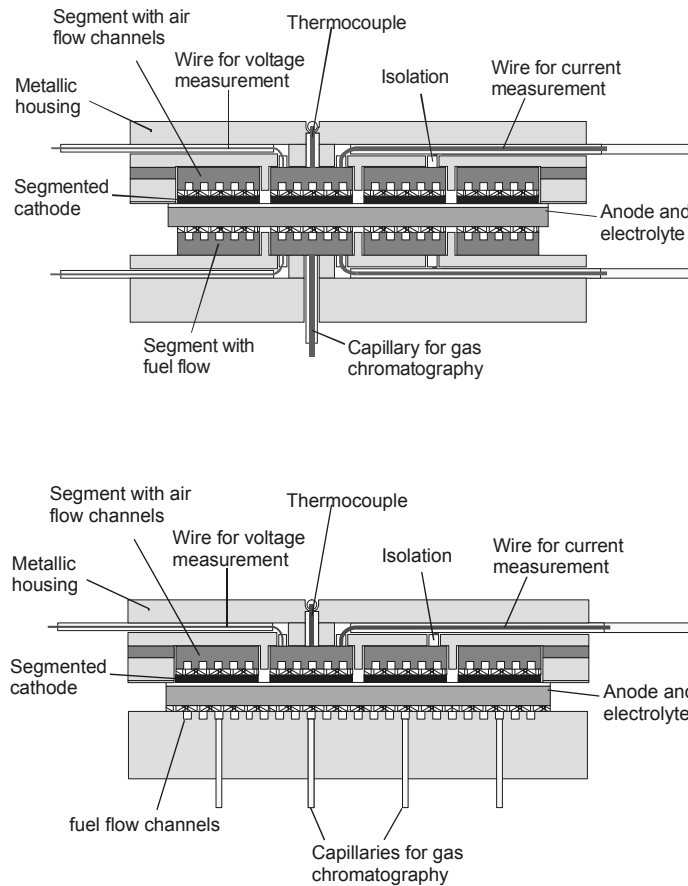


Figure 3-2: Setup of measurement systems for the characterisation of planar segmented SOFCs with cathode segmentation for anode-supported cells.

At each segment voltage and current can be measured by a four-point measurement. In order to determine the temperature at each segment, thermocouples are introduced in the metallic segments at the cathode. 16 Capillary tubes that correspond to the cathodic segments are integrated at the anode side to take samples of the anode gas that can be analysed by gas chromatography.

While the gas channels for the square cell have a square cross-section of 2 mm x 2 mm the cassette design setup has a cross section as shown in Figure 3-3, which is modelled after the flow field in the cassette design for stacks.

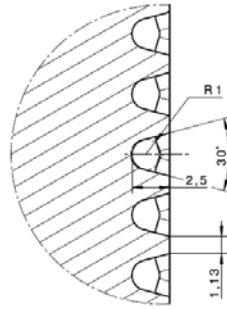


Figure 3-3: Cross section of the gas channels in the cassette design

The whole setup can be lifted into a furnace; the temperature is controlled by a Eurotherm temperature controller.

3.1 Sealing

A scheme of the sealing concept can be seen in the upper part of Figure 3-4. The sealing between the anode gas chamber and the exterior was realised by a nickel coated sealing ring (Wills Rings, Trelleborg) on which a sealing frame was put. By varying the thickness of that sealing frame the setup can be adapted to different cell thicknesses. The air passes from below through holes in the sealing frame into the cathode frame, which realises the distribution of the air into the gas channels of the flow field. Between the sealing frame and the cathode frame a layer of glass solder seals between the cathode gas chamber and the exterior. The glass solder also separates the anode gas chamber from the cathode gas chamber around the cell. The setup offers the possibility to apply weight separately on the sealing and the cell since the cathode frame and the mounting plate of the cathode measuring head are not rigidly connected.

For high air flows of 10 l/min as used in chapter 5, 6 and 7 this first setup worked fine. For lower air flows of 3 l/min as used in chapter 8 it was found that the cell setup was not sufficiently air tight. Therefore the sealing concept was changed to the one shown in the lower part of Figure 3-4. The sealing ring was replaced by a fleece (Altra paper KP1600, Rath GmbH) which densifies under pressure and high temperatures. Between the mounting plate of the cathode measuring head and the cathode frame the gap was filled with glass solder and an additional frame. Between the segments and the mounting plate glass solder was used.

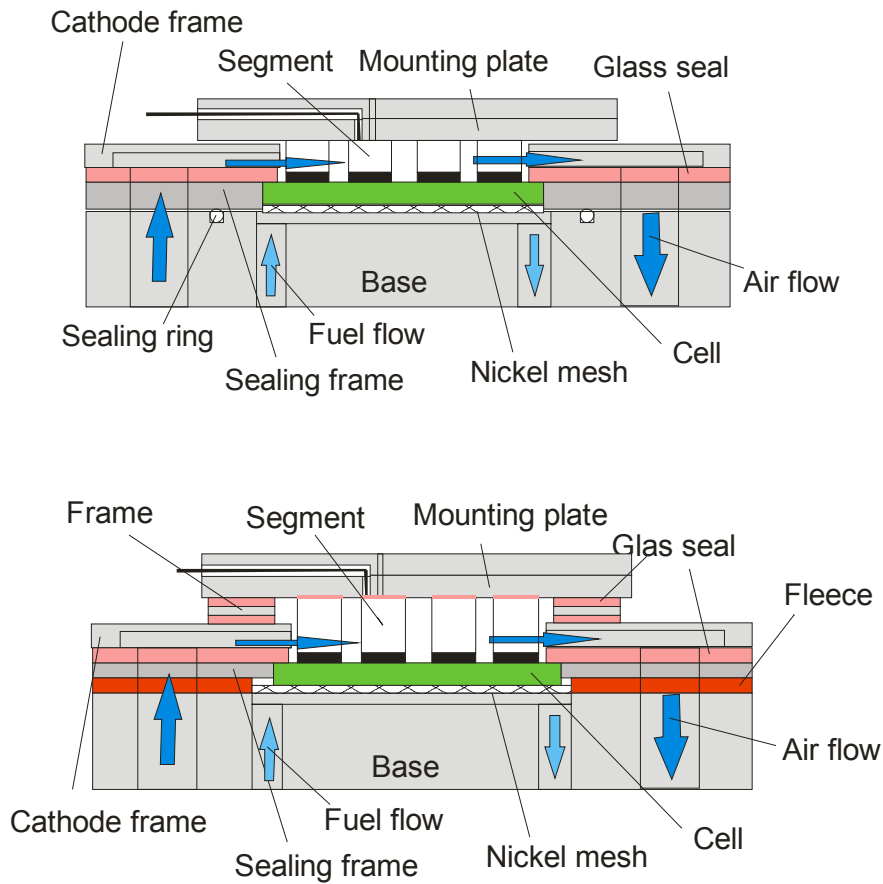


Figure 3-4: Sealing concepts

3.2 Cells

Two types of anode-supported cells were used for this thesis. The anode-supported cells used for the calibration and validation of the model in chapter 5 to 7 contained a 540 μm thick NiO/YSZ anode with a thin anode functional layer, a 7 μm thick 8YSZ electrolyte, a 7 μm thick YDC interlayer and a 30 μm thick LSCF cathode. For the contact of the electrodes nickel meshes were used on the anode and Pt meshes as well as a LSCF contact paste on the cathode. These cells will be referred to as type A.

The results shown in chapter 8 were obtained with anode-supported cells consisting of a 290 μm thick NiO/YSZ anode with an anode functional layer of about 10 μm . The 8YSZ electrolyte has a thickness of 10 μm and the cathode has a 10 μm LSM dense functional layer and 40 μm of a less dense cathode material. For the contact of the electrodes nickel meshes were used on the anode and Pt meshes as well as a LSM contact paste on the cathode. These cells will be referred to as type B.

3.3 Gas controlling system

The cell is supplied with fuel and oxidant gases by various mass flow controllers (Tylan 280). At the anode H_2 , N_2 , CO , CO_2 , CH_4 is available. At the cathode side flow controllers for air, N_2 and O_2 are installed. It is possible to change the air flow direction through the cell during operation with the help of quick-connects. To be able to add steam to the fuel gases liquid water is injected in the fuel supply tubes and these tubes are heated to vaporise the water. The heating of the tubes must be adapted to the flow of gas as well as to the amount of water to achieve a stable humidification of the fuel gas. If the temperature is too low liquid water remains in the tubes and the water content of the gas is lower than wanted. If on the other hand the temperature is too high irregularities in pressure may occur and the steam content varies which results in a varying voltage of the cell. The water is measured out by a peristaltic pump that can supply amounts of water between 0.0037 ml/min and 49 ml/min, depending on the kind of tube that is used, without pulsation. The pump is calibrated regularly, and since the age of the tubes has an influence on the amount of water transported through them it is checked every few days and before taking i-V curves. This is done by weighting the water transported by the pump during a set time.

3.4 Data logging

The data logging system was developed by Patrick Metzger and is described in detail in [30]. The local voltage, current, power and temperature is logged by two Agilent multimeter 34970A. It is possible to switch between the measurements of current-voltage curves when the segments are connected to a common current collector, OCV measurements where the segments have no connection with each other and to connect the cell to an impedance analyser. This setup is shown schematically in Figure 3-5. An Agilent VEE 6.1 program controls those switches and also visualises the local voltage, current, power and temperature. The operation parameters of a measurement are recorded in an MS Access database.

3.5 Electronic load and average voltage

An electronic load (EL1000 by Zentro Elektrik) and a constanter (XKW 8-125 by Xantrex) are used to take current-voltage characteristics. For its control an average synthetic voltage is generated from the 16 single voltages of the segments. The current of the 16 segments is measured through measuring resistors and collected at a current collector shown schematically in Figure 3-5 which is in turn connected to the electronic load.

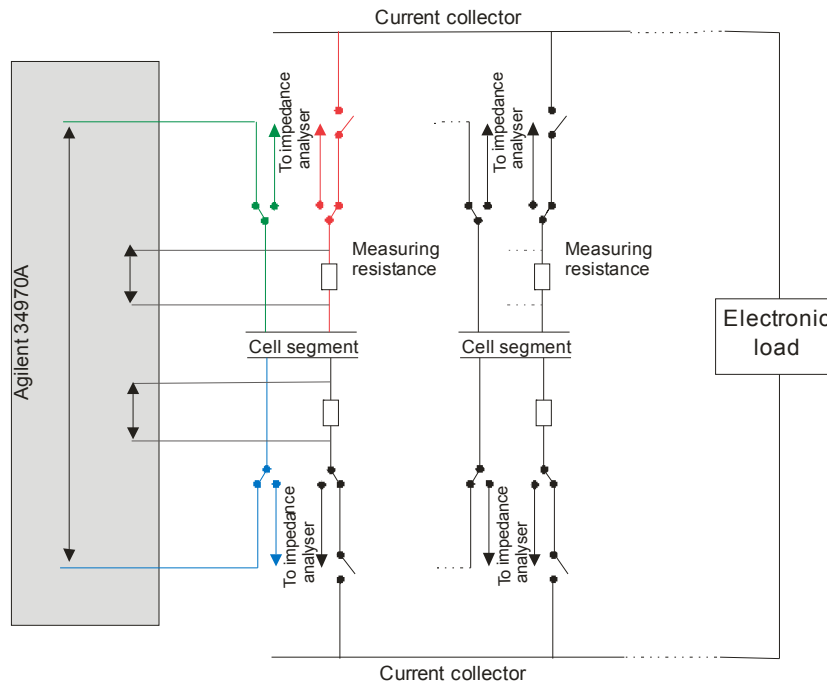


Figure 3-5: Scheme of the measuring periphery

3.6 Impedance analyser

The entire cell or single segments can be connected to an impedance analyser by the switches shown in Figure 3-5. Impedance spectra of the whole cell can be taken or the single segments can be measured consecutively. An impedance analyser Im6 by Zahner is used. Impedance spectra can be taken at OCV and under polarisation. The Im6 can apply currents up to 3 A; for higher currents an additional power potentiostat (PP 240) is used which allows for measurements up to 40 A.

3.6.1 Impedance spectroscopy

In addition to the i-V curves described in chapter 2.4 impedance spectroscopy is often used for the characterisation of fuel cells. Impedance spectroscopy is a non-destructive method that is often used for in-situ analysis of fuel cells. It is used for the evaluation of performance and degradation mechanisms. It allows for a better understanding of the electrochemical reaction kinetics as well as for the determination of mass transport limitations and diffusion processes in the cell. Unlike current-voltage curves it permits to assign losses to the different cell components [30-32].

Impedance is the complex alternating current resistance of a system and as such the ratio of complex alternating voltage $\hat{u}(t) = U_0 \exp(i(2\pi ft + \varphi))$ and complex alternating current $\hat{i}(t) = I_0 \exp(i(2\pi ft + \varphi))$ as in equation (3-1). This resistance is frequency-dependent. If an alternating

voltage is applied to a linear system it results in an alternating current response with the same frequency [32-34]. A fuel cell is a non-linear system because of the coupling of various processes. Nevertheless, if the amplitude of the excitation is small ($\Delta U < RT/F$), the answer of the system will by approximation be linear [32, 35].

$$Z = \frac{\hat{u}(t)}{\hat{i}(t)} = \frac{U_0}{I_0} \cdot \exp[i(2\pi ft + \varphi) - i(2\pi ft + \phi)] = |Z|(\cos(\varphi - \phi) + i \cdot \sin(\varphi - \phi)) = Z' + i \cdot Z'' \quad (3-1)$$

Z' real part of the impedance [Ω]
 Z'' imaginary part of the impedance [Ω]

Phase shift and amplitude of the response depend on the characteristics of the investigated system. A capacitance results in the current preceding the voltage by $\pi/2$, for an inductivity voltage precedes current by $\pi/2$. An ohmic resistance leads to current and voltage in phase [33]. In a complex system like a fuel cell the different effects superimpose. If the answer for the different components are dependent on the frequency different effects can be separated by measuring over a large range of frequencies.

Impedance spectra are usually plotted in either Nyquist or Bode plots. The Bode plot shows the impedance Z logarithmically and the phase φ over the logarithmic frequency. The Nyquist plot shows the imaginary part of the impedance over the real part. In this kind of diagram the frequency is not directly visible. Figure 3-6 a shows the Bode plot of one fuel cell electrode including electrolyte resistance, charge transfer and double layer capacity. Figure 3-6 b shows its Nyquist plot.

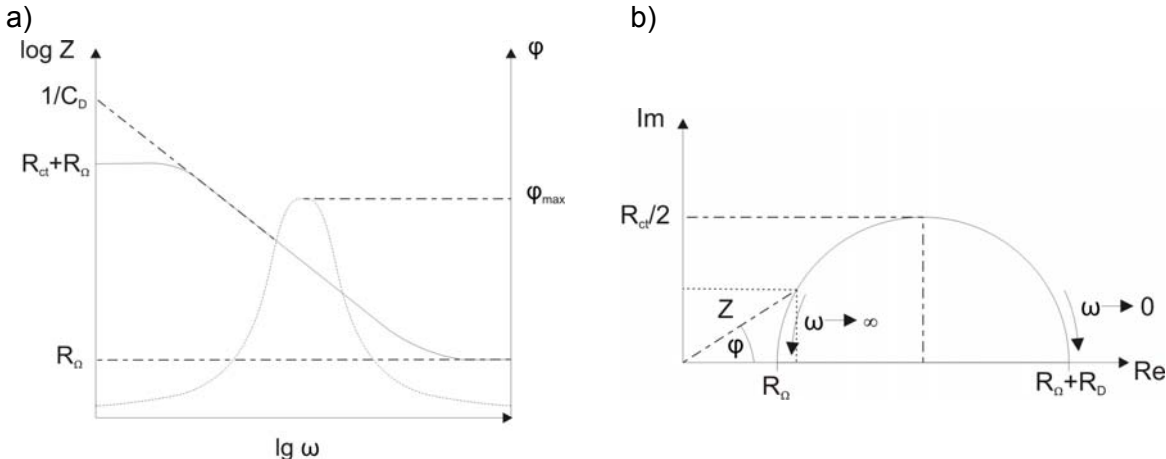


Figure 3-6: Schematic Bode plot (a) and Nyquist plot (b) of a fuel cell electrode including charge transfer and electrolyte resistance

At high frequencies the impedance corresponds to the ohmic resistance R_{Ω} of the cell, which is the electrolyte resistance as well as the contact resistances of the electrodes. In the Bode plot it is the value of Z for high frequencies. In the Nyquist plot it is the intersection of the semicircle and the real part axis of the diagram. In the Bode plot the sum of electrolyte resistance and charge transfer resistance R_{ct} can be seen for $\omega=0$. In the Nyquist plot the charge transfer resistance corresponds to the diameter of the semicircle.

In a real fuel cell with two porous electrodes several semicircles that correspond to different processes overlap. The oxidation of H_2 at the anode is a faster process than the reduction of oxygen at the cathode, which is why it can be seen at higher frequencies. The slowest process is the diffusion which can be seen at low frequencies.

3.6.1.1 Equivalent circuit model

An analysis of the frequency-dependent impedance spectra is often done with the help of an equivalent electric circuit model. It consists of a serial and parallel connection of electric elements. A simple equivalent circuit is shown in Figure 3-7.

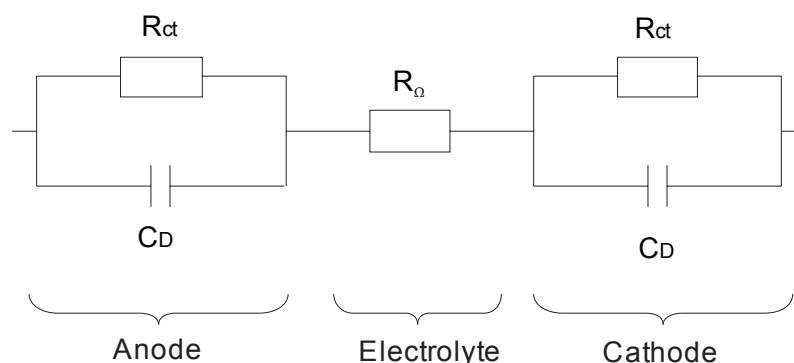


Figure 3-7: Equivalent circuit model of a fuel cell

The electrolyte and other ohmic resistances e.g. contact resistance and wire resistance are represented by the resistance R_{Ω} , while the electrodes are each represented as a parallel connection of the double layer capacitance C_D and the charge transfer resistance R_{ct} at the electrode. One $R_{ct}C_D$ component corresponds to one semicircle in the Nyquist plot. The values of the single components are then fitted to show the same behaviour as the impedance measurement.

In real impedance spectra the semicircles in the Nyquist plot are often more shallow arches than shown in Figure 3-6. To model this behaviour a constant phase element which

resembles a circle with the centre below the real-part-axis may be used instead of a capacitor. There are also a number of other elements or combinations of elements which can be used to model for instance porous electrodes or diffusion.

3.6.1.2 Reference electrodes

For a completely reliable separation of the effects of the anodic and cathodic contributions additional information may be obtained by using a reference electrode. With solid and very thin electrolytes as are used in SOFC this is difficult to accomplish.

Since the reference electrode cannot be placed into the middle of the electrolyte because of its thinness reference electrodes for SOFC usually consisted of an additional electrode on the surface as shown in Figure 3-8. Also shown in Figure 3-8 are planes of constant potential within the electrolyte which bend towards the electrolyte surface at the edge of the electrode.

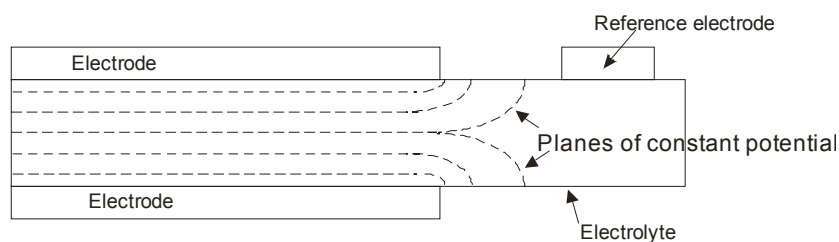


Figure 3-8: Schematic setup with reference electrode and planes of constant potential within the electrolyte

At the edge of the normal electrode the potential changes corresponding to the planes of constant potential within the electrode. The non-active part of the electrolyte with a constant potential corresponding to the potential in the middle of the electrolyte in Figure 3-8 is located about three times the electrolyte thickness away from the edge of the electrode [36] which is where a reference electrode should be placed.

The position of the reference electrode as well as its geometry has a great influence on the results of the measurements [37]. Misalignment of the active electrodes in the order of the thickness of the electrolyte leads to errors up to 100%. Even for ideally positioned electrodes that are not identical artefacts and distortion of the arches in the Nyquist diagram occur. Differences of resistance between the active electrodes also lead to errors [38]. Because of this immense need for accuracy and the large errors reference electrodes in thin SOFC are little reliable and are not used in the experiments done for this thesis.

3.7 Gas chromatograph

Gas samples can be taken at the anode at 16 locations corresponding to the cathodic segments and consequently analysed in a gas chromatograph (CP 4900 by Varian Inc). Before the gas enters the chromatograph the water contained in the sample is removed by a steam trap and a filter (Genie). Only one sample can be analysed at a time which is why measurements at the segments are done successively. Before each measurement gas is taken from the segment for 50 s to rinse the tubes. This gas bypasses the gas chromatograph. Inside the gas chromatograph two columns are used to separate N₂, H₂, O₂, CO, CO₂ and CH₄. Argon is used as carrier gas.

3.8 Reproducibility of setup

To test the reproducibility of the whole setup three different cells were tested with the measuring conditions from Table 8-1 on page 93 and the results at 800°C were compared. An uneven distribution of OCV is an indication for leaks at the cell or sealing. With the new sealing concept described in chapter 3.1 a variation in OCV from segment to segment of below 2% or 17 mV was achieved. To assess the comparability under load the voltage at 400 mA/cm² of the different cells was compared for the highest flow rate. If segments that performed visibly worse than others are disregarded, the values varied for about 10 % which is considered the accuracy of the measurements.

3.9 Comparison to non-segmented cell

In a non-segmented fuel cell lateral currents within the electrodes are expected to lead to a homogenisation of voltage. The effects will therefore be not as pronounced in a non-segmented cell as in the segmented setup. In the segmented setup compensating currents between the segments have to pass through the external wires, measuring resistance and external current collector. Figure 3-9 shows this difference schematically. The red arrows indicate the path compensating currents have to take in the segmented setup while the arrow in blue shows the path in a non-segmented cathode which is indicated by the shaded area.

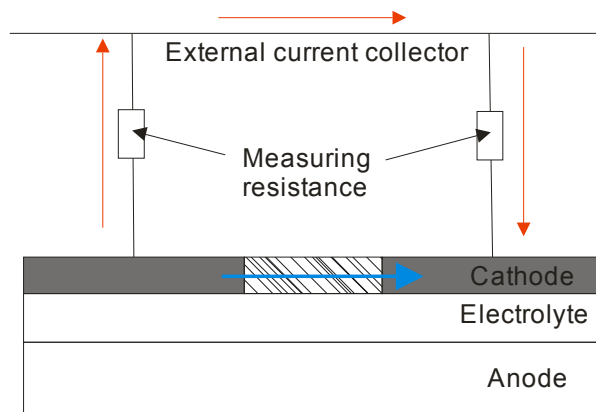


Figure 3-9: Current paths of compensating currents in a segmented cell (red) and a non-segmented cell (blue)

The conductivity σ of LSM is given in literature to be between 130 S/cm [39] and 224 S/cm [10]. LSM-YSZ composites show a lower conductivity of about 10 S/cm [40] or even lower [41]. If the resistance compensating currents meet in a non-segmented setup from one segment in the setup to the other is supposed to be determined by the distance between the middles of two adjoining segments (1.65 cm) and the thickness of the cathode and if conductivity is assumed to be 200 S/cm the resistance between two segments would be 0.611 Ω according to equation (3-2).

$$R = \frac{l}{\sigma \cdot A} \quad (3-2)$$

Part of the external circuit is at high temperature and part at room temperature. If the resistance in the hot area is calculated from the material data the resistance for 2 x 15 cm of platinum wire and 2 x 40 cm of microfer wire at 800°C is 0.475 Ω between two segments. The wiring outside the furnace was measured to have a resistance of 0.1 Ω and includes the measuring resistances of 10 m Ω . This gives a total resistance between two segments of 0.575 Ω .

The resistance of the wires leading from the cell to the external current collector was estimated for the model from chapter 4 to be 1.4 Ωcm^2 relating to one segment of the square setup. This results in a resistance of 0.37 Ω from segment to segment.

The values for the resistance within the electrode and in the external circuit are of the same order. It may be assumed that in a non-segmented setup the homogenisation of the voltage is not exclusively achieved by the lateral conductivity of the electrodes but rather because of

the high conductivity within the bipolar plate resulting in a more homogeneous distribution of voltage. The effect of segmentation will be treated further in chapter 5.6.4.

4 Simulations

For the simulations the detailed electrochemical model for fuel cells which was developed by Bessler et al. [42] was used. The model is implemented in an in-house numerical simulation software. The extension and adaptation of the model to the segmented setup was done by S. Gewies [43] and is summarized here. The model is a multiscale model since it takes into account the nanoscopic surface transport at the triple phase boundary, on a microscopic level the mass and charge transport in the porous electrodes and on a macroscopic level the transport in the gas channels.

4.1 Gas transport

The model is a detailed 1D + 1D elementary kinetic electrochemical model in which one channel of the experimental setup is represented.

The transport in the gas channels in the x dimension as shown in Figure 4-1 is described using the Navier-Stokes equations of conservation of mass, energy and momentum. Plug flow is assumed, that is an even distribution of velocity over the cross section and an equal residence time of all fluid elements [44]. Gradients in y or z directions are neglected.

The mass transport of gas phase species within the porous electrode is diffusive and mainly in y-direction. It is described by a combination of Stefan-Maxwell and Knudsen diffusion and Darcy flow. Porosity and tortuosity, which lengthens the ways within the porous media, are considered. Fick's law describes the diffusion of one species within another. The flow is proportional to the concentration gradient. Knudsen diffusion takes an additional diffusion limitation into account due to small pore sizes. If the pore size is equal or smaller than the mean free path of the gas particles an interaction of pore wall and the gas occurs. The Knudsen diffusion coefficient depends for each species on its molar mass and the cross section of the pores. Darcy's law describes the flow of a fluid through a porous media due to pressure difference. It takes into account the permeability of the porous media and the viscosity of the fluid.

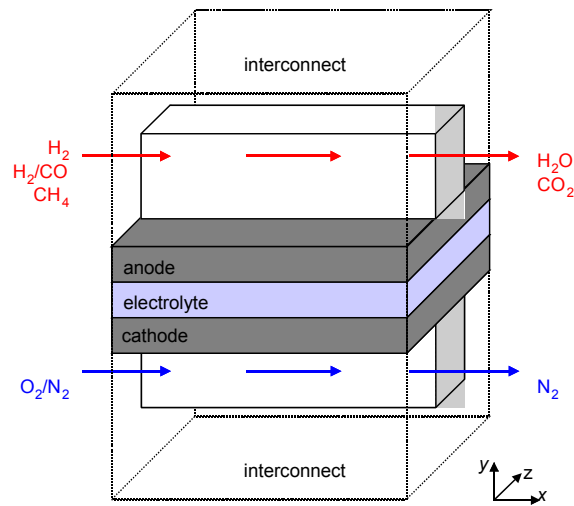


Figure 4-1: Model of SOFC. Two-dimensional representation of a single gas channel including MEA and interconnect [42]

The transport in the gas channel and in the porous electrode is coupled at the interface by the sum of all flow rates across it and pressure being the same for channel and electrode at the interface [43]. Since the electrolyte is considered to be gas tight all flow rates across it are 0 in the model. The charge transport through the electrolyte and in the YSZ part of the electrodes is described two-dimensionally by Ohm's law [45].

4.2 Electrochemistry

Anode electrochemistry is described using previously validated elementary kinetics for surface reactions on Ni and YSZ, and for charge transfer [46]. Hydrogen spillover is seen as the rate determining step. The reactants (e.g. H_2 at the anode) are adsorbed at the catalytic surface and split into ions (e.g. H^+) as presented in Figure 4-2. The charge transfer reaction takes place at the triple phase boundary between gas, electrode and electrolyte where the adsorbed H^+ ions cross from electrode to electrolyte and combine with the O^{2-} ions out of the electrolyte to form H_2O which then desorbs from the surface. The reactions on the nickel and YSZ surfaces as well as the charge transfer reaction are given in Table 4-1.

The difference of potential $\Delta\Phi$ as given in equation (4-1) between electrode and electrolyte outside the space charge layer leads to the charge transfer.

$$\Delta\Phi = \Phi_{\text{electrode}} - \Phi_{\text{electrolyte}} \quad (4-1)$$

The cell voltage and current-voltage relationships of the entire cell can be obtained by equation (4-2).

$$E(i) = \Delta\Phi_{\text{cathode}}(i) - \Delta\Phi_{\text{anode}}(i) - iR_{\text{electrolyte}} \quad (4-2)$$

The rates of the forward and backward charge transfer reaction $k_{f,ct}$ and $k_{r,ct}$ are given by equations (4-3) and (4-4). They depend on the potential difference $\Delta\Phi$ from equation (4-1), where $k_{f,ct}^0$ and $k_{r,ct}^0$ are factors, E^{act} the activation energies for forward or backward reactions and α the symmetry factor. The units of the preexponential factors depend on how many species take part in the reaction and whether these are surface adsorbed, gas phase species or from the bulk material.

$$k_{f,ct} = k_{f,ct}^0 \exp\left(-\frac{E_{f,ct}^{\text{act}}}{RT}\right) \exp\left(-\left(1-\alpha\right)\frac{zF}{RT}\Delta\Phi\right) \quad (4-3)$$

$$k_{r,ct} = k_{r,ct}^0 \exp\left(-\frac{E_{r,ct}^{\text{act}}}{RT}\right) \exp\left(\alpha\frac{zF}{RT}\Delta\Phi\right) \quad (4-4)$$

The rate constants of the surface reactions $k_{f,m}$ and $k_{r,m}$ that determine the production rates of species on the surface are given by the Arrhenius equations (4-5) and (4-6). The index m stands for the different reactions. Production rates depend on the rate constant and on the surface coverage or concentration of the species.

$$k_{f,m} = k_{f,m}^0 \exp\left(-\frac{E_{f,m}^{\text{act}}}{RT}\right) \quad (4-5)$$

$$k_{r,m} = k_{r,m}^0 \exp\left(-\frac{E_{r,m}^{\text{act}}}{RT}\right) \quad (4-6)$$

The elementary kinetic approach allows for a physical description of current-voltage relationships without using the Nernst equation which is only valid at OCV and without having to resort to semi-empirical calculation of overvoltages [42]. In the model the elementary kinetic mechanism is used for the forward reaction. The kinetic parameters for the backward reaction are determined by thermodynamic consistency as given in equations (4-7) and (4-8).

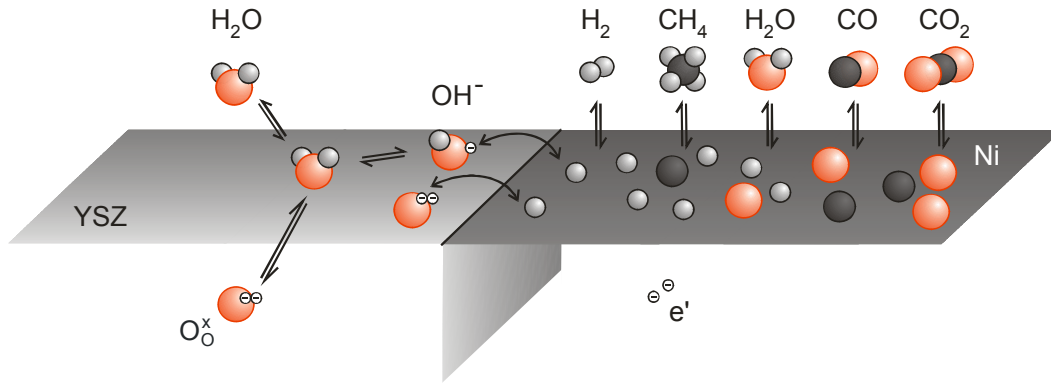


Figure 4-2: Surface electrochemistry at the anode triple-phase boundary [47].

Anode Reaction	Preexponential factor k_f^0	Activation energy $E_{f,m}^{act}$	
<i>Charge transfer reaction (Fit):</i>			
$H_{Ni} + OH^-_{YSZ} \rightleftharpoons \square_{Ni} + H_2O_{YSZ} + e^-_{Ni}$	$1.63 \cdot 10^5 \text{ mol}/(\text{m s})^a$	235 kJ/mol^b	
<i>YSZ surface reactions:</i>			
$H_2O + \square_{YSZ} \rightleftharpoons H_2O_{YSZ}$	$6.6 \cdot 10^{11} \text{ cm}^3/(\text{mol s})$	0	
$H_2O_{YSZ} + O^{2-}_{YSZ} \rightleftharpoons 2 OH^-_{YSZ}$	$1.6 \cdot 10^{22} \text{ cm}^2/(\text{mol s})$	9.6 kJ/mol	
$O^x_{O_{YSZ}} + \square_{YSZ} \rightleftharpoons V_{O_{YSZ}}^{\bullet\bullet} + O^{2-}_{YSZ}$	$1.6 \cdot 10^{22} \text{ m/s}$	91 kJ/mol	
<i>Nickel surface reactions:</i>			
$H_2 + 2 \square_{Ni} \rightleftharpoons 2 H_{Ni}$	$9.8 \cdot 10^{17} \text{ cm}^5/(\text{mol s})$	0	
$H_2O + \square_{Ni} \rightleftharpoons H_2O_{Ni}$	$1.4 \cdot 10^{10} \text{ cm}^3/(\text{mol s})$	0	
$H_{Ni} + O_{Ni} \rightleftharpoons OH_{Ni} + \square_{Ni}$	$5.0 \cdot 10^{22} \text{ cm}^2/(\text{mol s})$	98 kJ/mol	
$H_2O_{Ni} + O_{Ni} \rightleftharpoons 2 OH_{Ni}$	$5.4 \cdot 10^{23} \text{ cm}^2/(\text{mol s})$	209 kJ/mol	
$H_{Ni} + OH_{Ni} \rightleftharpoons H_2O_{Ni} + \square_{Ni}$	$3.0 \cdot 10^{20} \text{ cm}^2/(\text{mol s})$	43 kJ/mol	
Cathode reaction	Exchange current density	Activation energy	Exponent a for p_{O_2}
$1/2 O_2 + V_{O_{YSZ}}^{\bullet\bullet} + 2 e^- \rightleftharpoons O^x_{O_{YSZ}}$	$4.4 \cdot 10^{10} \text{ A/m}^2^a$	125 kJ/mol^c	0.47^a

^a Fitted to the present experiments.

^b Fitted to experiments with symmetrical SOFC cermet anodes[46].

^c Activation energy from dense thin film electrodes [48].

Table 4-1: Elementary kinetic reaction mechanisms for the anode and global kinetic reaction for the cathode. A single hydrogen spillover between Ni and YSZ surfaces is assumed as active charge-transfer reaction with a symmetry factor $\alpha = 0.5$. Surface site densities of Ni and YSZ are $6.1 \cdot 10^{-9}$ and $1.3 \cdot 10^{-9} \text{ mol/cm}^2$ respectively [42, 45].

$$E_{f,m}^{\text{act}} - E_{r,m}^{\text{act}} = \Delta H_m \quad (4-7)$$

$$\frac{k_{f,m}^0}{k_{f,r}^0} = \exp\left(\frac{\Delta S}{R}\right) \quad (4-8)$$

Within the porous anode, reforming and water-gas shift reactions on the Ni surface are included as in [42]. The fuel gases adsorb at the nickel surface where they are split into ions as in Figure 4-2. The elementary-kinetic mechanism used was developed by Janardhanan and Deutschmann [49] consisting of 21 reversible reactions between 6 gas-phase and 15 surface-adsorbed species. Table 4-2 gives the kinetic reaction mechanisms on the nickel surface of the anode for fuel gases containing carbon. Gas phase species reactions are treated in analogy to surface reactions and are modelled depending on equations (4-5) and (4-6) and concentrations [42]. YSZ surface reaction and charge transfer reactions are the same as in Table 4-1.

<i>Nickel surface reactions</i>		
$\text{H}_2 + 2 \square_{\text{Ni}} \rightleftharpoons 2 \text{H}_{\text{Ni}}$	$\text{H}_{\text{Ni}} + \text{OH}_{\text{Ni}} \rightleftharpoons \text{H}_2\text{O}_{\text{Ni}} + \square_{\text{Ni}}$	$\text{CH}_3_{\text{Ni}} + \square_{\text{Ni}} \rightleftharpoons \text{CH}_2_{\text{Ni}} + \text{H}_{\text{Ni}}$
$\text{O}_2 + 2 \square_{\text{Ni}} \rightleftharpoons 2 \text{O}_{\text{Ni}}$	$2 \text{OH}_{\text{Ni}} \rightleftharpoons \text{H}_2\text{O}_{\text{Ni}} + \text{O}_{\text{Ni}}$	$\text{CH}_2_{\text{Ni}} + \square_{\text{Ni}} \rightleftharpoons \text{CH}_{\text{Ni}} + \text{H}_{\text{Ni}}$
$\text{CH}_4 + \square_{\text{Ni}} \rightleftharpoons \text{CH}_{4\text{Ni}}$	$\text{C}_{\text{Ni}} + \text{O}_{\text{Ni}} \rightleftharpoons \text{CO}_{\text{Ni}} + \square_{\text{Ni}}$	$\text{CH}_{\text{Ni}} + \square_{\text{Ni}} \rightleftharpoons \text{C}_{\text{Ni}} + \text{H}_{\text{Ni}}$
$\text{H}_2\text{O} + \square_{\text{Ni}} \rightleftharpoons \text{H}_2\text{O}_{\text{Ni}}$	$\text{CO}_{\text{Ni}} + \text{O}_{\text{Ni}} \rightleftharpoons \text{CO}_2_{\text{Ni}} + \square_{\text{Ni}}$	$\text{CH}_4_{\text{Ni}} + \text{O}_{\text{Ni}} \rightleftharpoons \text{CH}_3_{\text{Ni}} + \text{OH}_{\text{Ni}}$
$\text{CO}_2 + \square_{\text{Ni}} \rightleftharpoons \text{CO}_2_{\text{Ni}}$	$\text{HCO}_{\text{Ni}} + \square_{\text{Ni}} \rightleftharpoons \text{CO}_{\text{Ni}} + \text{H}_{\text{Ni}}$	$\text{CH}_3_{\text{Ni}} + \text{O}_{\text{Ni}} \rightleftharpoons \text{CH}_2_{\text{Ni}} + \text{OH}_{\text{Ni}}$
$\text{CO} + \square_{\text{Ni}} \rightleftharpoons \text{CO}_{\text{Ni}}$	$\text{HCO}_{\text{Ni}} + \square_{\text{Ni}} \rightleftharpoons \text{CH}_{\text{Ni}} + \text{O}_{\text{Ni}}$	$\text{CH}_2_{\text{Ni}} + \text{O}_{\text{Ni}} \rightleftharpoons \text{CH}_{\text{Ni}} + \text{OH}_{\text{Ni}}$
$\text{H}_{\text{Ni}} + \text{O}_{\text{Ni}} \rightleftharpoons \text{OH}_{\text{Ni}} + \square_{\text{Ni}}$	$\text{CH}_4_{\text{Ni}} + \square_{\text{Ni}} \rightleftharpoons \text{CH}_3_{\text{Ni}} + \text{H}_{\text{Ni}}$	$\text{CH}_{\text{Ni}} + \text{O}_{\text{Ni}} \rightleftharpoons \text{C}_{\text{Ni}} + \text{OH}_{\text{Ni}}$

Table 4-2: Elementary kinetic reaction mechanism for the anode. A single hydrogen spillover between Ni and YSZ surfaces is assumed as active charge-transfer reaction with a symmetry factor $\alpha = 0.5$. The surface site densities of Ni and YSZ are $6.1 \cdot 10^{-9}$ and $1.3 \cdot 10^{-9} \text{ mol cm}^{-2}$, respectively.

At the cathode the reaction mechanisms are less complex than at the anode. Only one reaction mechanism is taking place as shown in Table 4-1. The focus is therefore on the anode and no elementary kinetics approach but a global kinetics approach is used for cathode electrochemistry. It is described using a modified Butler-Volmer equation (4-9) as derived by Zhu et al. [50].

$$i_F = i_0 \frac{(p_{O_2}/p_{O_2}^0)^{0.25}}{1 + (p_{O_2}/p_{O_2}^0)^{0.5}} \left[\exp\left(\frac{0.5F\eta_{act}}{RT}\right) - \exp\left(-\frac{0.5F\eta_{act}}{RT}\right) \right] \quad (4-9)$$

Here the current i_F is calculated depending on the activation overvoltage η_{act} . i_0 and $p_{O_2}^0$ are the exchange current density and a nonlinear function given by Zhu et al. [50].

4.3 Segmentation

The segmentation of the experimental setup is represented by an electric circuit model including the peripheral devices of the setup which is joined to the model of the cell, gas channels and interconnectors. This external circuit model is shown schematically in Figure 4-3. The model represents the experimental setup with the possibility of measuring voltage and current at each segment as well as the global voltage and current. All segments can be connected via the switches S_i to the outer current collectors. These collectors are at a constant potential and are connected to the electronic load. The connecting wires are represented as resistors R_i in the model. Being ohmic resistors they lead to a potential drop that depends on the segment current density. The number and size of the segments can be changed. For the simulations, four segments were used at both anode and cathode which conforms to the experimental setup. The switches S_i were closed for the simulation of polarisation of the cell. The resistance of the wires was determined by fitting to the experiments.

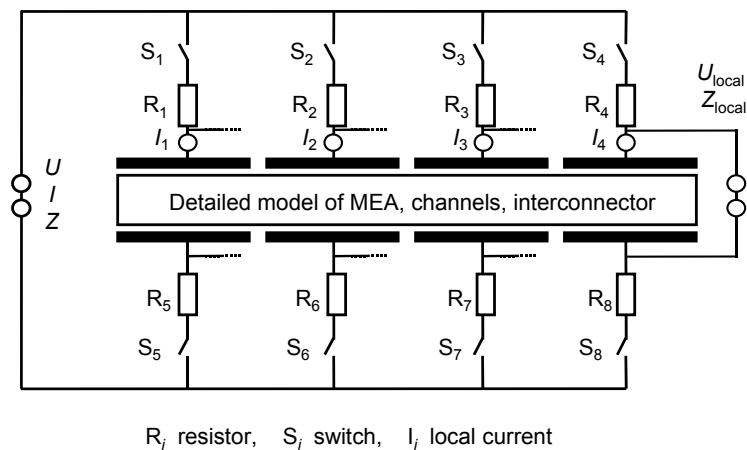


Figure 4-3: Representation of the segmented setup by an electric circuit

The simulation yields the total current I , the individual segment currents I_i , as well as local segment voltages U_{local} . The model could also be used to calculate global and local impedance Z and Z_{local} , respectively.

4.4 Model parameters

There are a number of model parameters associated with electrochemistry and transport in the membrane electrode assembly (MEA) that are specific for the investigated cells and cannot be obtained from literature. Some parameters can be reliably estimated (e.g., porosity from scanning electron micrographs (SEM)). Other parameters, however, can only be obtained by fitting to experimental data. Model parameters obtained and used in this thesis are summarised in Table 4-3. For the geometric parameters the first value given corresponds to the square cells, the second value to the cassette design.

The simulations shown in this thesis were all done assuming isothermal conditions. For the H₂ simulations in chapter 5 wall shear stress was taken into account while the Darcy flow at the anode was disabled. There is no need to include Darcy flow in this case because the number of molecules stays constant when H₂ is converted to H₂O. The simulations with CH₄ in chapter 7 do include Darcy flow but they do not include wall shear stress.

Model parameter	Value	Ref.
<i>Gas channel</i>		
Length	8.8 cm / 5.6 cm	Setup
Channel cross-sectional area	4 mm ² / 5.17 mm ²	Setup
Channel perimeter	4 mm / 3.93 mm	Setup
<i>Segmented cell</i>		
Number of segments in one channel	4	Setup
Segment area	2.2 cm x 2.2 cm / 1.4 cm x 2.7 cm	Setup
<i>Porous media</i> (mesh anode (ma), cermet anode (an), porous cathode (ca), mesh cathode (mc))		
Layer thickness: ma, an, ca, mc	450 μm, 540 μm, 55 μm, 490 μm	Setup
Porosity: ma, an, ca, mc	0.74, 0.32, 0.40 ^a , 0.82	Setup
Pore size: ma, an, ca, mc	100 μm, 0.7 μm, 0.5 μm ^a , 125 μm	Setup
Particle size: ca, mc	0.5 μm ^a , 40 μm	Setup
Tortuosity: ma, an, ca, mc	1.4 ^a , 2.9 ^b , 1.4 ^a , 1.4 ^a	
<i>Cermet anode</i>		
Active three-phase boundary length	4.5 · 10 ¹² m/m ³	Micro-structural model
Effective width electrolyte	0.43 μm	[46]
Effective width electrode	0.31 μm	
Structural factor electrolyte conductivity	0.30	
<i>Electrolyte</i>		
Effective thickness	10 μm	Setup
Conductivity bulk 8YSZ: preexponential factor,	5.15 · 10 ⁷ SK/m,	
activation energy	84 kJ/mol	[46]
<i>Additional resistances</i>		
Resistance of wires	1.4 Ωcm ^{2b}	Exp.
<i>Conditions</i>		
Temperature	700 - 800 °C	Exp.
Pressure	1013 hPa	Exp.

^a Estimated.

^b Fitted to the present experiments.

Table 4-3: Model parameters used for calculations.

5 H₂ measurements for the calibration of model parameters

Several model parameters associated with electrochemistry and transport in the MEA are specific for the investigated cells and cannot be obtained from literature or data sheets. Some of the parameters can be estimated like the porosity which was obtained from scanning electron micrographs. Other parameters can only be obtained by fitting to experimental data. Therefore the model was validated under suitable operating conditions with H₂, N₂, CO and CO₂ at the anode and oxygen and nitrogen at the cathode. Measurements of polarisation curves were done to adapt the model to the cells used in the experiments.

Four parameters that influence the chemical processes at the cell were fitted. The geometric parameters that were to be fitted were the tortuosities of the anode and the cathode. The porosity and particle size of the anode and cathode were obtained from scanning electron micrographs. The other two fitting parameters are the preexponential factor of the production rate on the surface $k_{f,m}$ at the anode and the exchange current density i_0 of the global kinetic charge-transfer reaction at the cathode [43]. The other kinetic parameters were used from previous cermet anode studies without modification [46].

5.1 Measuring conditions

For the calibration measurements polarisation curves were taken. The operating conditions chosen to calibrate the model are summarised in Table 5-1. The composition of the anode gas (H₂, H₂O and N₂), the composition of the cathode gas (air, O₂) as well as the temperature was varied. All variations were done with low fuel utilisation (<15%), and high flow rates of 380 to 760 ml/s and 280 to 1200 ml/s to avoid any spatial gradients along the channel. To ensure the comparability of the results operation condition no.1 was repeated regularly.

From number 2 to 5 the water content was varied between 3% and 60% to determine the kinetics of the H₂ oxidation. The dilution of the fuel gas with nitrogen was varied in numbers 4, 6 and 7 to fit the tortuosity of the anode. In 1, 4, 8 and 9 the composition of the cathode gas was varied for fitting the tortuosity of the cathode. The measurement conditions no. 1 and 10-15 are temperature variations at 700 °C, 750 °C, 800 °C and 850° for obtaining the temperature dependence.

No.	Temperature [°C]	Anode			Cathode	
		% H ₂	% H ₂ O	% N ₂	% O ₂	% N ₂
1	800	50	50	0	21	79
2	800	97	3	0	100	0
3	800	90	10	0	100	0
4	800	50	50	0	100	0
5	800	40	60	0	100	0
6	800	25	25	50	100	0
7	800	5	5	90	100	0
8	800	50	50	0	50	50
9	800	50	50	0	5	95
10	850	50	50	0	100	0
11	850	50	50	0	21	79
12	750	50	50	0	100	0
13	750	50	50	0	21	79
14	700	50	50	0	100	0
15	700	50	50	0	21	79

Table 5-1: Model calibration conditions for H₂.

5.2 Calibration measurements

For the calibration measurements square anode-supported type A cells with a segmented cathode were used and operated in counter flow. The numbers of the segments and the direction of the gas flow are shown in Figure 5-1. If not stated otherwise segments 9 to 12 which are marked by the red square were used for the presentation of the data obtained and for the fitting of the model parameters.

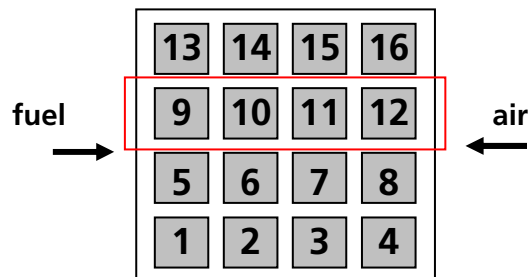


Figure 5-1: Scheme of the segmented cell with segment numbers and directions of gas flow.

5.2.1 Variation of water content

The first variation was the water content to determine the kinetics of the H_2 oxidation. Figure 5-2 shows the integral polarisation curves at different water contents in the fuel gas. The cell was fuelled with hydrogen and the water content was varied between 3% and 60%. The cathode was supplied with pure oxygen (conditions 2-5).

As expected the open circuit voltage (OCV) is lower for higher water content. It can also be seen that the higher the water content the less pronounced is the exponential behaviour at low current densities. At high water content the voltage of the cell was less stable. This is assumed to be due to an unstable vaporisation of the water.

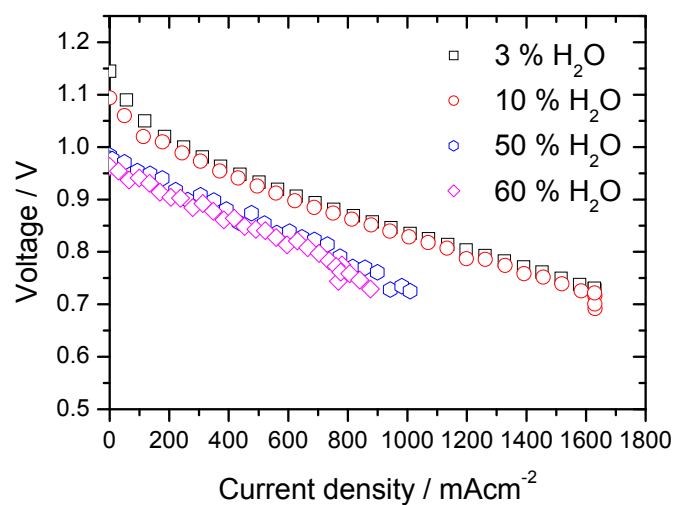


Figure 5-2: Integral polarisation curves with 3, 10, 50 and 60% of steam. Counter flow operation; anode: 5.5 l/min H_2 ; cathode: 10 l/min air; $T = 800\text{ }^\circ\text{C}$.

Figure 5-3 shows the local voltage over the local current density of segments 9 to 12 that is one row of segments from the fuel entrance to the exit for water contents of 3% and 60%. Here the local voltage is plotted versus the local current density polarisation curves. Since the fuel utilisation is low the curves of the different segments do not vary much even at high current densities. This shows that the different segments yield comparable results when operated under the same conditions and is therefore an important test of the reliability of the testing equipment.

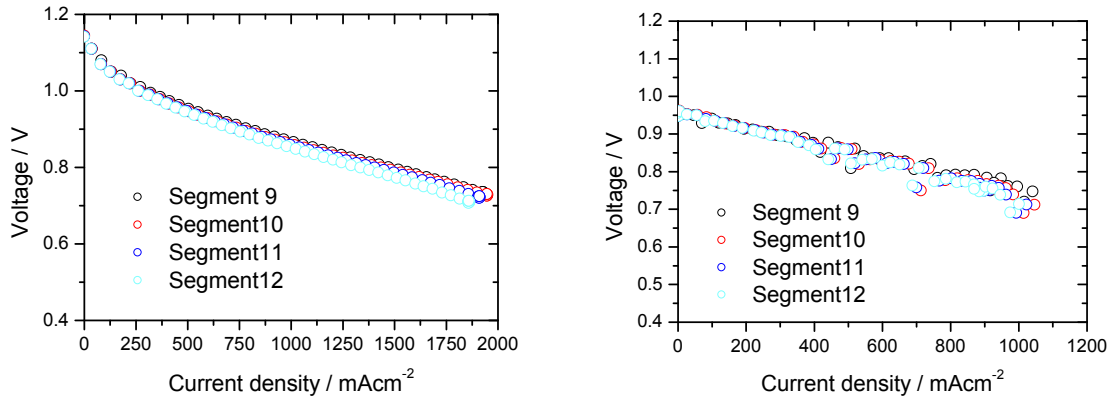


Figure 5-3: Local polarisation curves with 3% H₂O (left) and 60% H₂O (right). Counter flow operation; anode: 5.5 l/min H₂; cathode: 10 l/min air; T = 800 °C.

5.2.2 Dilution with nitrogen

The dilution of the fuel gas with nitrogen was varied in conditions 4, 6 and 7. The corresponding polarisation curves are shown in Figure 5-4. In the case of condition 6 and 7 (50% N₂ and 90% N₂, respectively) the flow rate of hydrogen was significantly lower than in the other conditions due to limitations of the nitrogen mass flow controller (2.33 l/min H₂ for condition 6 and 0.3 l/min H₂ for condition 7). This is why a diffusion limit can be seen for these curves in Figure 5-4 that did not appear for the other conditions where the flow rate of hydrogen was significantly higher.

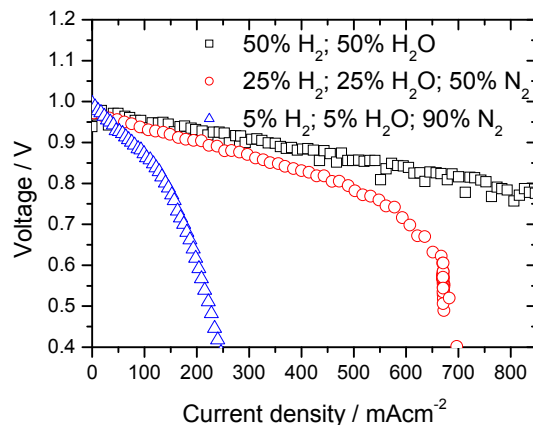


Figure 5-4: Variation of anode gas dilution with 50% H₂ and 50% H₂O. Counter flow operation; cathode: 10 l/min O₂; T = 800 °C.

The lower flow rate of hydrogen also leads to a different behaviour of the local polarisation curves which can be seen in Figure 5-5. Here the local voltage is plotted versus the local

current density polarisation curves. The curves fan out at elevated current densities. The further the segment is away from the fuel entrance the lower is the current density at which the voltage drops strongly and a diffusion limit is visible. This effect will be looked at in chapter 5.5.

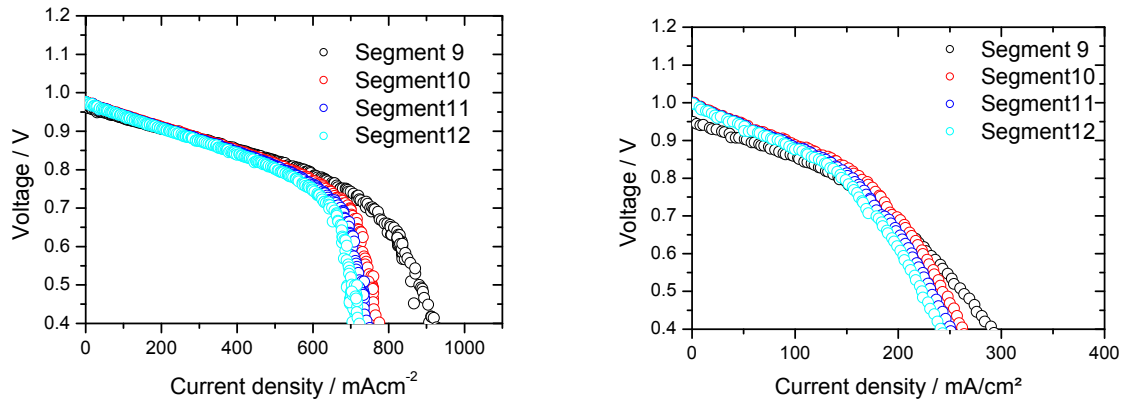


Figure 5-5: Local i-V curves of the variations of anode gas dilution with 25% H₂, 25% H₂O and 50% N₂ (left) and 5% H₂, 5% H₂O and 90% N₂ (right). Counter flow operation; cathode: 10 l/min O₂; T = 800 °C.

5.2.3 Variation of cathode gas

Another variation was the composition of the cathode gas. The variations ranged from pure oxygen over air and 50 % nitrogen with 50 % oxygen to 90% nitrogen with 10% oxygen. At the anode the cell was fuelled with 50% H₂ and 50% H₂O. The integral i-V curves can be seen in Figure 5-6. As expected the voltage of the cell is lower the lower the oxygen content on the cathode is. Since the fuel utilisation was low the local polarisation curves do not offer additional information and are therefore omitted.

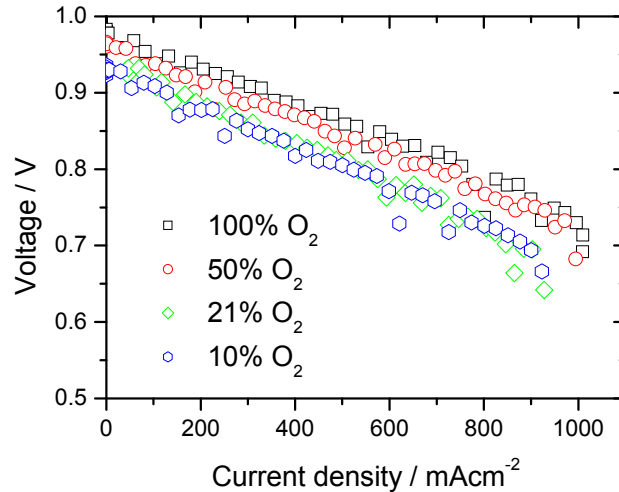


Figure 5-6: Integral polarisation curves for different compositions of the cathode gas. Counter flow operation; anode: 5.5 l/min H₂, 50 % H₂O; T = 800 °C.

5.3 Temperature variations

Finally temperature variations were done. The temperature was varied between 700°C and 850°C. Figure 5-7 shows the integral i-V curves of the temperature variations. As expected the OCV decreases with rising temperature (Nernst) and the lower the temperature the stronger the slope of the i-V curves because the conductivity of the electrolyte decreases with falling temperatures. The flow rates were high to avoid local gradients therefore the local behaviour does not show local effects and is not shown here. The cell was operated with H₂ and 50% H₂O at the anode and air on the cathode side.

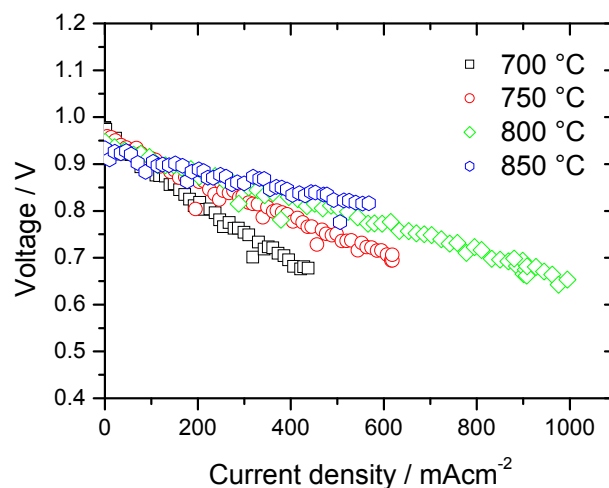


Figure 5-7: Temperature variations. Counter flow operation; anode: 5.5 l/min H₂, 50 % H₂O; cathode: 10 l/min air.

5.4 Correlation with model

For the fitting of the four free model parameters mentioned at the beginning of chapter 5 (tortuosities of electrodes, $k_{f,m}$ and i_0) a 1-D model was used. In order to have a known gas composition the polarisation curves of segment 9 and conditions 1-9 were used. Segment 9 is directly located at the entrance of the fuel gases therefore the composition of the fuel is known; the fuel utilisation being low no local effects are expected. For most of the measuring conditions the cathode was supplied with pure oxygen. Therefore the composition of the cathode gas is also known at segment 9. The temperature change during polarisation was taken into account for the validation measurements [43]. The results of the simulated and experimental validation conditions are shown in Figure 5-8.

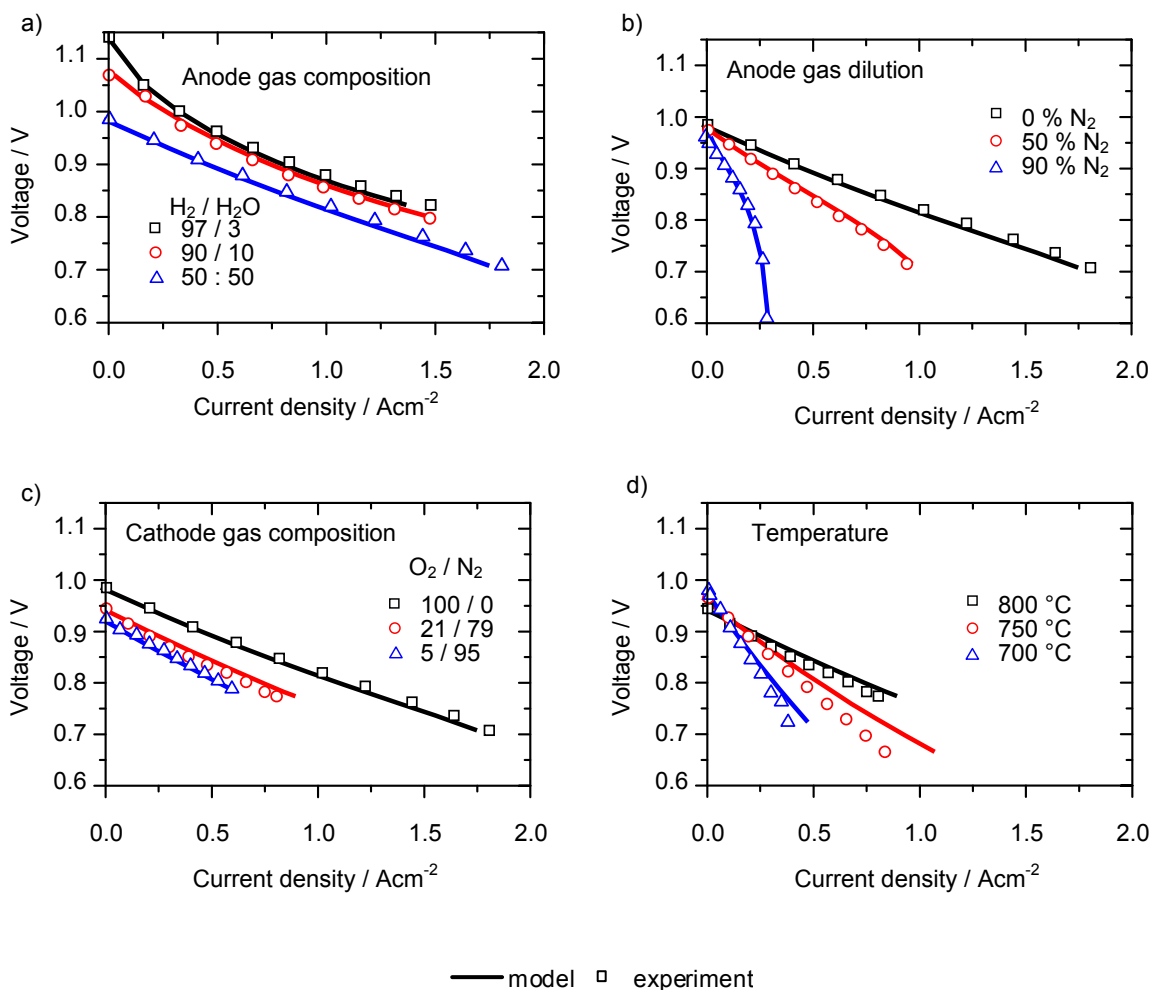


Figure 5-8: Comparison of experimental data under validation conditions (low fuel utilisation) and 1D model calculations. (a) Variation of anode gas composition without N₂ at 800 °C with cathode at 100 % O₂; (b) Variation of anode gas dilution with 50 % H₂ and 50 % H₂O at 800 °C and cathode at 100 % O₂; (c) Variation of cathode gas composition at 800 °C with anode at 50 % H₂ and 50 % H₂O; (d) Variation of temperature with anode at 50 % H₂ and 50 % H₂O and cathode air [45].

A good quantitative agreement between the model and the experiment can be seen for all operating conditions. For the temperature variations a deviation of the experiments towards lower voltages can be seen which is assumed to be due to an onset of cell degradation which is not included in the model.

5.5 High fuel utilisation

After the model parameters were calibrated measurements under more realistic conditions that is with higher fuel utilisation were done and compared to simulated i-V curves which were obtained with the calibrated model.

Figure 5-9 a) shows the global behaviour of the cell for operation with 0.5 l/min H₂, 1 l/min N₂, and 1 % H₂O. This condition was chosen as corresponding to a synthetic nitrogen-rich reformat gas. The cathode is supplied with 7 l/min air. The i-V curve has a typical shape displaying parabolic behaviour at low current densities and linear behaviour at medium current densities. The limiting current density would be just below 0.8 A/cm² and the cell has its maximum power density at about 700 mV.

In Figure 5-9 b) the local segment voltage of segments 9 to 12 is shown versus the global current density. Segment 9 is located at the entrance of the fuel gas; segment 12 is closest to the exit of the gases. Figure 5-9 c) shows the local voltage versus local current density.

The local i-V curves show a considerable variation depending on the position of the segment. They fan out and the local voltage drops earlier close to the exit of the fuel gases than at the entrance due to fuel depletion along the flow path.

Plotting the local voltage versus the global current density allows for a better comparison with the global polarisation curve at a given global current density which would be known in a non segmented cell, while current distribution is not. Plotting local voltage versus local current density includes additional information about the behaviour of the current density distribution. For example it can be seen that segment 12 which is closest to the exit shows a decreasing current density while the voltage continues to decrease. Global voltage versus local current density is not plotted here, but would facilitate an examination of the current density distribution at a given cell voltage.

The agreement between the experiment and the model is good both for the global as well as the local behaviour. The rapid decrease of segment voltage at the segments close to the fuel exit and the decreasing segment current under high polarisation is reproduced very well.

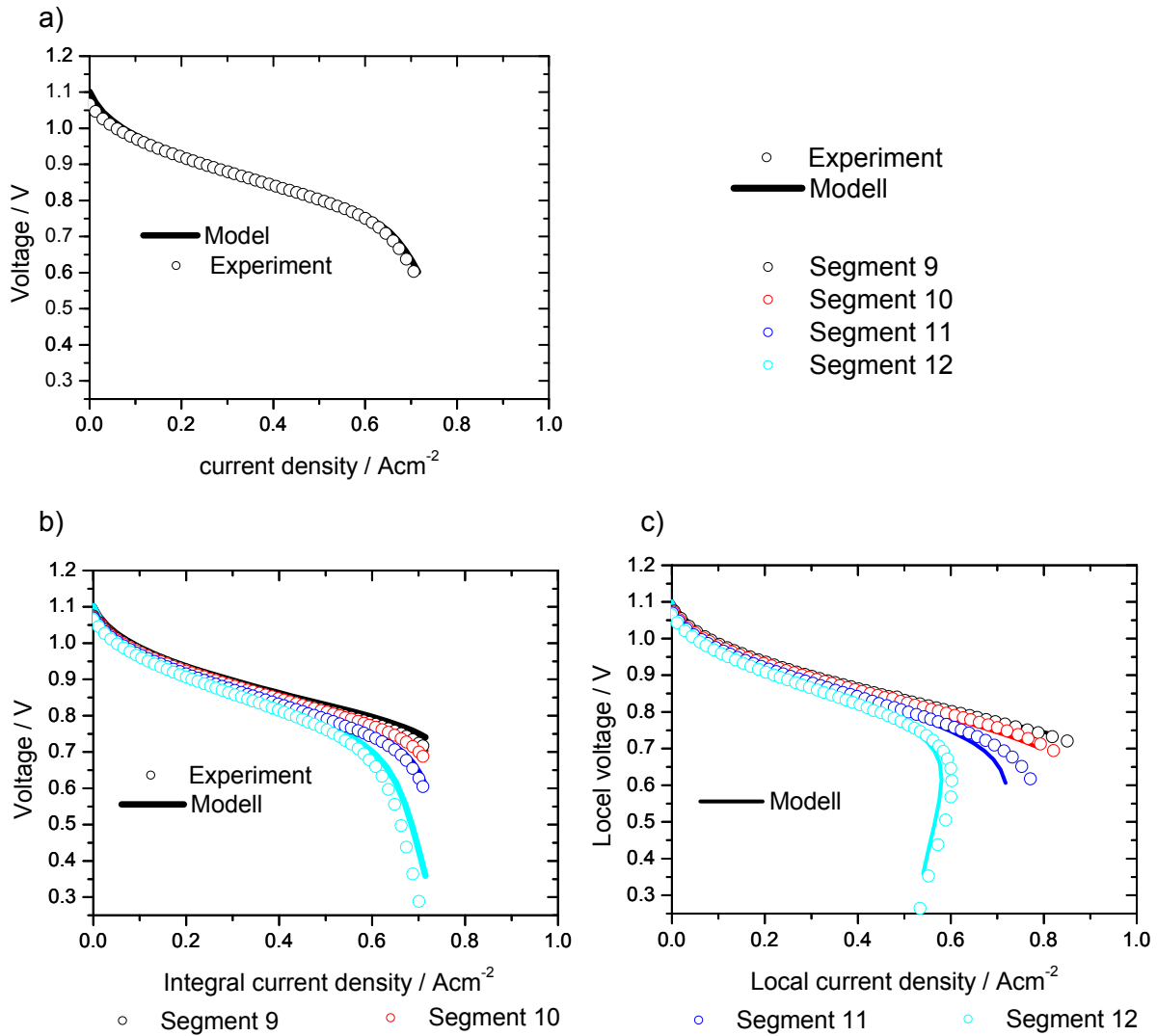


Figure 5-9: Global and local experimental and simulated polarisation curves. a) global behaviour, b) local voltage over global current density, c) local voltage over local current density. Square setup, counter flow operation; anode: 0.5 l/min H₂, 1 l/min N₂, 1 % H₂O; cathode: 7 l/min air.

At the cell's maximum current density the voltage of the last segment is already operated at very low voltages that must be considered critical. According to chapter 2.9 nickel oxidation is expected to take place at voltages below 0.679 V. It remains to be seen whether a local voltage below that value leads to local oxidation if the total cell voltage is still above the critical value.

Figure 5-10 shows the simulated distribution of voltage, current density and gas concentrations for a total cell voltage of 700 mV for the measurements conditions as in Figure 5-9. In the upper diagram the distribution of voltage and current density along the cell

is shown. It can be seen that both voltage and current density fall linearly from segments 1 to 3 and then drop strongly at segment 4. In the middle the concentration of hydrogen and water along the flow path are shown. Hydrogen enters from the left and is subsequently consumed and transformed into water. The concentration of nitrogen remains constant since there is no change in the number of moles. It is not shown here. In the lowest diagram of Figure 5-10 the concentrations of oxygen and nitrogen along the cathode are shown. The air enters from the right and the oxygen content decreases towards the left. The change is small since the cell is operated with surplus air.

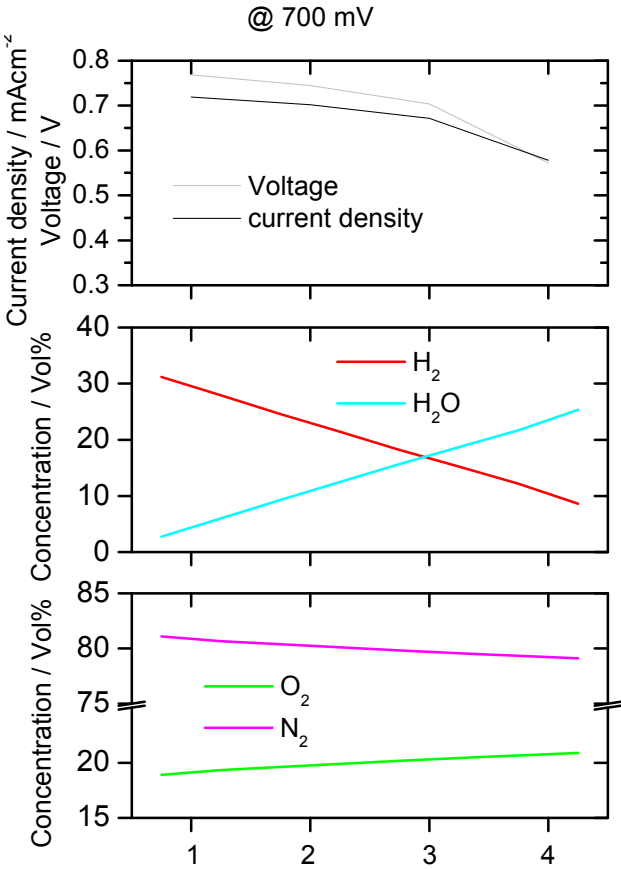


Figure 5-10: Simulation of voltage, current density, H₂ and H₂O at the anode and O₂ and N₂ at the cathode along the cell at total cell voltage of 700 mV. Square setup, counter flow operation; anode: 0.5 l/min H₂, 1 l/min N₂, 1 % H₂O; cathode: 7 l/min air.

Figure 5-11 shows the simulated spatially resolved distribution of the gas phase concentrations in the porous electrodes, the current collector meshes and the gas channels. Especially in the porous anode strong concentration gradients can be seen. The hydrogen content at each segment is more or less constant in the gas channel and mesh but changes through the thickness of the anode. At the last segment the hydrogen concentration at the electrolyte-electrode interface tends towards zero while water content is about 45 %. This

explains the strong decrease in segment voltage and current observed in Figure 5-9. This gas composition might also lead to the formation of nickel oxide and thereby to an increased degradation of the cell. It can be expected from these simulations that nickel oxidation begins to occur at the interface of anode and electrolyte at the end of the flow path and then spreads.

At the cathode only very slight gradients can be seen which is due to the high air flow rate and therefore the low oxygen utilisation. The cathode of this cell is thin compared to the anode which also decreases gradients through its thickness.

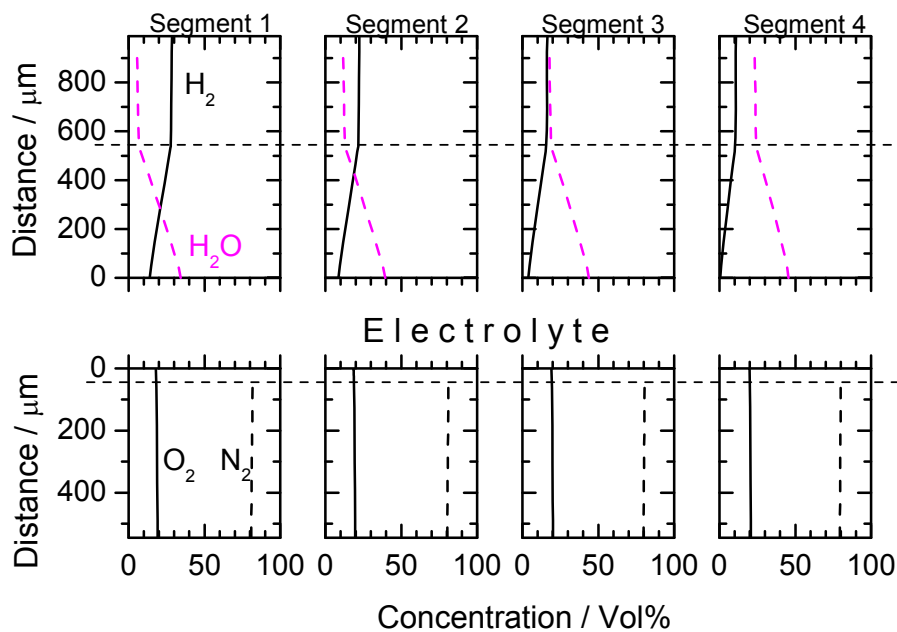


Figure 5-11: Gas concentration within the porous electrodes. Counter flow operation; anode: 0.5 l/min H₂, 1 l/min N₂, 1 % H₂O; cathode: 7 l/min air [45].

5.6 Parameter variations in simulation

Experimental variations of cell parameters or setup geometry are very time-consuming and costly. The validated model allows to qualitatively predict the behaviour of the cells if certain parameters are changed. In the following chapter some parameters like gas channels, electrode thickness and segmentation of the cell and setup are changed to show the possibilities the model offers and to examine the effects these parameters have upon the performance of the cell.

5.6.1 Variation of gas channels

A shallower gas channel results in a higher velocity of the gas flow. Figure 5-12 shows the simulated local i-V curves for two different channel areas. The total amount of fuel gas was kept constant at the value of chapter 5.5. The depth of the gas channel and the velocity of the gas were changed accordingly. It can be seen that this variation does not have any considerable impact on their course.

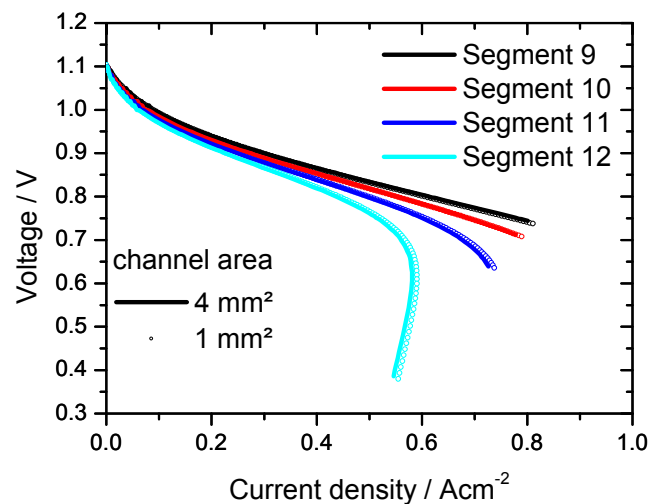


Figure 5-12: Simulated local i-V curves for channel areas of 4 mm² and 1 mm².

5.6.2 Anode thickness

A variation of the thickness of the anode has an influence on the local characteristic i-V curves. As can be seen in Figure 5-13 the thinner anode leads to a higher current density for all segments and the fanning out of the segments only starts at higher current densities. The thickness of the anode influences the limiting current density which is higher for a thinner diffusion layer. There is an increase in the maximum power density from 0.465 W/cm² for the 540 μm anode to 0.596 W/cm² for the 135 μm anode.

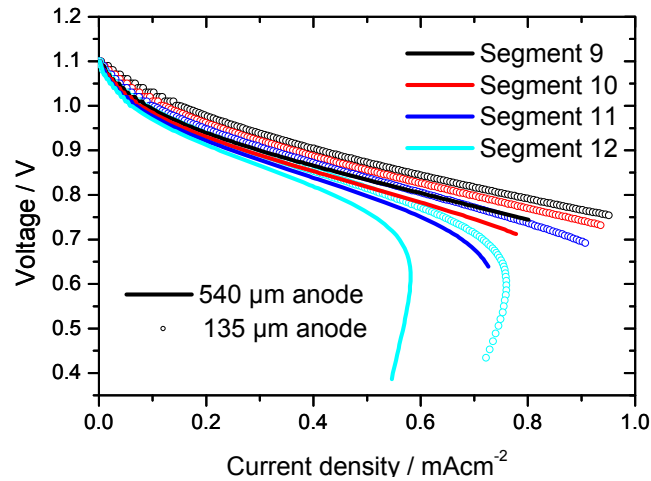


Figure 5-13: Simulated local current-voltage curves for anode thickness of 540 μm and 135 μm .

In Figure 5-14 the simulated contributions of the polarisation losses are shown for the last segment in the row, segment 12. The left diagram shows the losses for the 540 μm anode of the type A cell and the right diagram for the thinner anode of 135 μm .

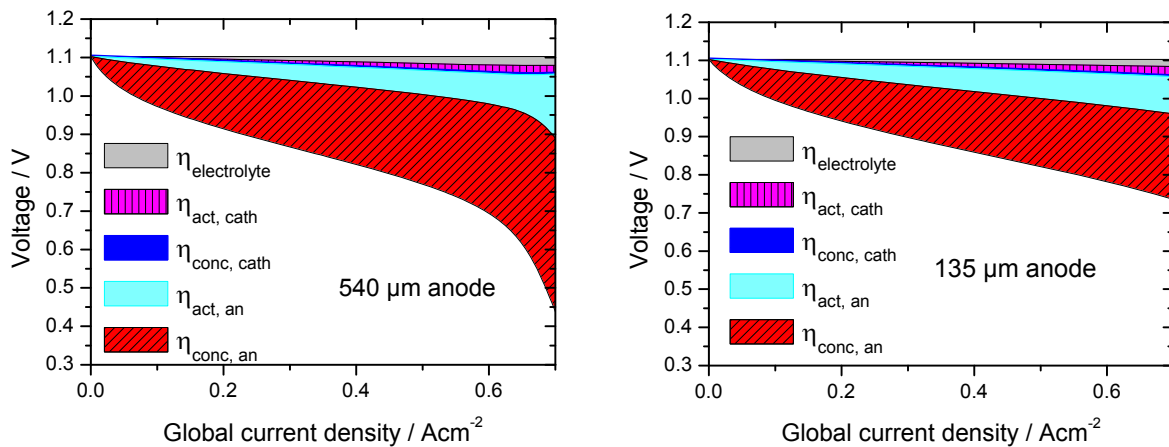


Figure 5-14: Simulated contributions of polarisation losses in segment 12 for anode thickness of 540 μm and 135 μm for operating conditions from chapter 5.5

Up to current densities of 0.6 A/cm^2 the only significant difference is that the thinner anode shows a decidedly lower concentration overpotential at the anode. At higher current densities it can be seen for the thick anode that anode activation overpotential is also increasing, which does not appear for the case of the thin anode, at least not at current densities in the regarded range. This increase in activation overpotential is due to the fact that the exchange

current density depends on the gas phase concentrations of H_2 and H_2O . It is shown by Bessler et al. that the exchange current density in an SOFC increases with a rising water content in H_2 and then drops again when a water content of about approximately 85 % is reached [51].

At a global current density of 0.7 A/cm^2 the total fuel utilisation and therefore the water content at the end of the cell is the same for both thicknesses. The distribution along the cell varies very little. A difference can be seen if the gradient within the porous anode is regarded. Figure 5-15 shows the simulated water content through the anode thickness and gas channel for segment 12 which is the last along the flow path. The water content is highest at the interface, and then drops throughout the anode thickness. To the right of the sharp bend is the contact mesh and the gas channel.

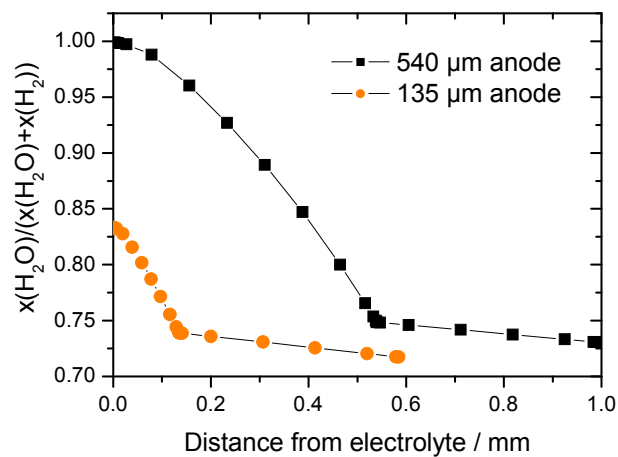


Figure 5-15: Simulated H_2O content through the porous anode and gas channel for an anode thickness of $540 \mu\text{m}$ und $135 \mu\text{m}$ at 0.7 V at the last segment.

For the thin anode the water content within the porous anode is lower and remains below 85% even at the interface of the electrolyte where water content is highest. For the thick anode there is no hydrogen left at the interface between electrolyte and anode and for a greater part the water content is above the 85 % for which the exchange current density starts to decline.

5.6.3 Cathode thickness

The influence of the thickness of the cathode is of interest because a thicker cathode reduces the chromium poisoning of the cathode in a metallic setup [52] but can lower the performance of the cell. For the air flow rate used in chapter 5.5 no difference in the local characteristic curves can be seen if the thickness of the cathode is doubled. If the thickness

of the cathode is increased to four times the initial thickness, a change in the i-V curves as in Figure 5-16 can be seen, especially of the segments close to the exit of the air. For segment 9 and 10 the beginning of a diffusion limitation can be seen, which does not appear for the thinner cathode. Under this operating condition the cell is supplied with a surplus of air. For lower air flows the effect might be stronger. The thicker cathode also results in a lower maximum power density of 0.447 W/cm² than the thin cathode which has a maximum power density of 0.465 W/cm².

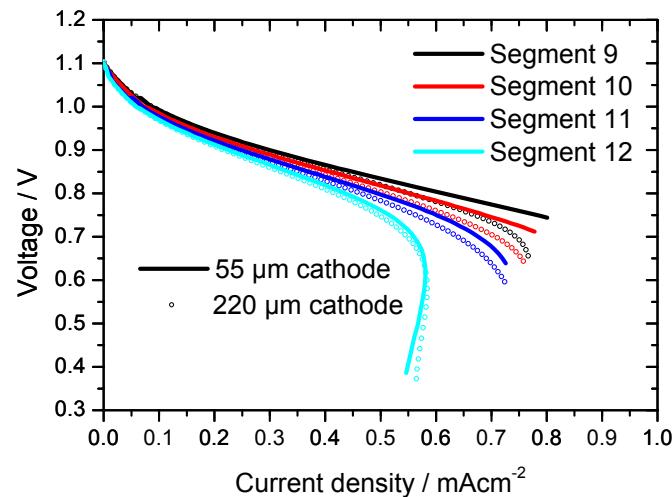


Figure 5-16: Local current-voltage curves for cathode thickness of 55 μm and 220 μm

In Figure 5-17 the simulated contributions of the polarisation losses are shown for the last segment in the row, segment 9. The left diagram shows the losses for the 55 μm thick cathode of the type A cell and the right diagram for the thicker cathode of 220 μm . At current densities of 0.65 A/cm² a strong increase of the cathode activation overpotential can be observed, while the other contributions are not affected. According to equation (4-9) the activation overpotential at the cathode side depends on the pressure of oxygen and the exchange current density. The concentration overpotential at the cathode does not increase because of the increase in thickness.

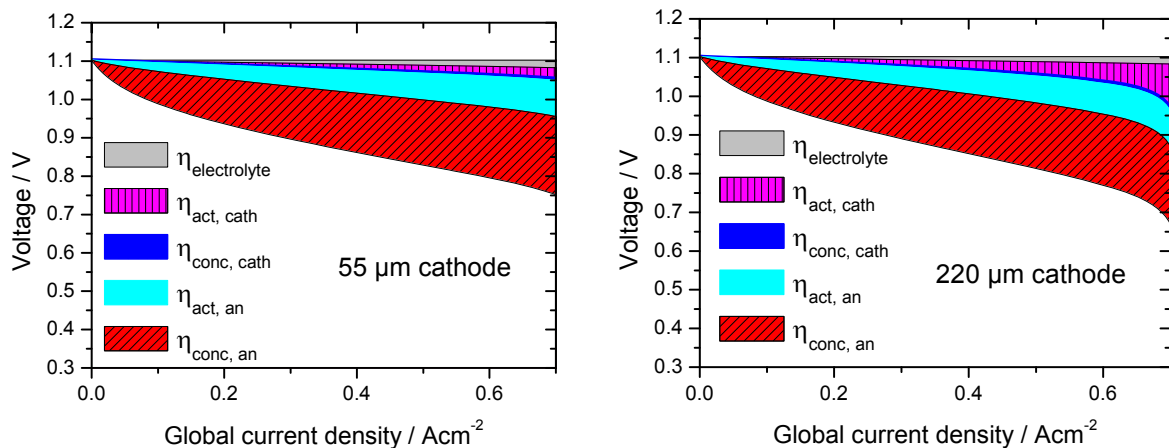


Figure 5-17: Simulated contributions of polarisation losses in segment 9 for cathode thickness of 55 μm and 220 μm for operating conditions from chapter 5.5

5.6.4 Non-segmented cell

In a real, unsegmented cell which is contacted on the anode side by a single nickel mesh and at the cathode side by one platinum mesh, gradients in voltage are compensated through the electrodes and contact meshes as already mentioned in chapter 3.9. Therefore the voltage distribution along the cell will be more homogeneous along the cell if the conductivity of contact meshes and bipolar plates is high. The same is not true for the distribution of current within the cell.

If the segmentation on the anode side or on both sides is removed from the model the current density distribution and the voltage distribution is affected. Figure 5-18 a) shows the simulated global and Figure 5-18 b) the local current-voltage characteristics for an unsegmented cell, a cell with a segmented cathode and a cell where both electrodes are segmented. The operating conditions are those from chapter 5.5. There is little difference in the global i-V curves. The segmentation does not significantly affect the global behaviour. There is however a considerable difference in the local i-V curves. For the first segment along the flow path the i-V curves do not differ in the shown range but the i-V curves of the following segments show a drop at lower current densities if the segmentation is removed. The additional lines in Figure 5-18 b) connect the operating points for the different segments at a global cell voltage of 0.7 V for the three configurations. The gradient of these lines is greatest for the configuration with segmented electrodes on both sides. It is smaller when only one electrode is segmented and the line becomes horizontal for the unsegmented electrodes and setup. These gradients are due to the resistances of the external wires through which equilibrating currents have to pass to compensate differences in voltage. For

the non-segmented setup it is assumed in this model that the voltage distribution is homogeneous since the whole cell is contacted with a continuous nickel mesh at the anode and a platinum mesh at the cathode both of which have very high conductivity.

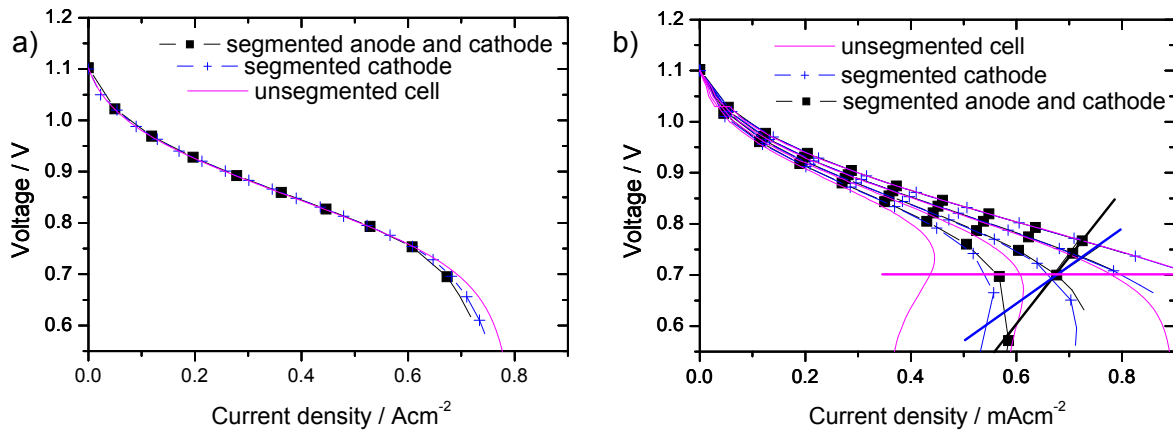


Figure 5-18: Global (a) and local (b) i-V curves with and without segmentation of electrodes. The additional lines in (b) connect the operating points of the different segments at a global cell voltage of 0.7 V.

Figure 5-19 shows on the left the distribution of the current density along the cell for the three configurations of the unsegmented cell, the segmented cathode and the segmented anode and cathode at a global cell voltage of 700 mV. On the right it shows the distribution of the voltage over the segments. For the unsegmented cell the current density declines constantly from the entrance of the cell to the exit while the voltage is constant over the whole cell. The segmented versions show a step-like behaviour both in current density and in voltage. The segmentation increases the inhomogeneity in voltage along the cell. The configuration in which both electrodes are segmented shows the greatest voltage difference along the cell. The voltage drops by 0.186 V from 0.769 V at the first segment to 0.583 V at the last. For the unsegmented anode and segmented cathode it drops from 0.757 V to 0.613 V which is a difference of 0.144 V.

If the current density distribution along the cell is regarded, then the slope for the non-segmented version is much greater than for the segmented anode and the cell that is segmented on both sides. For the unsegmented configuration the current density for segment 1 is about 0.22 A/cm² higher than in the simulation where both electrodes are segmented. At segment 4 the current density is by approximately 0.15 A/cm² lower.

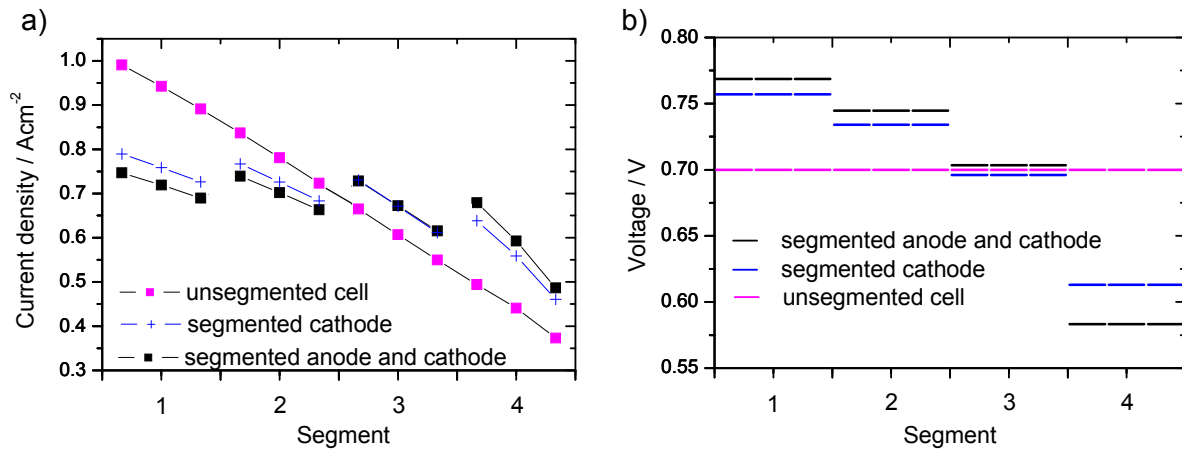


Figure 5-19: Simulated local current (a) and voltage (b) distribution with and without segmentation of electrodes.

The segmentation leads to a more even distribution of current density and a greater variation of voltage along the cell. Because of the equal voltage in the non-segmented configuration the first segment is forced to operate under a lower voltage than in the segmented version and therefore under higher current densities. For the last segment it is the other way round. It is operated under a voltage that is higher than for the segmented cell leading to a lower current. A higher current density at the beginning of the cell also uses a greater amount of fuel leaving a stronger depleted gas composition for the rest of the cell. It can also be seen that the current density at the end of one segment is lower than at the start of the next segment. This is due to the resistance of the wires. The average segment current density decreases along the flow path, therefore the potential drop over the wires decreases also leading to an increase in the segment current and a step from one segment to the other.

Figure 5-20 shows the influence the segmentation has on the distribution of the fuel hydrogen and the reaction product water along the flow path. Since the nitrogen content stays constant if hydrogen oxidation is the only reaction taking place it is not shown in the diagram. There is little difference between the configurations for one segmented electrode and two segmented electrodes. The unsegmented cell shows slightly higher fuel consumption especially at the beginning and therefore a stronger decrease in hydrogen content. At the end of the flow path the difference in hydrogen content between the three configurations decreases again.

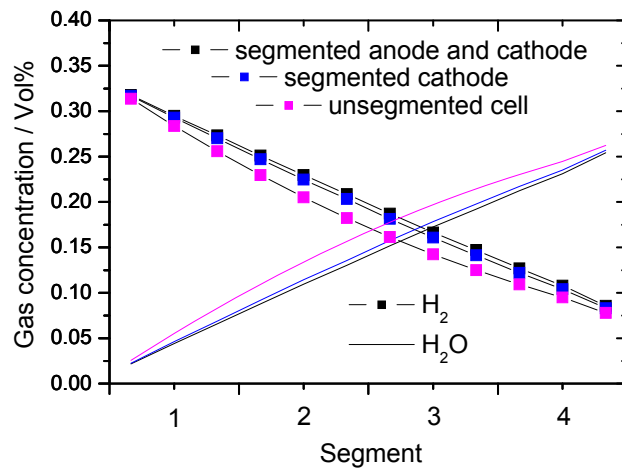


Figure 5-20: Simulated gas composition along the flow path with and without segmentation of electrodes.

It is to be expected that in a non-segmented setup the variation along the cell in voltage is far less pronounced than measured in the segmented setup. On the other hand the variation of current density is increased and the fuel consumption is greater. It can therefore be concluded that the local electrochemical oxidation of nickel due to low local voltage is not an issue for a non-segmented cell as long as the total cell voltage remains above the nickel oxidation voltage. The local chemical oxidation of nickel due to the gas composition and depletion of fuel still has to be considered especially as the higher current density at the entrance of the cell leads also to a greater consumption of fuel and an increase of reaction products.

6 Measurements with CO

For the fitting of the model parameters concerning the oxidation of CO further measurements were done. The conditions were chosen to avoid the formation of carbon at the cell or in the gas supply tubes. Carbon deposition in the cell may lead to cell damage and depositions in the tubes would change the composition of the gases reaching the cell, both of which had to be avoided. If only CO and CO₂ are present carbon deposition is possible via the Boudouard reaction given in equation (2-18). At room temperature the reaction is slow and carbon deposition is negligible. At higher temperatures the reaction rate increases and can no longer be neglected but at the same time the equilibrium moves towards CO at high temperatures [18].

The measurement conditions that were chosen can be seen in Table 6-1. To avoid the mentioned carbon deposition very low CO contents were chosen and the gas was diluted with nitrogen to further reduce the risk of carbon deposition. The CO/CO₂ ratio of the selected conditions varies between 0.03 and 0.14.

Nr.	Temp.	Anode			CO/CO ₂
		N ₂	CO	CO ₂	
	[°C]	ml/(min·cm ²)	ml/(min·cm ²)	ml/(min·cm ²)	
1	800	129	3.8	123	0.031
2	800	129	6.5	123	0.053
3	800	126	12.6	120	0.105
4	800	90	12.9	90	0.143

Table 6-1: Measurement conditions for CO and CO₂

Figure 6-1 shows the equilibrium compositions of the measuring conditions from Table 6-1 at different temperatures. The equilibrium was calculated with the open-source software CANTERA [20]. The calculations show that for all conditions in Table 6-1 the amount of carbon tends to zero for temperatures > 500°C. For inferior temperatures during the heating of the fuel gases the reaction rate of the Boudouard reaction is assumed to be negligible. The testing equipment can therefore be operated without carbon deposition in the cell or in the gas supply tubes.

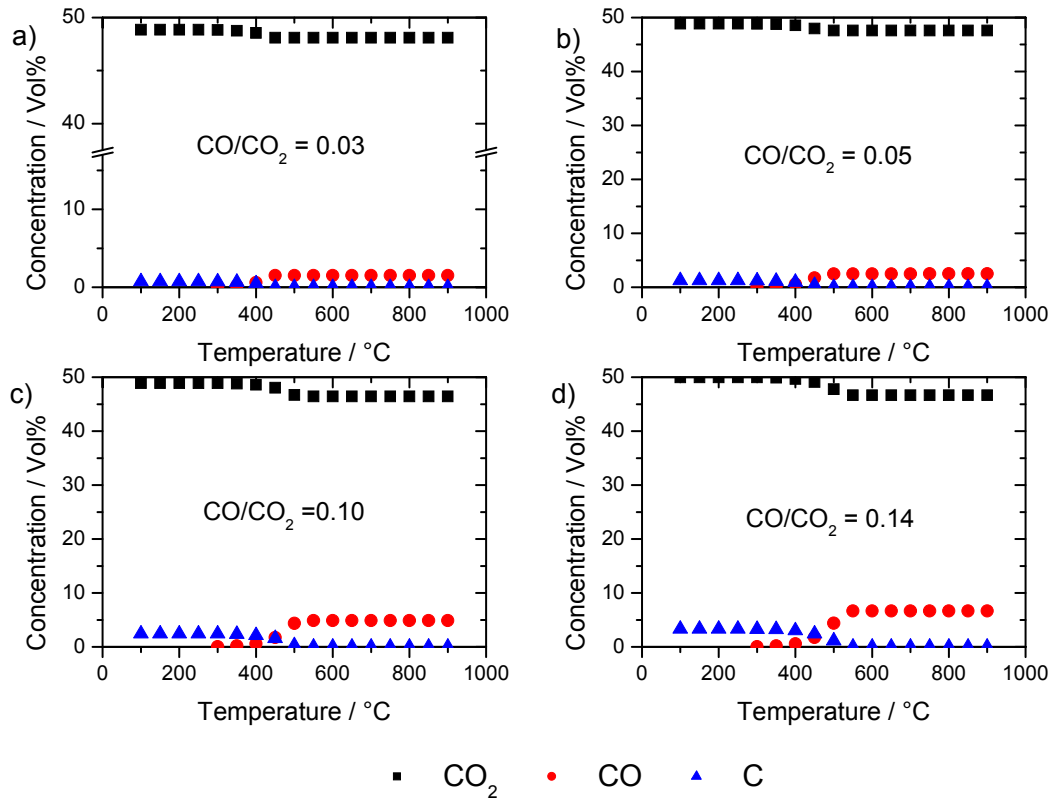


Figure 6-1: Equilibrium compositions of the measuring conditions as a function of temperature

6.1 I-V curves

Current-voltage characteristics were taken at all the measuring conditions given in Table 6-1. The integral current-voltage curves of the different CO/CO₂ ratios can be seen in the left part of Figure 6-2. As expected a lower CO content and lower CO flow rate lead to a lower OCV and a quicker decline of voltage when a current is drawn.

For low CO/CO₂ ratios plateaus can be observed at a voltage of 0.69 V in Figure 6-2 a) where the voltage stays constant for a rising current density before the voltage continues to drop. The higher the CO/CO₂ ratio is and the higher the CO flow rate the less pronounced is that plateau. This effect is reproducible and was measured in several cells. Once the current density is kept constant at its maximum value at the end of the i-V curve the voltage continues to decrease. The reason for this behaviour can not be found in a total depletion of fuel since the calculated fuel utilisation of CO is below 30%. It can be seen in the local i-V curves of the single segments which are shown in Figure 6-2 b) that the fuel utilisation is low and that there is no depletion of fuel. These local polarisation curves show little variation from the segment at the fuel gas inlet to the segment at the outlet. The plateau effect has also been observed for very low hydrogen contents in nitrogen in subsequent measurements,

therefore the reason is seen in the low fuel content rather than CO as fuel. A similar phenomenon was observed for SOFC stacks measured at DLR where plateaus were visible for some cells at high fuel utilisation.

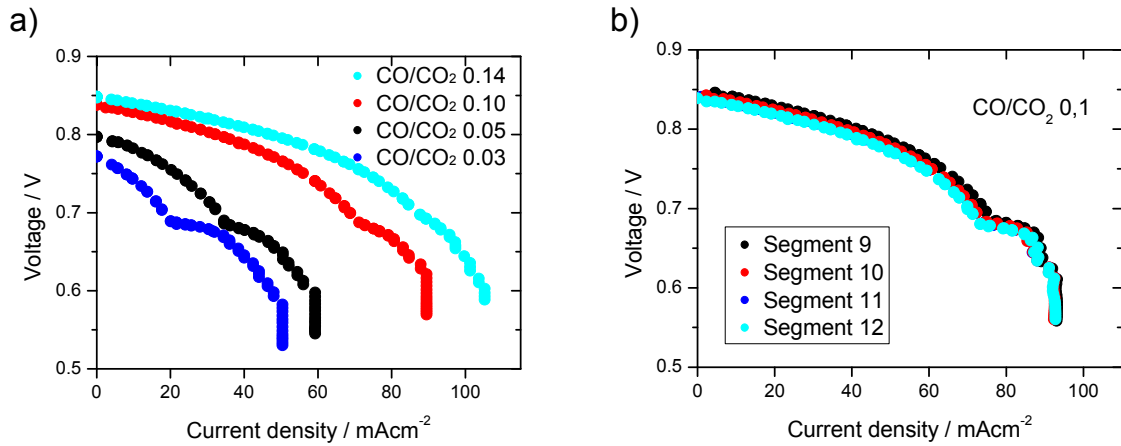


Figure 6-2: a) Global current-voltage characteristics for different CO contents b) local current-voltage characteristics for a CO/CO₂ ratio of 0.1 and low fuel utilisation.

6.2 Comparison of measurements and simulations under CO/CO₂ conditions

Figure 6-3 shows the experimental data and the corresponding simulations of the CO measurements. The circles represent the experimental data, the lines the simulation. The plateau-like behaviour of the experimental curves does not appear in the simulation. It is due to an effect which is not implemented in the model. The OCV and the i-V curve before the plateau show a qualitatively good agreement between the model and the experimental data especially at low CO contents.

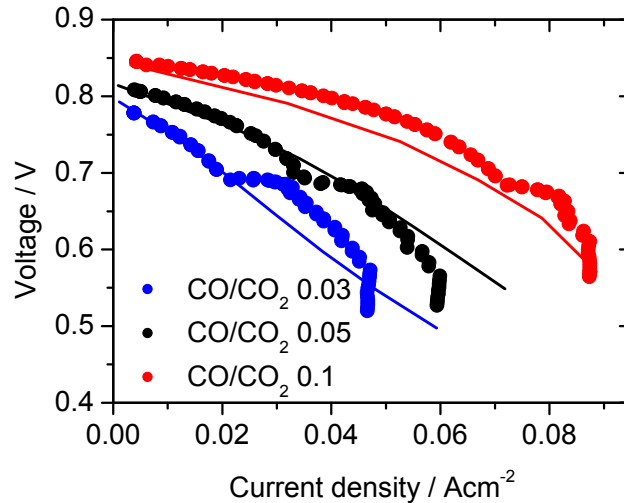


Figure 6-3: Experimental and simulated current-voltage curves for different CO/CO₂/N₂ mixtures.

6.3 Nickel oxidation at observed plateaus

In Figure 6-2 it can be seen that at the end of each i-V curve when the current remains constant the voltage continues to drop. Therefore another measurement was done where the current density is kept constant at various voltage values during the measurement to see a possible relation between the plateau-like behaviour and the decline of voltage at constant current density.

In Figure 6-4 the current density and voltage of this measurement are shown over time. The gas composition was that of the CO/CO₂ ratio of 0.14 from Table 6-1. Above 0.69 V the voltage remains constant as soon as the current does. Below 0.69 V the voltage keeps decreasing logarithmically even though the current is constant and it takes a while until equilibrium is reached.

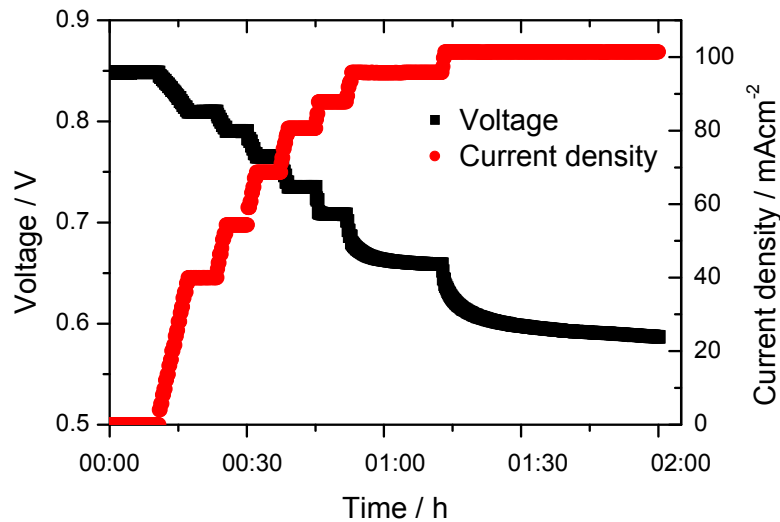


Figure 6-4: Voltage behaviour at various constant current densities. CO/CO₂ = 0.14.

A possible explanation is seen in the oxidation of nickel in the anode in addition to the oxidation of the fuel. The possible reactions taking place at the anode would then be not only (2-12) and (2-13) but also (6-1) and (6-2).



In this case nickel would behave like an additional fuel and the oxidation of nickel could for some time lead to an additional current that can be drawn at constant voltage as in Figure 6-2. This is only possible while the nickel oxide layer is not yet thick enough to deactivate the catalyst and increase resistance. The oxidation of nickel then leads to a deactivation of the catalyst nickel and an increase in polarisation and ohmic resistance, which would explain the gradual convergence of the voltage in Figure 6-4 towards a Ni/NiO/CO/CO₂ equilibrium since according to [53] the growth of a nickel oxide layer follows a parabolic law. The formation of nickel oxide is not implemented in the model. The experimentally observed plateaus can therefore not be obtained in the simulation.

Since the fuel content in the anode gases is very low, the case is similar to that of fuel starvation although the fuel utilisation remains below 40% of the initial CO. If there was no fuel in the anode gas the OCV at 800°C would be 0.679 V, which was calculated in chapter 2.9 and which was also determined experimentally. It is expected that at that voltage and below the nickel in the anode is oxidised even when fuel is present. The voltage of the nickel

oxidation coincides with the voltage of the experimentally observed plateaus, making nickel oxidation a plausible explanation.

The formation of nickel oxide depends on the gas composition and on the voltage of the cell. Whether the gas composition leads to an oxidation of the cell may be calculated or it may be estimated from the Ellingham diagram shown in Figure 2-5. From the Ellingham diagram it can be seen that the CO/CO₂ ratio for which nickel would be oxidised chemically at 800°C is below 10⁻². This value is three times lower than the smallest CO/CO₂ ratio used in the experiments.

For the CO/CO₂ ratio of 0.03 the plateau appears at a current density of 20 mA/cm². This corresponds to a fuel utilisation of 36% and to a CO/CO₂ ratio of 0.019 at the fuel outlet. For the second highest CO/CO₂ ratio of 0.1 the plateau appears at 0.7 mA/cm² which corresponds to a fuel utilisation of 38% and a CO/CO₂ ratio at the fuel outlet of 0.06. For the CO/CO₂ ratio of 0.14 which is the highest and at which only a very slight plateau is visible the plateau appears at 90mA/cm² and a fuel utilisation of 27% resulting in a CO/CO₂ ratio of 0.1 at the fuel outlet. The gas composition at the exit of the cell is very close to the limit to an oxidising atmosphere if the cell is operated at current densities where the plateaus appear. It is therefore possible that the cell is oxidised due to the gas composition.

6.3.1 Impedance measurements at the plateau

To further support the theory of the nickel oxidation as the reason for the plateaus shown in Figure 6-2 impedance measurements were done for a CO/CO₂ ratio of 0.03 on one cell. The measurements were taken of the entire cell. Spectra were taken at 500 mA (8.3 mA/cm²) at which stage the system is still stable and at 1.1 A (18 mA/cm²) where the system changes with time. At the higher polarisation a series of six measurements were done one after the other to examine the time dependence. The time gap between the start of each measurement was about 4 minutes. The resulting impedance spectra of this series are shown in Figure 6-5.

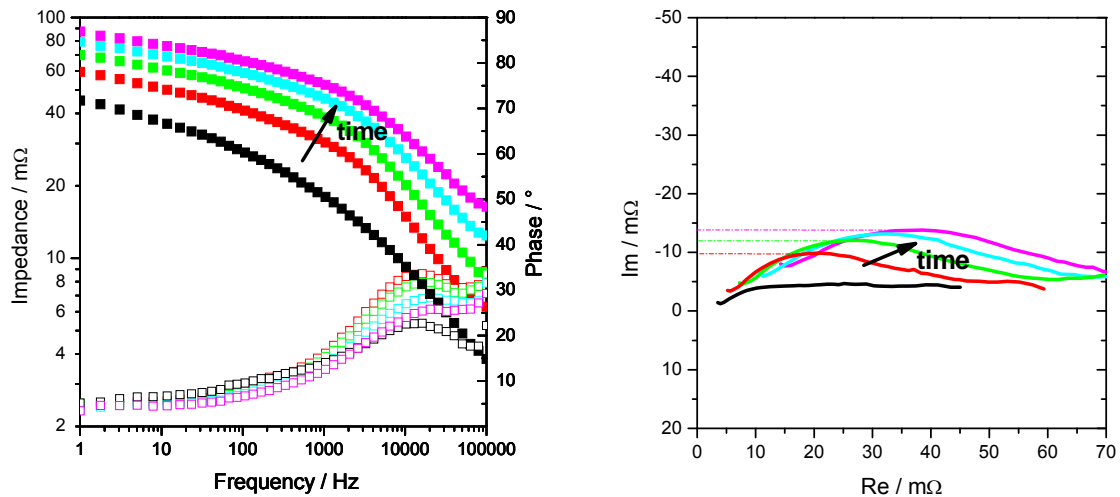


Figure 6-5: Impedance series of the entire cell at 18 mA/cm² (CO/CO₂ = 0.03).

With time which is indicated by the arrow in Figure 6-5 the curves are displaced towards higher impedances. The impedance at high frequencies corresponds to the ohmic resistance of the cell. It can easily be seen in the left diagram of Figure 6-5 that the impedance at high frequencies rises with time. This increase of the ohmic resistance was linear as is shown in Figure 6-6. Since conductivity of nickel oxide is very low, an increase of nickel oxide and decrease of the well conducting nickel is a plausible explanation of the observed increase in ohmic resistance.

The Nyquist diagram on the right of Figure 6-5 shows plainly a growth of the somewhat flattened semicircle. According to chapter 3.6.1 the height of that semicircle is one half of the charge transfer resistance. This growing of the charge transfer resistance of the cell can be caused by a reduction of the catalytically active surface in the anode because nickel is transformed into non-active nickel oxide. Figure 6-6 shows the increase of the charge transfer resistance obtained from the impedance measurements. It shows a logarithmic behaviour as would be expected from literature for the growth of a nickel oxide layer.

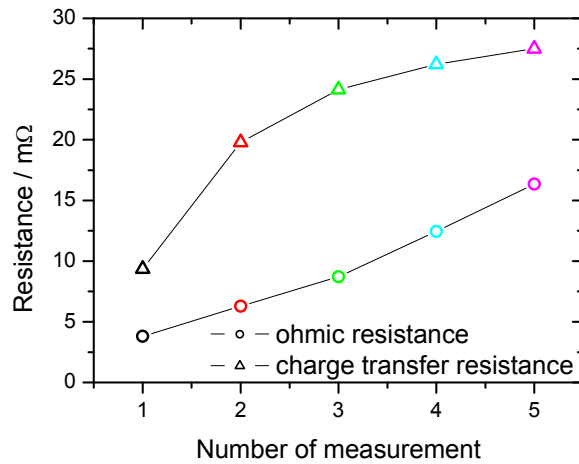


Figure 6-6: Development of ohmic resistance and charge transfer resistance during impedance series of the entire cell at 18 mA/cm². CO/CO₂ = 0.03.

After the strong polarisation was removed the system returned to normal as can be seen in Figure 6-7 which shows the impedance spectra before and after the experiment. The effect was therefore completely reversible and no lasting damage was done to the cells.

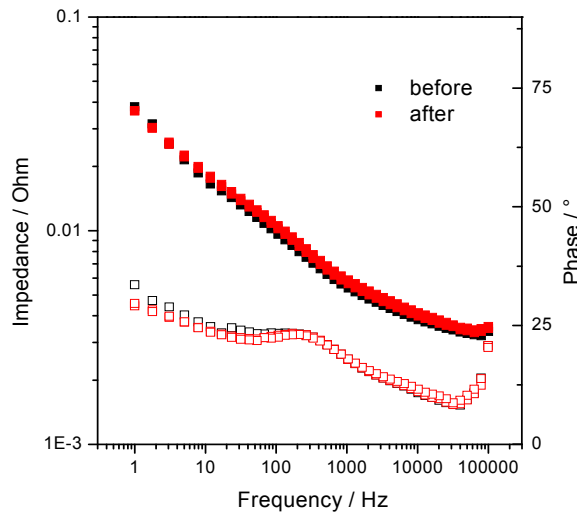


Figure 6-7: Impedance spectra at 500 mA before and after polarisation of 1100 mA. CO/CO₂ = 0.03.

7 Methane as fuel

An advantage of SOFC in comparison with other fuel cells is the possibility to use not only hydrogen as a fuel but also fuels containing hydrocarbons e.g. methane or methanol. These can be internally reformed at the cell. The internal reforming of methane (CH_4) especially is of great interest, since it is the main component of natural gas and biogas. The availability is therefore good and an infrastructure for its distribution already exists. During the internal reforming water-gas shift and reforming reactions take place at the anode in addition to the cell reaction. They are coupled to diffusive and convective transport processes and may lead to a variation of temperature and gas-phase species along the flow channel and through the anode thickness and are therefore expected to present an additional stress on the cell.

7.1 Experiments and simulations

Experiments were conducted in counter flow operation for various fuel compositions of methane/steam mixtures with steam to carbon ratios of 1, 2 and 3. The amount of CH_4 for condition 1, 2 and 3 was kept constant at 0.085 l/min and was diluted with 0.004 l/min of N_2 to obtain a mixture corresponding to natural gas. The amount of water was varied accordingly. Unless stated otherwise the experimental results shown were obtained with a nickel contact mesh. The cassette design setup and type A cells were used for experiments and simulations. All simulation results shown are calculated under the assumption of isothermal conditions.

7.1.1 Carbon deposition

To assess the risk of carbon deposition in the cell the equilibrium compositions of the chosen measuring conditions were calculated with CANTERA [20]. Figure 7-1 shows the equilibrium over temperature for the three conditions.

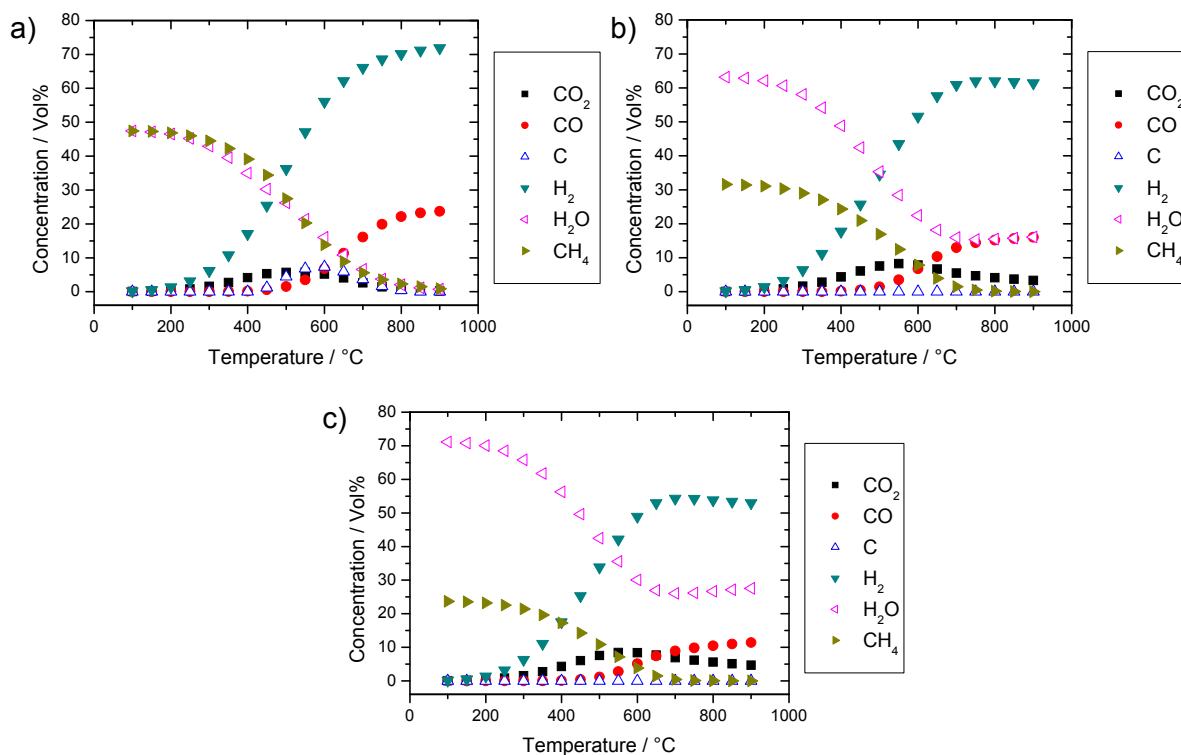


Figure 7-1: Equilibrium compositions over temperature for measuring conditions with $S/C = 1$ (a), 2 (b) and 3 (c).

At 800°C there is no water left for $S/C = 1$ but there is still a little methane. For higher S/C ratios the methane is completely reformed at 800°C and not all the water is consumed. It can be seen in Figure 7-1 a) that for an S/C ratio of 1 there is carbon deposition possible at temperatures between 450 °C and 750 °C. For higher S/C ratios this is no longer the case. It can therefore be assumed that no carbon deposition will occur at the anode for the chosen conditions of $S/C = 2$ and 3 while it can not be entirely excluded that some carbon deposition will occur in the tubes and at the cell for $S/C = 1$.

7.1.2 Current voltage curves

Figure 7-2 shows the simulated and measured global i-V curves for different S/C ratios. For simulation the model from chapter 4 was used. The curves show the typical shape that would be expected from a normal non-segmented cell. A parabolic behaviour at low current densities can be seen for $S/C = 1$. This parabolic behaviour is less pronounced for higher water contents. At intermediate current densities a linear behaviour can be seen. The curves for all S/C ratios have the same limiting current density of slightly above 0.6 A/cm² in the simulation.

There is a good agreement between the modelled and the experimental curves. The higher the water content, the lower is the OCV of the cell. The experimental OCVs are slightly lower than the modelled ones. The difference between the single i-V curves decreases with increasing current densities. The higher the current density the smaller is the influence of the water content, all simulated curves reaching the same limiting current density. The simulated curves tend to reach the diffusion limit at lower current densities than the experimental curves.

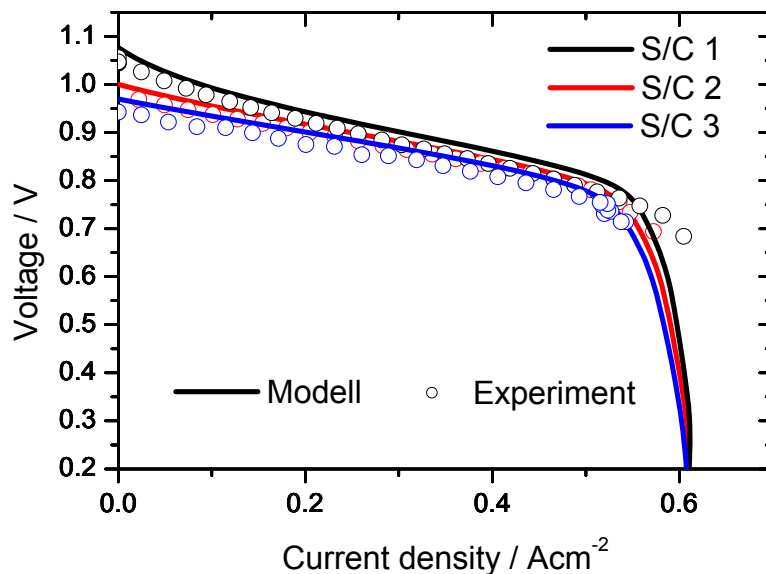


Figure 7-2: Comparison of the simulated and experimental global i-V curves for S/C = 1, 2 and 3. Counter flow operation; anode: 0.085 l/min CH₄, 0.004 l/min N₂; cathode: 8 l/min air; T = 800 °C.

On the left side of Figure 7-3 the simulated and measured global i-V curves can be seen for S/C ratios of 1, 2 and 3. The corresponding local i-V curves for one row of segments from the fuel inlet to the outlet are shown on the right. Here the local segment voltage is plotted versus the local segment current. Segment 9 is located at the entrance of the fuel gas; segment 12 is closest to the exit of the gases. The local i-V curves show a considerable variation depending on the position of the segment. They fan out and the local voltage drops at lower current densities close to the exit of the fuel gases than at the entrance. Segment 12 which is closest to the exit even shows a decreasing current density while the voltage continues to decrease. This behaviour was already seen in chapter 5.5 and is due to a strong depletion of fuel at the end of the flow path.

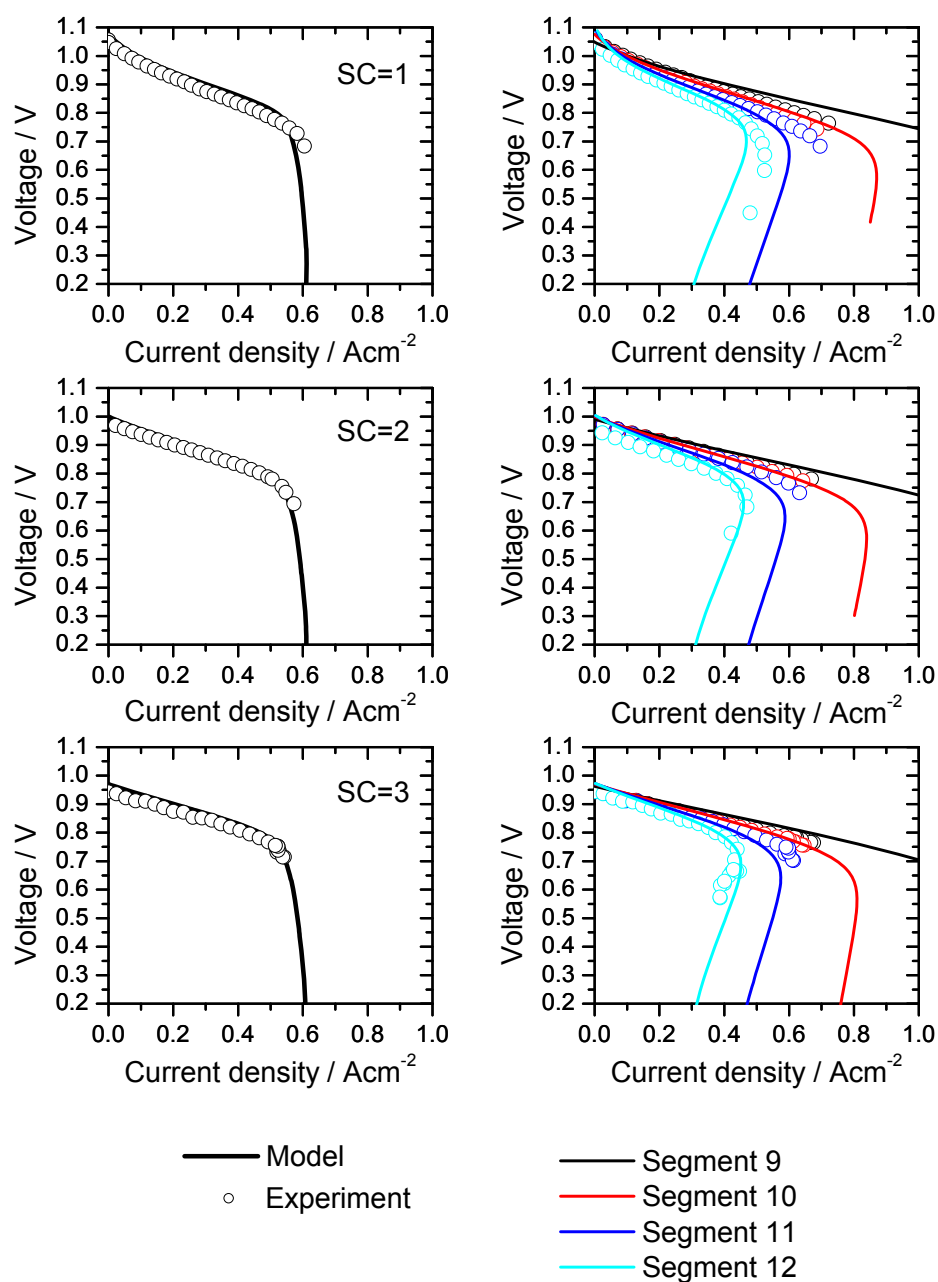


Figure 7-3: Experimental and simulated polarisation behaviour for S/C 1, 2 and 3. Left: global current-voltage curves; right: corresponding local segment voltage versus local segment current. The numbers indicate the segments, where segment 9 is the first in flow direction of the fuel gas (counter flow operation; anode: 0.085 l/min CH₄, 0.004 l/min N₂; cathode: 8 l/min air; T = 800 °C).

The global i-V curves show a good agreement between the simulated and the measured curves. For the local i-V curves a quantitatively good agreement can be observed which is best for an S/C ratio of 2. The experimental curves of segment 9 which is located at the

entrance of the fuel gases are slightly below the simulated curve for all conditions. Simulated and experimental curves match excellently for segment 10, while segment 11 tends to better experimental values than the simulated ones under all conditions. Segment 12 shows an excellent agreement between modelled and measured curves for an S/C ratio of 2. For S/C = 1 it shows higher measured current densities and for S/C = 3 the current density recedes slightly stronger in the experiment than in the model.

Figure 7-4 shows the simulated spatially resolved distribution of gas-phase concentrations in the porous electrodes and current collector meshes at 700 mV for an S/C ratio of 1 on the left and S/C 3 on the right. The anode has a thickness of 540 μm ; further to the right are the contact mesh and the gas channel.

The CH_4 content is low even in the gas channel and even for segment 1. Gradients in gas composition are visible within the relatively thick anode. A decrease of H_2 and CO through the anode thickness and a corresponding increase of water and CO_2 can be seen. At segment 3 and 4 concentration of fuel (e.g. H_2 and CO) are very low. For segment 4 the concentration of H_2 and CO even reaches zero at the electrolyte/electrode interface, which explains its low current density and voltage.

Such a strong fuel depletion is expected to lead to nickel reoxidation at the anode. It can be taken from the Ellingham diagram (Figure 2-5) that a $\text{H}_2/\text{H}_2\text{O}$ ratio below 10^{-2} Pa at 800°C will lead to oxidation of nickel. The $\text{H}_2/\text{H}_2\text{O}$ ratio at segment 4 is lowest since part of the H_2 is already transformed into H_2O . For the steam to carbon ratio of 1 an $\text{H}_2/\text{H}_2\text{O}$ ratio of $7.67 \cdot 10^{-4}$ just under the electrolyte is definitely a condition under which nickel oxide is formed. In the gas channel the gas composition yields an $\text{H}_2/\text{H}_2\text{O}$ ratio of $8.3 \cdot 10^{-2}$ which is still very close to nickel oxidising conditions. It can therefore be expected that nickel oxidation will occur under the given conditions at the anode, especially at the last segment and directly at the electrolyte interface. For the S/C ratio of 3 the $\text{H}_2/\text{H}_2\text{O}$ ratios at segment 4 are even lower than for S/C = 1 increasing the probability of nickel oxide formation.

The critical situation at segment 4 is not visible from the global i-V curve as was seen in Figure 7-2. The cell is operating locally under critical conditions while the global behaviour is apparently not critical. The influence on local degradation still has to be studied.

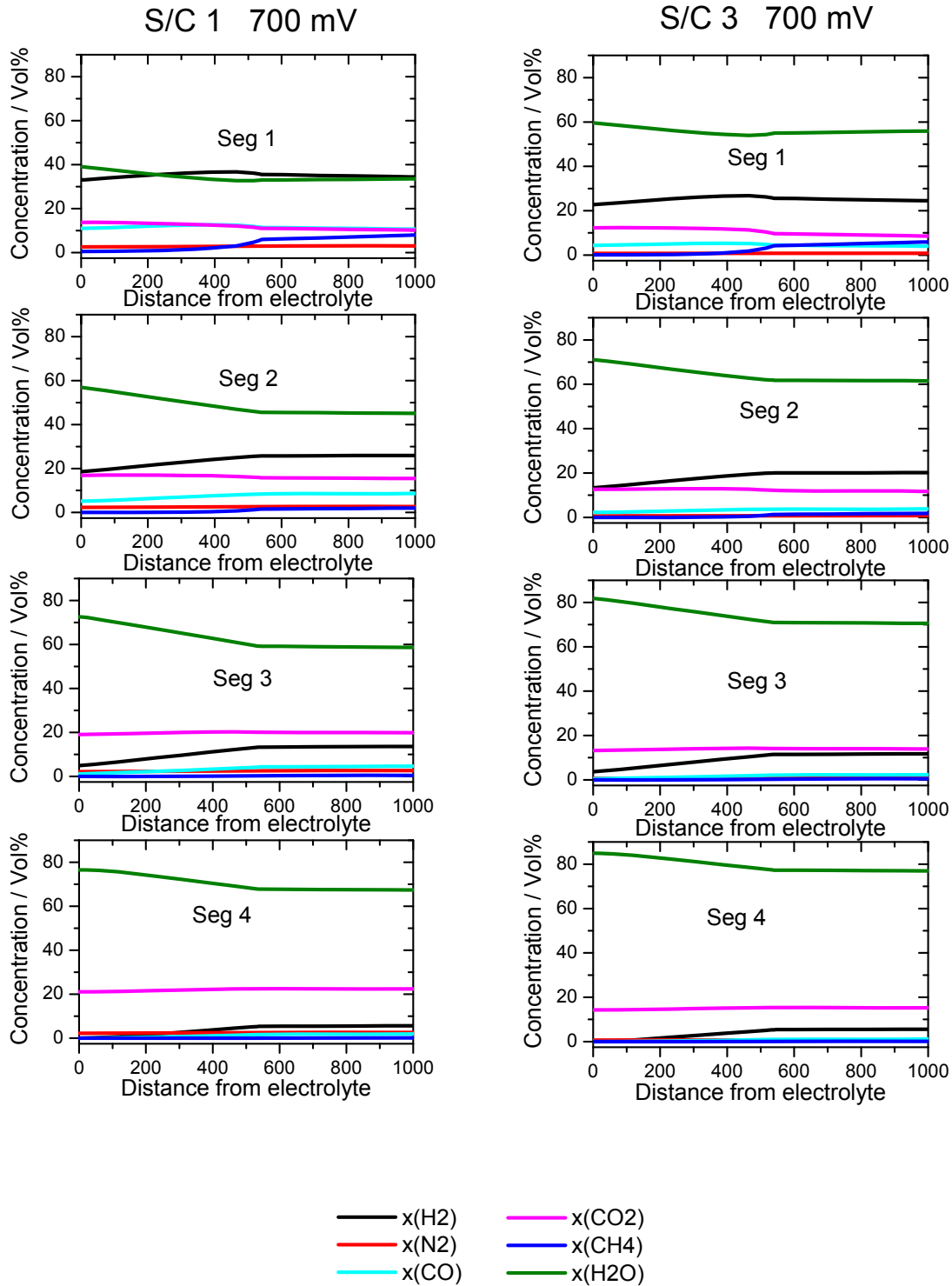


Figure 7-4: Simulated distribution of the local gas concentrations within the porous anode and the gas channel for a cell voltage of 700 mV for S/C ratios of 1 and 3 (counter flow operation; anode: 0.085 l/min CH₄, 0.004 l/min N₂; cathode: 8 l/min air; T = 800 °C).

7.2 Gas composition at OCV - Reforming along the cell

Figure 7-5 shows a detail of the simulated i-V curve shown in Figure 7-3 with a steam to carbon ratio of 1. It can be seen that the OCV varies within the cell. It is lower at the entrance than at the exit because the reforming reaction takes place at the entrance of the cell resulting in variations in fuel composition as will be seen in Figure 7-6. In the experiments this effect could not be observed.

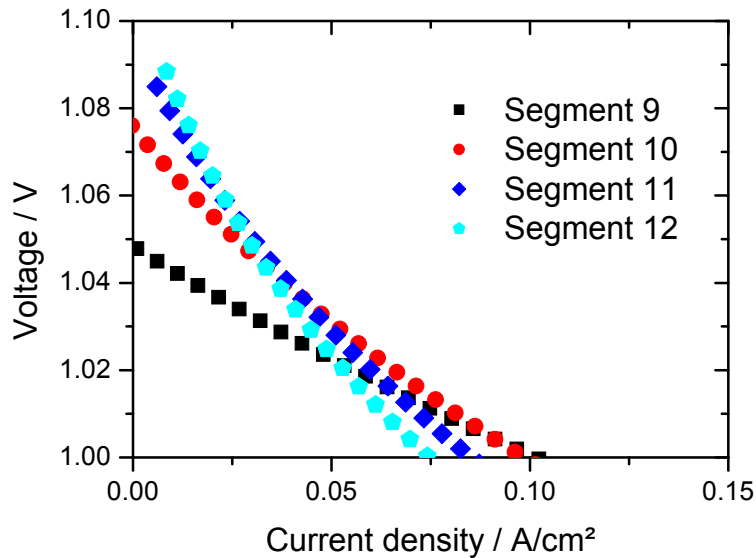


Figure 7-5: Detail of the simulated polarisation behaviour for S/C = 1 (counter flow operation; anode: 0.085 l/min CH₄, 0.004 l/min N₂; cathode: 8 l/min air; T = 800 °C).

To determine where and how fast the methane was reformed at the cell gas samples were taken at OCV of two rows of segments for all conditions and analysed with the gas chromatograph. Figure 7-6 shows the measured and simulated fuel gas composition along the flow path at OCV for S/C ratios of 1, 2 and 3. Since the gas chromatograph is not capable of measuring water, water is not included in the diagrams and the simulated values are adapted accordingly.

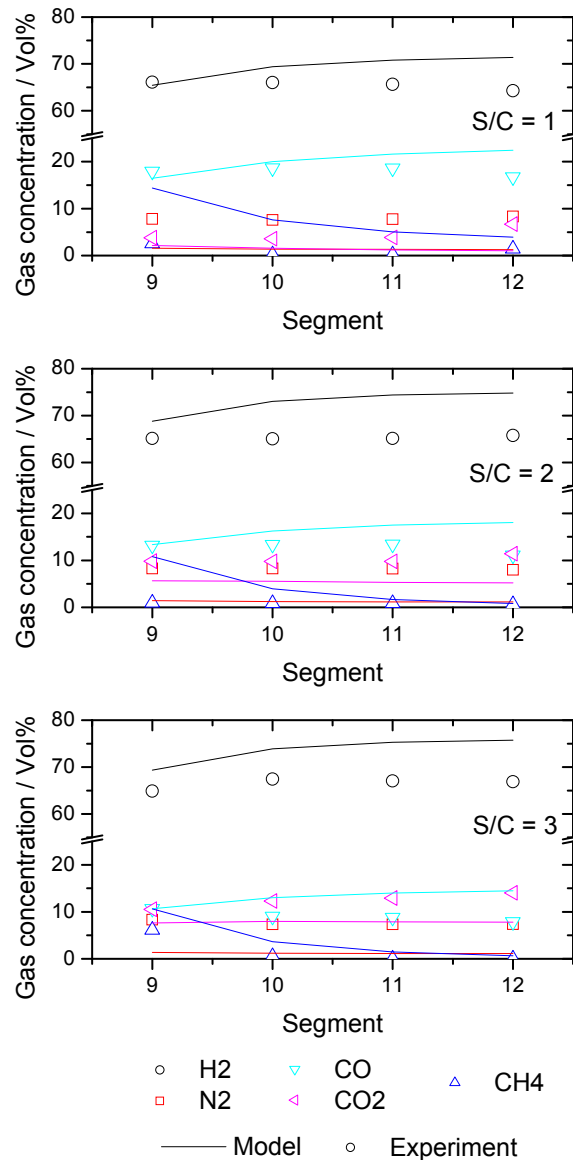


Figure 7-6: Comparison of measured (symbols) and simulated (lines) gas composition along the flow path at OCV for S/C = 1, 2 and 3. Water is not included in the diagrams (counter flow operation; anode: 0.085 l/min CH₄, 0.004 l/min N₂; cathode: 8 l/min air; T = 800 °C).

By comparing the methane content along the cell it can be seen that the reforming process is faster in the experiment than in the model. The model predicts more than 10 % CH₄ at the first segment for all three conditions. The measured values at the first segment stay below that value. The difference is especially big at S/C = 1 where the CH₄ is highest for the simulation. A possible explanation is, that the methane is not only reformed at the nickel of the anode, but also at the nickel contact net, which is not considered to have any catalytic

activity in the model, or that reforming already starts in the tubes leading towards the cell. Since it is not possible to measure the gas composition just before the cell this possibility can neither be proven nor discarded. Another possible explanation can be found if the content of nitrogen is observed. The measured values for nitrogen and CO₂ are much higher than is to be expected from the model. Between 7.3 and 8.3 % of nitrogen is found in the fuel gas while the simulation gives values below 1.6 % for all conditions and segments. The values for CO₂ are also about twice as high in the experiments as in the simulation. The higher amount of nitrogen and CO₂ might be due to air leaking into the fuel somewhere before the fuel enters the cell. A leakage of air would explain the amount of nitrogen and the oxygen contained in the air would lead to an increase in reaction products, e.g. CO₂ and water because part of the methane is burned before reaching the cell. The nitrogen content stays more or less constant along the flow path which is an indication that the leakage takes place before the fuel gas enters the cell and not along the cell itself. The higher concentrations of N₂ and CO₂ lead to a decreased value for the other contents explaining why they stay below the simulated values.

If the water content is disregarded as in this consideration the difference in fuel composition is rather small for the different S/C ratios. The S/C ratio does not seem to have a major influence on the internal reforming of methane at the cell.

7.3 Polarisation

Figure 7-7 shows in the upper part the voltage and current density for an S/C ratio of 1 (left) and 3 (right) at 700 mV. At this condition the current density of the last segment in the row is already below its maximum as can be seen in the local polarisation curves in Figure 7-3. For both conditions the voltage and the current density drop at the last segment.

In the experiments as well as in the simulation the difference between the voltage of segment 9 and segment 12 is greater for S/C = 1 (difference of 0.24 V in experiment and 0.37 V in simulation) than for S/C = 3 (difference of 0.17 V in experiment and 0.29 V in simulation). The voltage inhomogeneity is slightly lower in the experiments than in the simulation. There is also a similar difference in the distribution of the current density between an S/C ratio of 1 and 3. The current density difference between segment 9 and 12 is slightly greater for S/C = 1 (difference of 0.265 mA/cm²) than for S/C = 3 (0,214 mA/cm²). As could already be seen in Figure 7-2 the total current density level is lower for S/C = 3 than for S/C = 1. A slightly more even distribution is therefore obtained at a slight loss in power density.

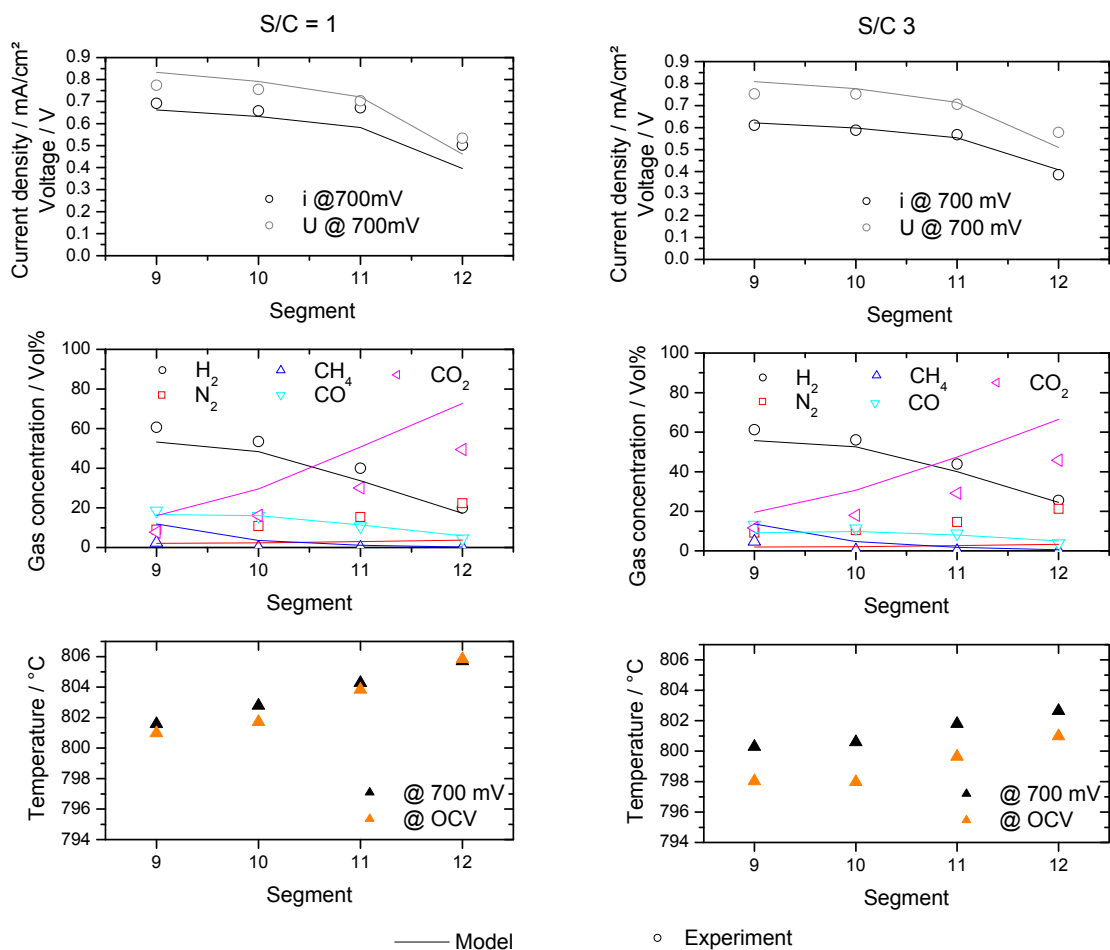


Figure 7-7: Comparison of measured (symbols) and simulated (lines) voltage, current density, gas composition and measured temperature at a cell voltage of 700 mV for S/C ratios of 1 and 3 (counter flow operation; anode: 0.085 l/min CH₄, 0.004 l/min N₂; cathode: 8 l/min air; T = 800 °C).

Figure 7-7 shows in the middle the fuel gas composition along the flow path for S/C ratios of 1 and 3 at 700 mV. The water content is not considered in the diagrams. For hydrogen and CO the agreement between the model and the experimental data is very good. Like in the OCV measurements the methane is reformed quicker in the experiment than in the model. CO₂ production is stronger in the model than measured in the experiments while a decidedly larger amount of nitrogen was measured than expected indicating a possible leakage of air to the anode. An increase of nitrogen can be seen along the cell which did not appear during the OCV measurements. This is due to the formation of water when hydrogen is consumed. When all methane has been reformed the number of moles remains constant. A decrease of H₂ and a consequent increase of steam which is not measured leads to a measured increase of the other species. If the water content is not regarded, the difference in gas composition is

very similar for different S/C ratios. The only significant difference that might lead to any local effects is therefore the water content and because of the water content the velocity of the flow.

For the experiments an increase of temperature within the cell has been observed both at OCV and at polarisation. The temperatures are shown in the lower diagram of Figure 7-7. The increase was basically the same for OCV and polarisation, indicating that this temperature gradient is due to the reforming reaction and a resulting temperature drop at the entrance of the cell rather than polarisation. The increase in temperature was observed for all S/C ratios although only S/C = 3 and S/C = 1 are shown. The temperature increase is below 5°C justifying the neglect of temperature change in the simulations. It is to be expected that this temperature increase will have a stronger effect in a stack with less thermal mass around the cell and several cells close together than in the present setup. The global temperature measured is slightly lower at an S/C ratio of 3 than at S/C = 1. This is assumed to be due to the imperfect preheating of the fuel gases before entering the cell.

7.4 Influence of flow rate and water content

In Figure 7-7 a higher voltage inhomogeneity was observed for S/C = 1 in comparison with S/C = 3 in the experiments as well as in the simulations. To determine whether this is due to the water content or to the increased flow rate or both, a simulation was done in which 0.17 l/min N₂ was added to the S/C = 1 condition. Now the total flow rates equals that of the S/C = 3 condition in Figure 7-7.

Figure 7-8 shows the results for the condition of S/C = 1 with additional nitrogen as well as the curves for S/C = 1 and S/C = 3 from Figure 7-7. The left diagram of Figure 7-4 a) shows the local voltage at a global cell voltage of 700 mV. On the right side the local current density is shown for the same global voltage. The local voltage of the nitrogen-diluted S/C = 1 condition lies for all segments between the voltage of the other two conditions although it is a bit closer to the line of S/C = 3. For the voltage the higher flow rate as well as the water content seem to have an influence on the distribution even though the flow rate has the greater one. In the current density diagram on the right of Figure 7-4 a) the difference between the current density values for S/C = 3 and S/C = 1 with nitrogen is very small. S/C = 3 still shows a slightly more even distribution. The difference in the current density of the S/C ratio of 1 is more pronounced. For the first three segments the current density is higher for this condition than for the other two dropping strongly at the last segment to a value even slightly below the value of S/C = 1. The main difference both for the voltage as well as for the current density distribution is due to the flow rate. The higher flow rate obtained by more

water only makes a very small difference with respect to the flow rate increase by the addition of nitrogen.

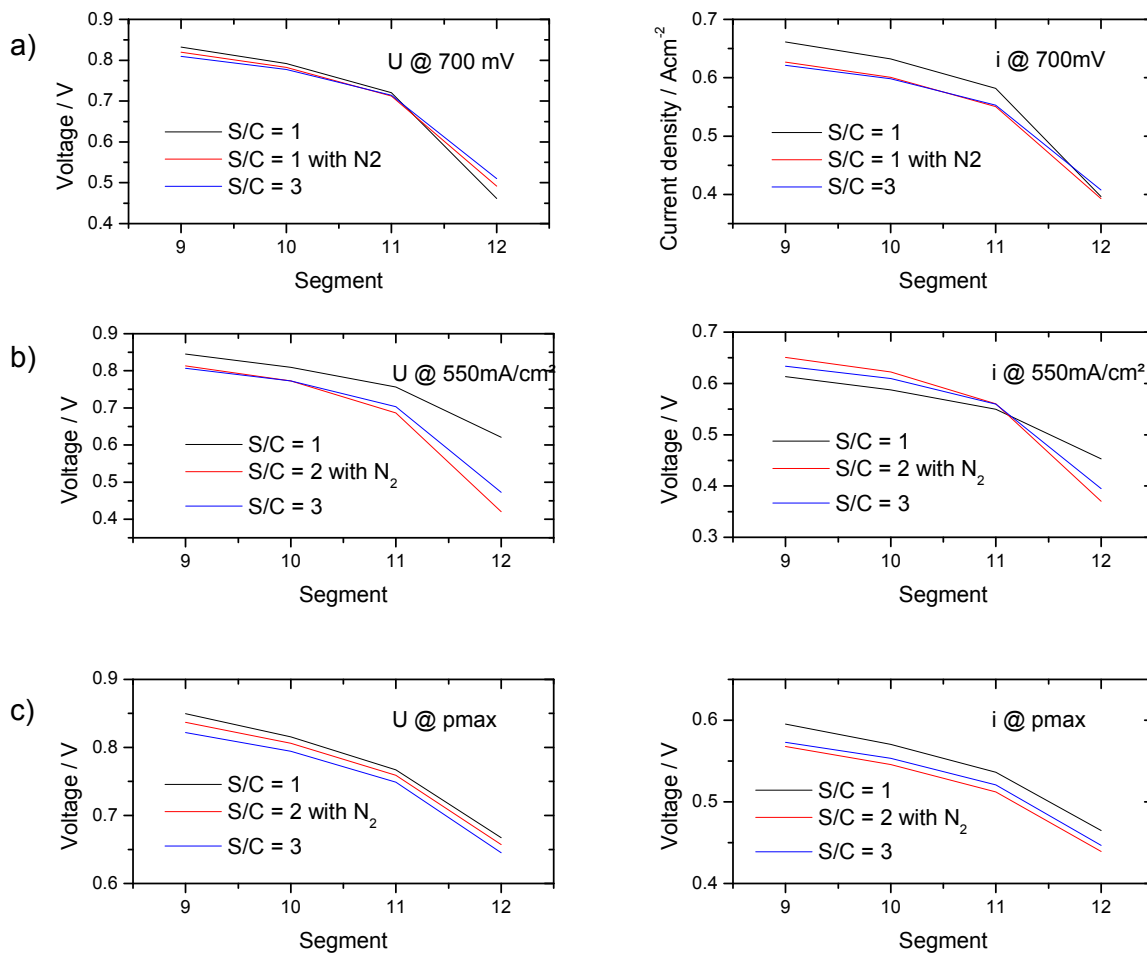


Figure 7-8: Comparison of simulated voltage (left) and current density (right) at a) global cell voltage of 700 mV, b) global current density of 550 mA/cm², c) maximum power density for S/C ratios of 1 and 3 (counter flow operation; anode: 0.085 l/min CH₄, 0.004 l/min N₂; cathode: 8 l/min air; T = 800 °C) as well as for S/C =1 diluted with nitrogen (counter flow operation; anode: 0.085 l/min CH₄, 0.174 l/min N₂; cathode: 8 l/min air; T = 800 °C).

A dilution of fuel with a non reactive gas like nitrogen or with a product gas leads to a more even distribution of voltage and current density within the cell if the total cell voltage is kept constant. This is different if the current and therefore the fuel utilisation is kept constant. In this case the current and voltage distribution is most homogeneous for the less diluted fuel as can be seen in Figure 7-8 b). The difference between the nitrogen dilution and the S/C = 3 condition is small, although the condition S/C = 3 shows a slightly more even distribution.

If the distribution is regarded at the maximum power density as in Figure 7-8 c) the lines for local current density and voltage are almost displaced in parallel. There is little difference in the gradient of voltage and current density along the cell between the three conditions but the least diluted fuel has the highest values for both.

These results indicate that more homogenous distribution within the cell resulting from a dilution of fuel depends on the control parameters used for the cell.

7.5 Influence flow rate on reforming

In chapter 7.2 the methane was reformed quickly right at the entrance of the cell. If a higher amount of methane is fed to the cell the reforming takes place along a greater length of the cell. To see the influence of the methane flow rate a measurement with a higher flow rate was done. Figure 7-9 shows the measured and simulated gas composition at OCV for an S/C ratio of 3 for a flow rate that is three times as high as in Figure 7-6. The nitrogen content was with 5 % a little higher in this case. The air flow rate is the same.

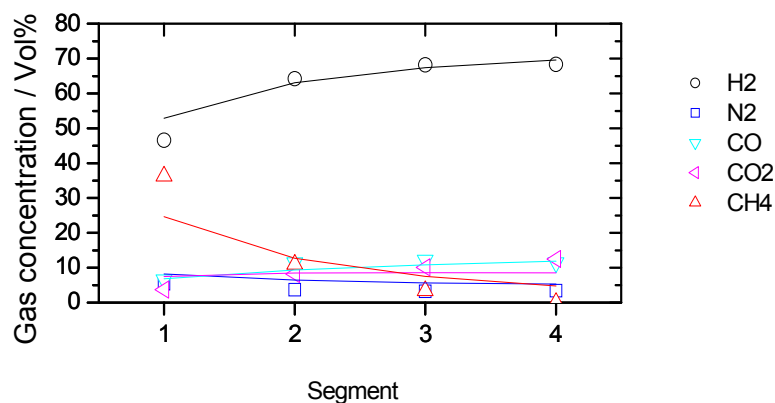


Figure 7-9: Measured and simulated gas composition along the flow path at OCV for S/C = 3. Water is not included in the diagrams (counter flow operation; anode: 0.281 l/min CH₄, 0.059 l/min N₂, 0.843 l/min steam; cathode: 8 l/min air; T = 800 °C).

In this case the reforming process is overestimated in the model as the experiment shows higher methane content for the first segment than the simulation. For the following segments the simulation and the experiments match very well. As expected the reforming process with higher flow rates does not take place only right at the entrance of the cell but also further along the cell.

7.6 Influence of nickel contact net on reforming reaction

As nickel is a catalyst for the reforming reaction it is to be expected that reforming takes place at the nickel contact mesh as well as at the anode of the cell. For some of the experimental measurements a Crofer 22 APU net was used as contact mesh on the anode side instead of a nickel mesh. A difference in the reforming of methane along the cell could be observed for the different contacts. Figure 7-10 shows the gas composition at OCV along the fuel path with a nickel mesh (left) and Crofer 22 APU mesh (right) as contact for an S/C ratio of 3. The flow rate is the same as in Figure 7-9.

At the first segment the measurement of the gas composition with a nickel contact shows a content of methane of about 36% while for the Crofer 22 APU contact a methane content of 63% was measured. The gas composition at the Crofer 22 APU net reaches the same fraction of CH₄ at segment 4 (after 4.9 cm) which a nickel net reaches at segment 2 (after 2.1 cm). The distance is more than twice as long.

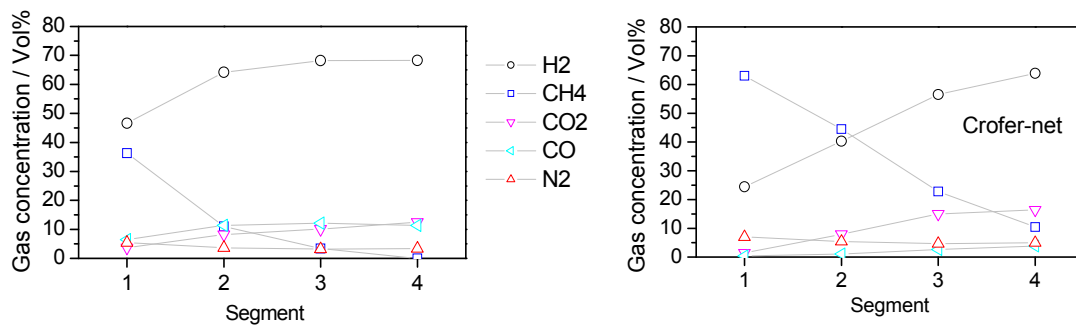


Figure 7-10: Gas composition along the flow path with nickel contact mesh and Crofer 22 APU contact mesh at OCV for S/C = 3. Water is not included in the diagrams (counter flow operation; anode: 0.281 l/min CH₄, 0.059 l/min N₂, 0.843 l/min steam; cathode: 8 l/min air; T = 800 °C).

If one aims at having a more even distribution of the reforming reaction along the cell a non-catalytic contact mesh would be an option. Still, the Crofer 22 APU net led to a rapid degradation of cell performance because it was quickly oxidised during operation which makes it unserviceable for the purpose.

8 Flow rate and temperature variations

The flow rate as well as temperature has a significant impact on the distribution of voltage, current density and gas composition in the cell. Measurements with H₂/N₂ = 50/50 and 3 % H₂O as shown in Table 8-1 were done at 800°C, 750°C und 700°C. Four different anode flow rates were used resulting in 12 measuring conditions. The measurements were done with the cassette design setup and cells of type B. Current-voltage curves were taken and the gas composition along the flow path for different loads was measured using the gas chromatograph. On the cathode the cells were supplied with 3 l/min of air for all conditions and the cells were operated in co-flow. I-V curves were taken galvanostatically at a rate of 70 mA/s. The model used in chapter 4 to 7 was not calibrated for this kind of cell, which is why no comparisons to simulations are done in this chapter.

H ₂ [%]	N ₂ [%]	H ₂ O [%]	Flow rate [l/min]
48.5	48.5	3	1.44
48.5	48.5	3	0.72
48.5	48.5	3	0.36
48.5	48.5	3	0.22

Table 8-1: Measuring conditions for flow rate variations.

8.1 Flow rate variations

Figure 8-1 shows the local i-V curves of segment 9 to 12 for the measuring conditions from Table 8-1 at 800°C. The anode is fed with 50/50 mixture of hydrogen and nitrogen which is humidified with 3 % of water. The four diagrams show the i-V curves for the four different flow rates. The local segment voltage is plotted versus the local segment current. Segment 9 is located at the entrance of the fuel gas; segment 12 is closest to the exit of the gases. The highest flow rate of 1.44 l/min is shown in Figure 8-1 a), in b) the second highest flow rate of 0.72 l/min is shown. Figure 8-1 c) shows the i-V curves for a flow rate of 0.36 l/min and in Figure 8-1 d) curves for the smallest flow rate of 0.22 l/min are shown.

There is little difference between the two highest flow rates which are shown in Figure 8-1 a) and Figure 8-1 b). All segments show a slightly lower current density for the lower flow rate but there is little difference between the characteristic curves of the different segments along the flow path. If the flow rate is reduced further, the characteristic curves of the segments start to fan out. The farther a segment is located from the entrance of the fuel gases the

smaller is the current density at which the local voltage drops. In Figure 8-1 c) the i-V curve of the last segment (segment 12) drops strongly at a current density of slightly above 0.3 A/cm² and the current density starts to decrease while voltage is decreasing further. In the range of this bent in the i-V curve a strong hysteresis can also be observed between the characteristic curve in which the load is increased and the curve for which the load is decreased. The other segments do not show this hysteresis. For the smallest flow rate the hysteresis appears at the last two segments (segment 11 and 12) as is shown in Figure 8-1 d).

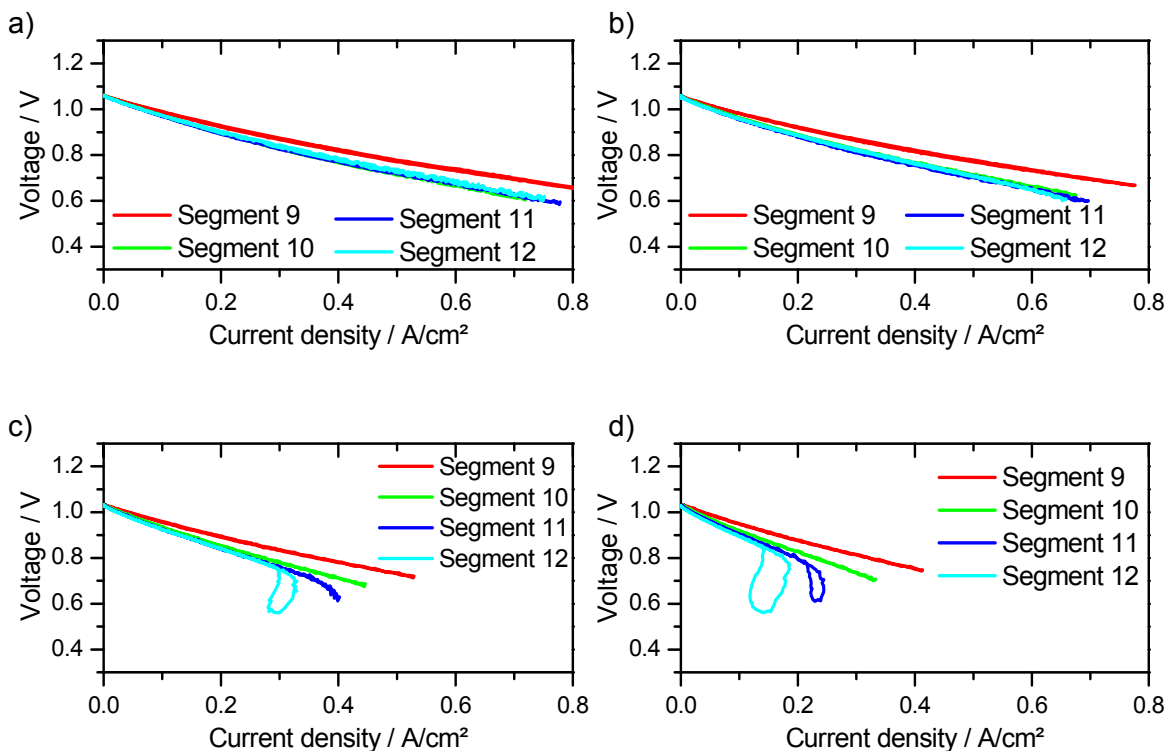


Figure 8-1: Local current-voltage curves of segments 9 to 12; T = 800°C, a) anode: 1.44 l/min, b) anode: 0.72 l/min, c) anode: 0.36 l/min, d) anode: 0.22 l/min; cathode 3 l/min.

8.2 Temperature variations

The conditions from Table 8-1 were measured at temperatures of 800°C, 750°C and 700°C. Figure 8-2 shows the local i-V curves for segments 5 to 8 for different temperatures and different flow rates. The upper row shows the i-V curves for the greatest flow rate the bottom row the curves for the smallest flow rate. Next to each other are the i-V curves with the same flow rate but different temperatures.

The lower the temperature the higher is the negative slope of the curves. The turning of the i-V curve of segment 8 which was already described earlier appears for a flow rate of

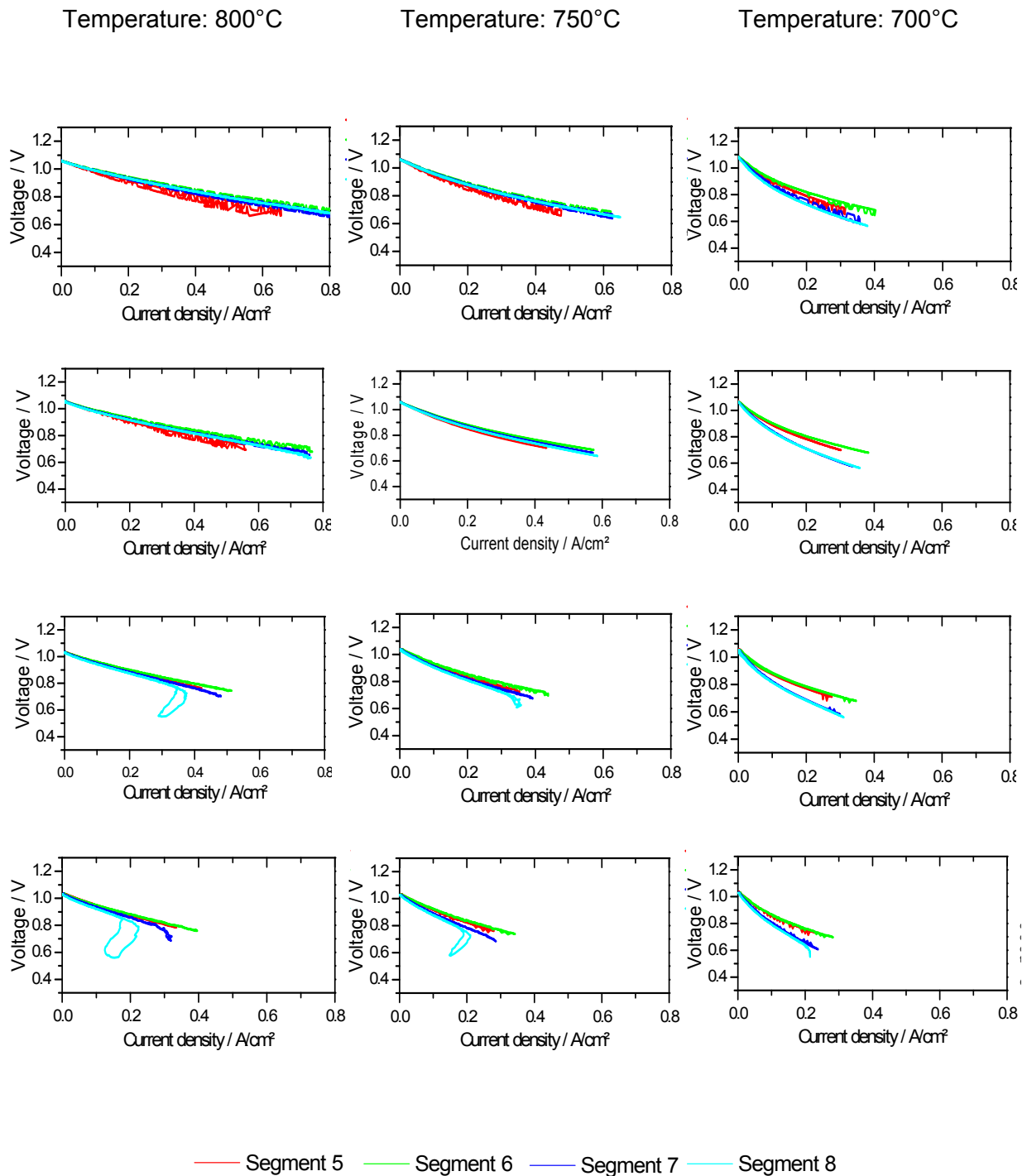


Figure 8-2: Local current-voltage curves for the segments of segments 5 to 8 for 4 different flow rates from Table 8-1 and at 800°C, 750°C and 700°C. Top row: highest flow rate, bottom row: lowest flow rate.

0.36 l/min at 800°C and at 750° but not at 700°C. For the smallest flow rate it appears at all temperatures. The turning point appears for each flow rate at similar current densities but different voltages.

When the highest current density which the individual segments reach is regarded it can be seen that the variation in the current density of the segments within the cell becomes smaller as the temperature decreases. The difference in current density between the segments at the entrance and at the exit of the fuel gases also decreases. This can be understood when the gas composition along the cell is regarded which is shown in the next chapter.

8.3 Gas composition

For all conditions from Table 8-1 measurements of the gas composition along the cell were done with the gas chromatograph. The gas composition was determined at OCV, at 850 mV and at 700 mV total cell voltage. OCV measurements were done to detect possible leakages, measurements under load to study the fuel depletion along the flow path.

Figure 8-3 shows the results of these measurements. The four diagrams correspond to the four gas flow rates from Table 8-1. The measured hydrogen concentrations for one row of segments (segments 5 to 8) are shown in red for OCV, in blue for 850 mV and in green for 700 mV total cell voltage. For each segment three pillars can be seen that correspond to the three different temperatures for which measurements were done.

At OCV the concentrations of hydrogen remain more or less constant along the cell. An exception is the smallest flow rate where a slight decrease of hydrogen can be observed even at OCV. This is assumed to be due to imperfect sealing and consequently a small leakage of air to the anode.

Under load the hydrogen concentration decreases along the flow path. The smaller the cell voltage the greater is this decrease. At the entrance of the fuel (segment 5) the difference between OCV and load is small, while at segment 8, which is located at the fuel exit, the difference is greatest. By comparing the four diagrams with each other one can see that the decrease of the hydrogen concentration is smaller the higher the flow rate is. This corresponds to the smaller fuel utilisation.

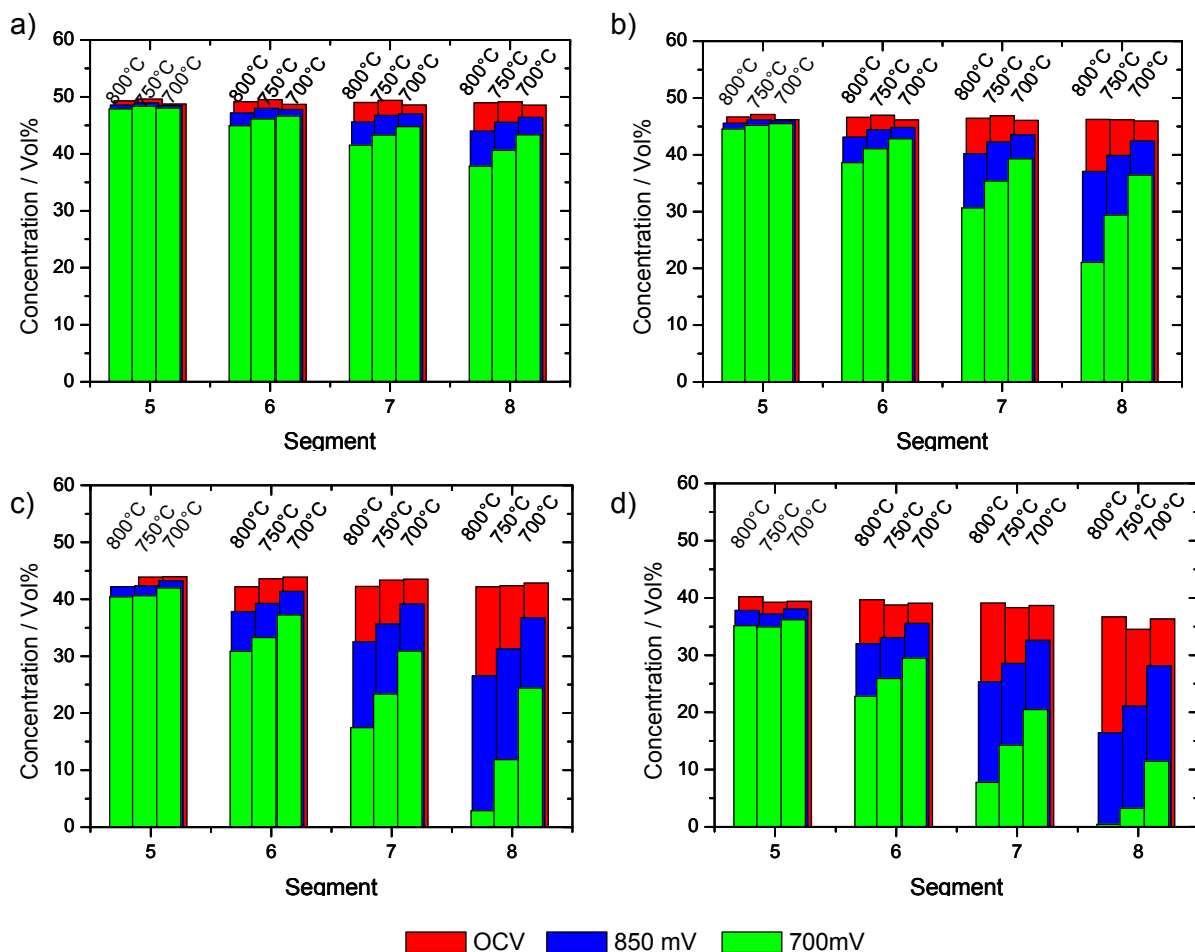


Figure 8-3: Hydrogen content along the flow path at segments 5 to 8 (middle row) at OCV, 850 mV and 700 mV for temperatures of 800°C, 750°C and 700°C. a) anode: 1.44 l/min, b) anode: 0.72 l/min, c) anode: 0.36 l/min, d) anode: 0.22 l/min; cathode 3 l/min.

At high temperatures the hydrogen concentration along the cell decreases faster than at lower temperatures. For low temperatures the distribution is more homogeneous. Since the power of the cell decreases with lower temperatures less fuel is consumed. This is then still available at the last segment. It can be seen that at a flow rate of 0.36 l/min and a temperature of 800°C and a total cell voltage of 700 mV the fuel is almost entirely consumed at the end of the cell. The amount of hydrogen measured was below 3 %. For the even smaller flow rate of 0.22 l/min the hydrogen content fell to below 1 %.

8.4 Influence of cell edge

It is to be expected that the distribution of gas within the flowfield is not perfectly homogeneous but that the gas channels located at the sides of the flowfield are not as well

supplied with fuel as the channels in the middle. To see whether there are differences between the rows of segments which are located at the side of the cell and in the middle the i-V curves of segments 1 to 4 as representing a middle row and segments 4 to 8 as a side row are compared. In Figure 8-4 they are marked in red and blue, respectively.

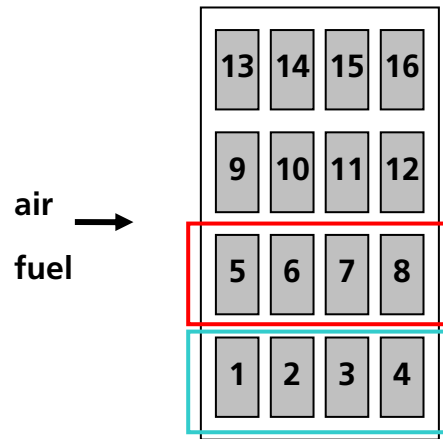


Figure 8-4: Position of middle (red) and side (blue) row.

Figure 8-5 and Figure 8-6 show on the left the current-voltage curves of a cell for the side row and on the right for the middle row for a gas flow of 0.36 l/min and 0.22 l/min from Table 8-1 respectively at a temperature of 800°C. As was already seen earlier the smaller the gas flow the more the curves of the segments along the row fan out.

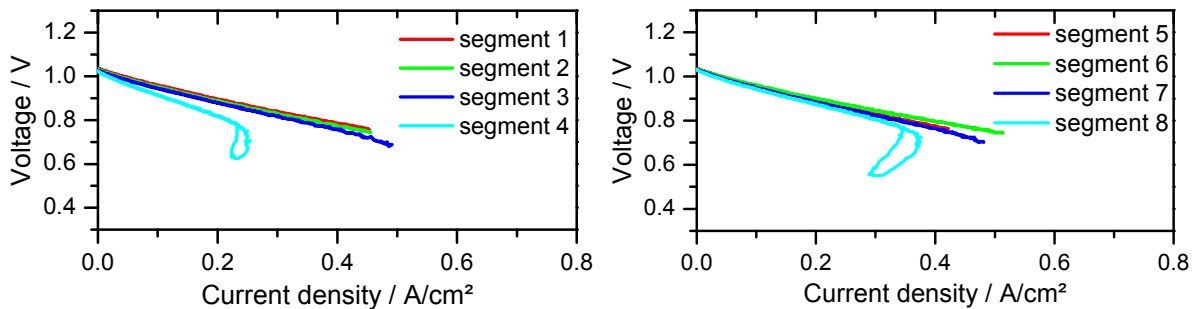


Figure 8-5: Current-voltage curves for the segments of a side row (left) and a middle row (right); T = 800°C, anode: 0.36 l/min, cathode 3 l/min.

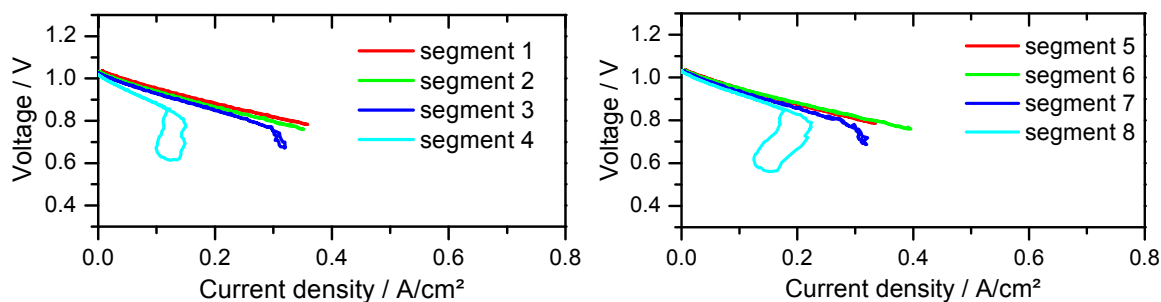


Figure 8-6: Current-voltage curves for the segments of a side row (left) and a middle row (right); T = 800°C, anode: 0.22 l/min, cathode 3 l/min.

The main difference between the middle and the side row is the current density at which the i-V curve of the last segment in the row i.e. segments 4 and 8 has its maximum and then decreases again. For the side row this current density is smaller than for the middle row for both flow rates. Table 8-2 shows the values for these turning points of the i-V curves for segment 4 and 8. For both flow rates the maximum current density for the last segment is about 1/3 smaller for the side row than it is for the middle. For higher gas flow rates the i-V curves of the last segments do not show the turn, therefore this comparison can not be made for them.

l/min	Segment 8	Segment 4	Difference side row – middle row	
	A/cm ²	A/cm ²	in A/cm ²	in %
0.36	0.376	0.255	0.121	32
0.22	0.224	0.150	0.074	33

Table 8-2: Values of the turning points of the i-V curves of segments 4 and 8 from Figure 8-5 and Figure 8-6.

At current densities below the turning point of the i-V curve of the last segment the voltages of the segments were compared at fixed current densities. For a gas flow of 0.36 l/min at the anode that current density was 200 mA/cm², for 0.22 l/min it was 100 mA/cm². There are no substantial differences to be seen. The differences found were below 8% and no tendencies were visible. No substantial differences were found for higher flow rates either.

It is probable that this difference between the side and the middle row is due to an unequal distribution of fuel and therefore a lower flow velocity at the sides of the flowfield or it is due to the influences of leakages at the side of the cell diluting the fuel. Figure 8-7 shows the hydrogen content of the fuel along the flow path for the side row made out of the segments 1

to 4. The difference between the side row (Figure 8-7) and the middle row (Figure 8-3) for a fuel flow rate of 0.36 l/min is small. At the flow rate of 0.22 l/min a stronger difference can be observed. Here the hydrogen content declines even at OCV indicating a leakage of air towards the anode at the side of the cell. Under load the hydrogen content is lower, too.

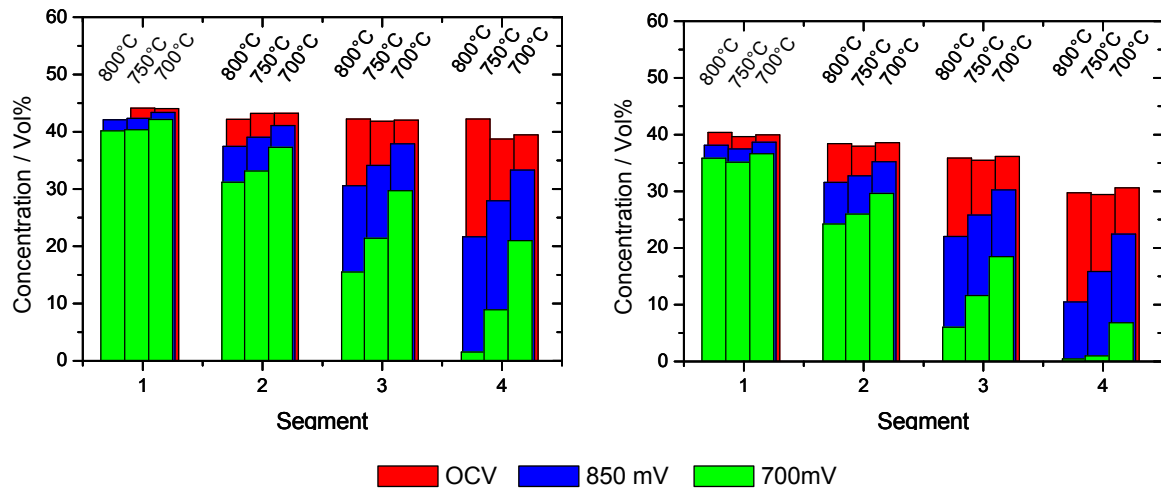


Figure 8-7: Hydrogen content along the cell for a side row at OCV, 850 mV and 700 mV for temperatures of 800°C, 750°C and 700°C. Left: anode: 0.36 l/min. Right: anode: 0.22 l/min.

For higher flow rates the difference in gas composition between the side and the middle row decreases.

Table 8-3 and Table 8-4 show the local voltage, current density and the fuel utilisation that was calculated from the electrical data after each segment for a side row (segments 1 to 4) and a middle row (segments 5 to 8) at 700 mV total cell voltage. For the calculation of the hydrogen utilisation it was assumed that each row of segments is supplied with $\frac{1}{4}$ of the total amount of fuel gas. This may lead to errors if the distribution of the gas is not homogeneous. The fuel utilisation of segment 8 in Table 8-4 is greater 100 % and in Table 8-3 the fuel utilisation for the middle row is greater than for the side row, too. This can easily be explained by the middle row (segments 5 to 8) receiving a greater amount of fuel than the assumed $\frac{1}{4}$ of the total amount of fuel gas. The middle row receives more fuel while the side row (segment 1 to 4) receives less, leading to the difference in the polarisation curves of the last segments that was seen in Figure 8-5 and Figure 8-6.

	Seg 1	Seg 2	Seg 3	Seg 4	Seg 5	Seg 6	Seg 7	Seg 8
Voltage [V]	0.766	0.751	0.714	0.607	0.776	0.751	0.723	0.670
Current density [A/cm ²]	0.410	0.386	0.456	0.186	0.362	0.471	0.439	0.345
Fuel utilisation after segment	24.7	47.9	75.3	86.5	21.8	50.1	76.5	97.3

Table 8-3: Local voltage, current density and fuel utilisation at segments 1 to 8 at 700 mV total cell voltage. T = 800°C, anode: 0.36 l/min, cathode 3 l/min.

	Seg 1	Seg 2	Seg 3	Seg 4	Seg 5	Seg 6	Seg 7	Seg 8
Voltage [V]	0.775	0.758	0.692	0.609	0.784	0.757	0.722	0.625
Current density [A/cm ²]	0.322	0.293	0.275	0.085	0.289	0.360	0.309	0.135
Fuel utilisation after segment	32.3	61.7	89.3	97.8	28.9	65.1	96.1	109.6

Table 8-4: Local voltage, current density and fuel utilisation at segments 1 to 8 at 700 mV total cell voltage. T = 800°C, anode: 0.22 l/min, cathode 3 l/min.

8.5 Influence of LSCF cathode

Solid oxide fuel cells with an LSCF cathode show a higher performance than those with an LSM cathode. The conditions from Table 8-1 were measured on cells with LSCF cathode as well as with LSM cathodes. A comparison between the segmented current-voltage curves of the two different cathodes can be seen in Figure 8-8 where the i-V curves for the highest flow rate from Table 8-1 are shown and in Figure 8-9 where the curves of the lowest flow rate can be seen. In the left diagrams the local current-voltage curves for a cell with LSM cathode can be seen, while the right shows the local i-V-curves for a cell with LSCF cathode. In Figure 8-8 the segments along the flow path show a similar performance since the flow rate is high and fuel utilisation remains low. The cell with the LSCF cathode shows a higher performance. At a voltage of 0.8 V the LSM cathode reaches a current density of 0.4 A/cm² while the LSCF cathode reaches twice that value (0.8 A/cm²).

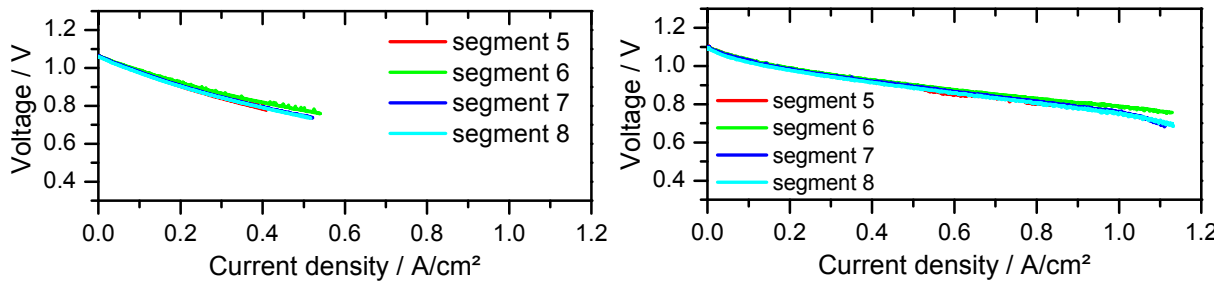


Figure 8-8: Current-voltage curves for segments 5 to 8 with LSM cathode (left) and LSCF cathode (right). T = 800°C, anode: 1.44 l/min, cathode 3 l/min.

Figure 8-9 shows the local current-voltage curves for segments 5 to 8 for a cell with LSM cathode on the left and with LSCF cathode on the right side for the lowest flow rate from Table 8-1. The fanning out of the curves of the segments which has already been described in previous chapters is stronger for the LSCF cathode than for LSM. The voltage drop of segment 8 after the current density starts to decrease while voltage continues to drop is much more pronounced for the LSCF cathode. The local current density at which the curve of segment 8 turns is the same for both cell types.

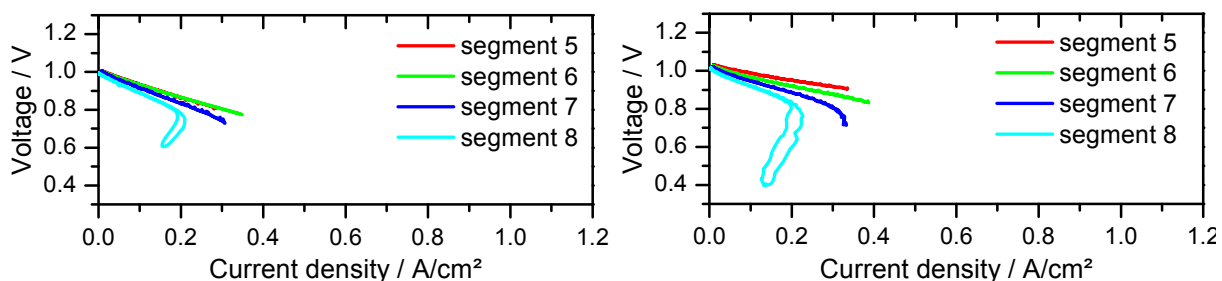


Figure 8-9: Current-voltage curves for segments 5 to 8 with LSM cathode (left) and LSCF cathode (right). T = 800°C, anode: 0.22 l/min, cathode 3 l/min.

Figure 8-10 shows the hydrogen content measured along the flow path for the LSM cathode in the left diagram and for the LSCF cathode on the right. The hydrogen content is shown in red for OCV, in blue for 850 mV and in green for 700 mV total cell voltage. For each segment three pillars can be seen that correspond to the three different temperatures for which measurements were done.

It can be seen that the fuel consumption along the flow path is greater for the LSCF cathode which is to be expected since the cell shows a higher performance. A higher cell

performance leads to a greater gradient in gas composition and therefore in voltage and current density distribution.

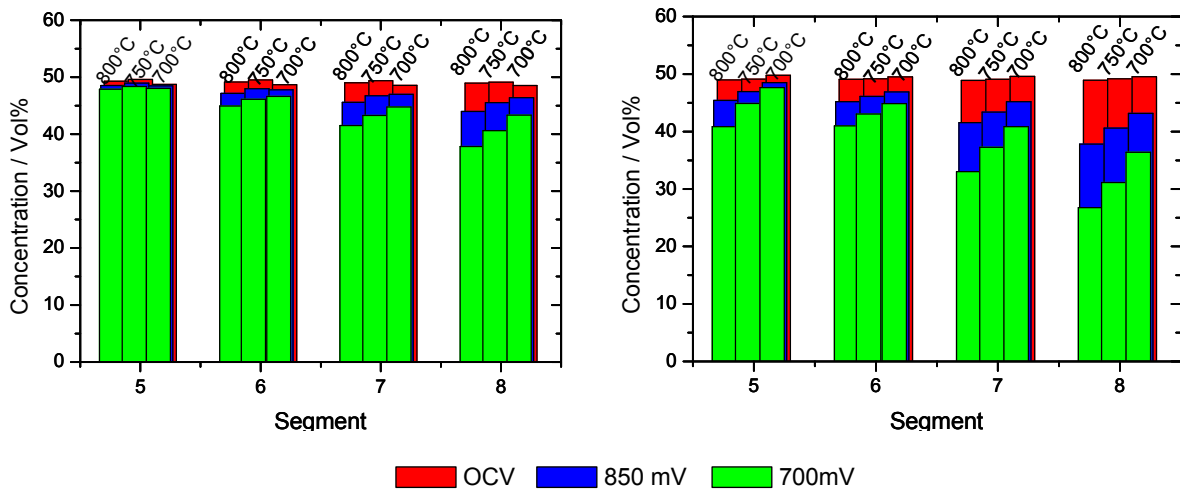


Figure 8-10: Hydrogen content along the flow path at segments 5 to 8 at OCV, 850 mV and 700 mV for temperatures of 800°C, 750°C and 700°C with LSM cathode (left) and LSCF cathode (right). T = 800°C, anode: 1.44 l/min, cathode 3 l/min.

8.6 Hysteresis

Figure 8-1 shows for the last segment and low flow rates a strong hysteresis between the polarisation curves for increasing and decreasing the load. This hysteresis appears at the point where the current density starts to decrease while the voltage continues to fall. It could be due to the depletion of fuel at the anode that was shown in chapter 8.3 and an increased influence of diffusion processes in the cell at the rather fast rate at which the polarisation curves were taken. It could also be due to temperature effects or the oxidation of nickel at the anode due to the low voltage and fuel content. The temperature effect can be excluded since the increase of cell temperature during the polarisation curve was for all segments smaller than 1°C although the temperature of the last segment increases less strongly once the i-V curve turns.

To see whether the hysteresis seen in Figure 8-1 for the two lower flow rates is related with the formation of nickel oxide at the anode, cells were polarised until the total cell voltage was 0.7 V and the last segment was well into the area where current density decreases while voltage decreases as well. The flow rate was 0.36 l/min and the temperature was 800°C. This condition was held during 45 minutes. Afterwards the load was taken away abruptly and the cell was flushed with nitrogen at the same time on both electrodes to avoid a reduction of nickel oxide at the cell. The cell was then cooled to room temperature and taken out of the

setup. Figure 8-11 b) shows the anode of the cell with the gas flow directions. The anode is partially oxidised as can be seen by its colour. The anode is usually of a grey colour but when the nickel contained in it is oxidised it turns green. The oxidation in Figure 8-11 b) appears mainly around the edge and more strongly at the entrance of the fuel gas than at the exit. This is probably due to leakages since there could not be observed any great difference in comparison with a cell that was cooled down while being flushed with nitrogen on both sides after having been kept at OCV for some time which is shown in Figure 8-11 a. There was no additional nickel oxide observed at the segments exposed to low voltage. Especially no nickel oxide was detected at the electrolyte interface at the last segments where according to chapter 5.5 the conditions in gas composition are most likely to lead to the formation of nickel oxide. This indicates to nickel oxide not being the reason for the hysteresis observed in the i-V curves of the last segment or that the time of exposure was not sufficiently long.

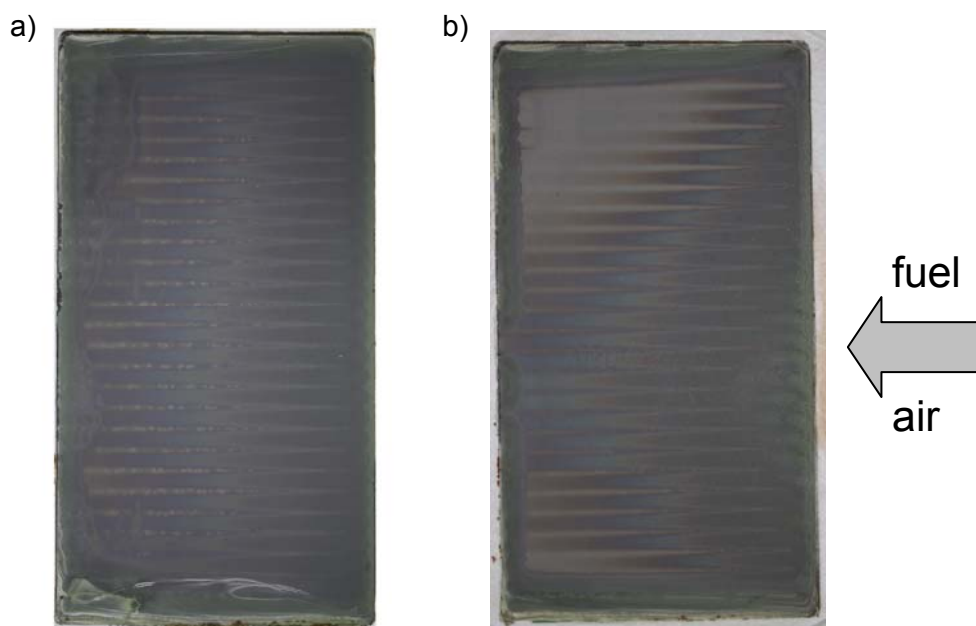


Figure 8-11: Anode after operation at OCV (a) and 700 mV total cell voltage(b), flushed with N₂ during cool down.

8.7 Electrolyte defects

It occurred for several cells that segments showed a poorer performance than the corresponding segments for other cells. One cell where segments 11, 14 and 15 showed a deviation of more than 18 % at 400 mA/cm² at an anode flow rate of 1.44 l/min was cooled

down while the cell was flushed with nitrogen on both electrodes after operation at 700 mV as described in chapter 8.6. Figure 8-12 shows the anode of the cell with the gas flow directions after the test. Marked in red are two areas in which a strong oxidation can be seen in the upper middle part. These areas correspond to segments 11, 14 and 15 that had shown lower power densities during operation than during measurements with other cells. The cell is also oxidised around the edge as are the cells shown in chapter 8.6.



Figure 8-12: Partially oxidised anode after operation at 700 mV total cell voltage. Strongly oxidised areas in the middle correspond to segments 11, 14 and 15.

After operation the cathode was removed in the areas where the anode was oxidised at the segments that showed poorer performance and for comparison at segments that showed neither stronger oxidation nor poorer performance. The surface of the electrolyte is shown in Figure 8-13 for two different magnifications. The images were taken with an optical microscope. The electrolyte above the non-oxidised areas which is shown on the right is smooth and only shows some light scratches from removing the cathode. On the left the electrolyte above the oxidised region can be seen. It shows an agglomeration of craters over a large region of several mm which could also be seen without the microscope.

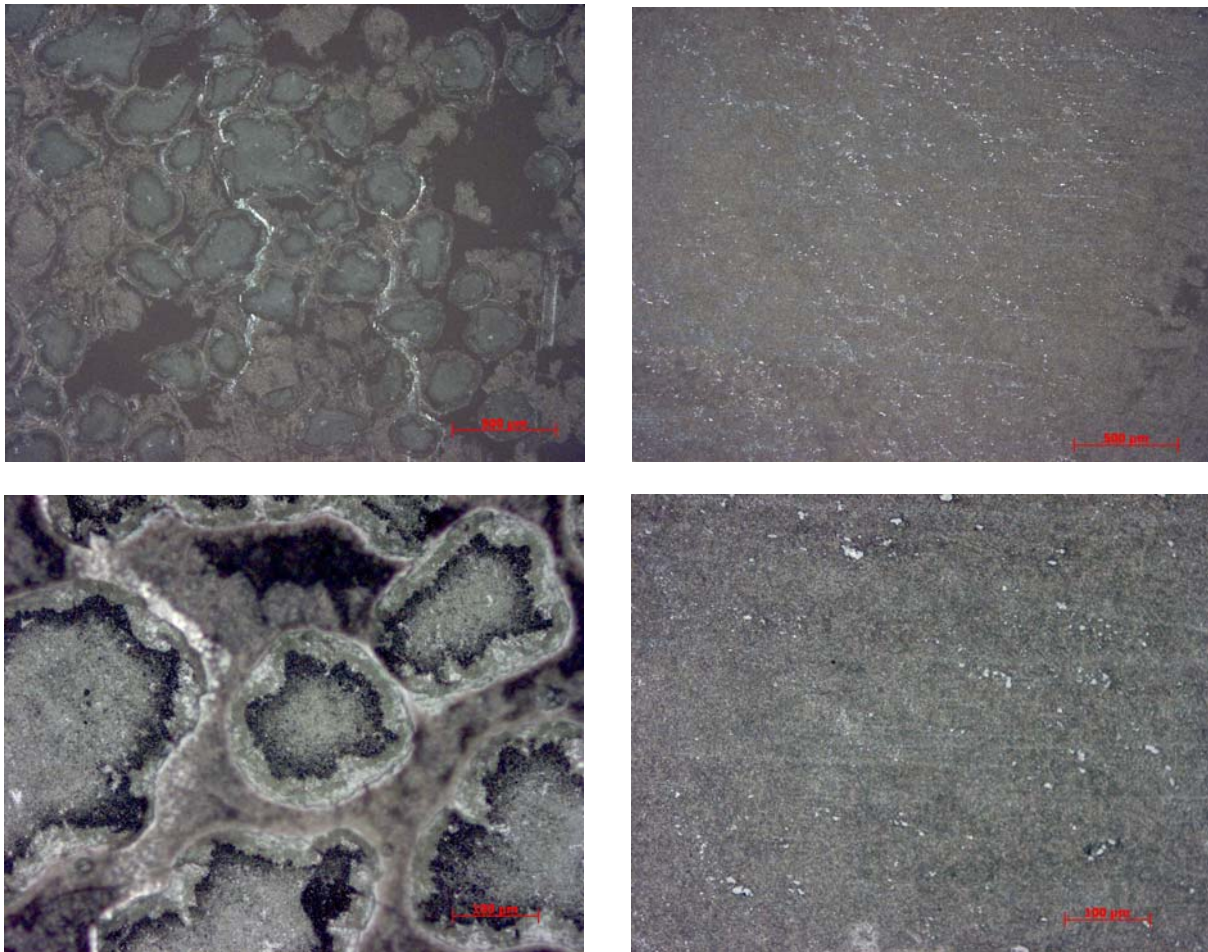


Figure 8-13: Surface of the electrolyte after removal of the cathode for a region with oxidation at the anode (left) and for non-oxidised region (right)

If a cross section of the electrolyte defect area is regarded under the optical microscope a structure change of the anode below the defect can be observed as in the left picture of Figure 8-14. The white spots are metallic nickel. Just below the electrolyte defect no nickel is visible. The picture on the right of Figure 8-14 shows the anode below a non-defective electrolyte for comparison.

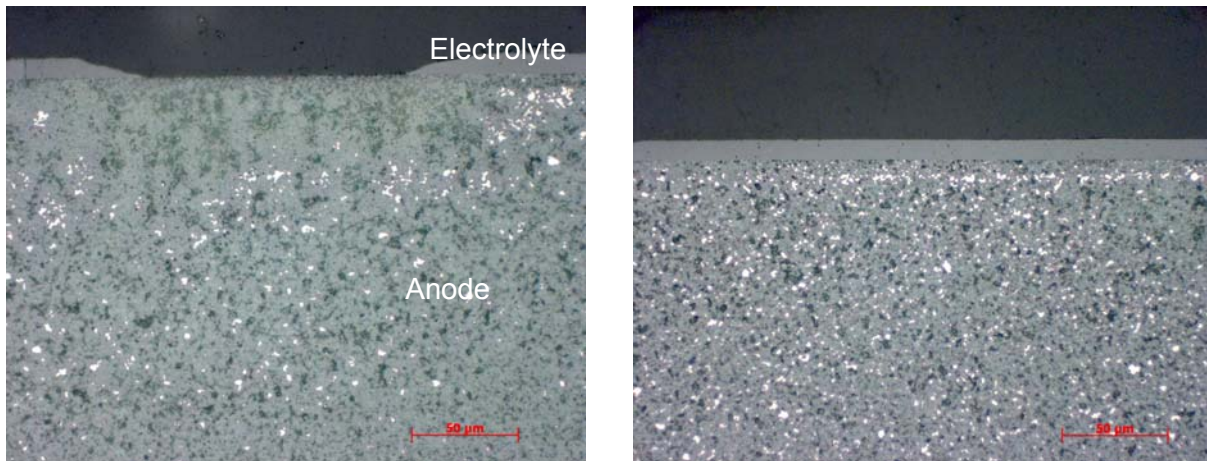


Figure 8-14: Cross section of cell with electrolyte defect (left) and without (right)

Figure 8-15 shows an EDX map of the electrolyte defect from Figure 8-14 and the anode underneath it. The electrolyte material zirconia oxide is presented in purple, nickel is green and nickel oxide is yellow. The greater part of the nickel is oxidised. Just below the electrolyte defect the ceramic matrix of the anode is also rather depleted of nickel.

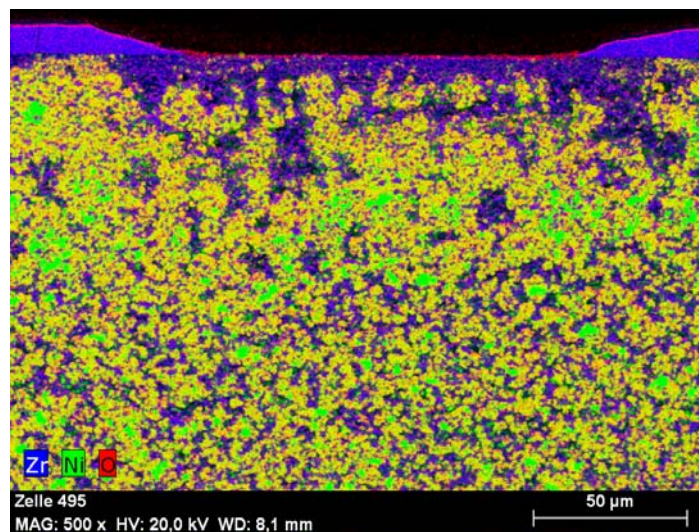


Figure 8-15: EDX Map of area below electrolyte defect showing zirconia oxide (purple), nickel (green) and nickel oxide (yellow).

A correlation between the poor local performance of the cell segments and local electrolyte defects was observed. The defects in the electrolyte led to a local performance loss and local nickel oxidation in the anode as well as a depletion of nickel just below the defect.

The measuring setup for the segmented cell offers the possibility to further study the effects of defects in the electrolyte, if for example cells with intentionally defective areas are measured. It might be possible to determine the critical size of defects for affecting local performance and the influence of local defects on the local and global degradation of the anode.

9 Cell behaviour under negative voltages

In a stack the cells are connected in series, the current being the same for all cells. The voltage varies according to differences in the characteristics of the individual cells. If one cell differs strongly from the others it is driven at a lower voltage than the others resulting in negative voltages in the worst case. It is to be expected that these negative voltages seriously damage the cell and lead to a further voltage loss and an increase in local temperature. At 800°C a voltage of below 0.679 V is expected to lead to the oxidation of the nickel in the anode. It can be found in literature that negative voltages lead to delamination and breaking of the electrodes and even to a decomposition of the electrolyte, which may be a matter of minutes only [54].

It has been shown in previous chapters that at high fuel utilisations the local i-V curves of the cells fan out and the local voltage drops at lower current densities close to the exit of the fuel gases than at the entrance. If the current density is further increased local voltages may even become negative at the exit of the fuel gas. At a further increase of current density the negative voltages proceed towards the fuel entrance. In the following part the damage to a cell because of local negative voltages is studied.

A type A cell was operated with 0.3 l/min H₂, 1.2 l/min N₂ and 0.015 l/min H₂O at the anode and 4 l/min air at the cathode. The cell was operated in counter-flow. A current was drawn until the last two segments of each row showed negative voltages. This load was held for 10 minutes. Figure 9-1 shows the voltages and current densities over time during the experiment. The situation is not quite the same as in a stack where one cell is forced to operate under negative voltages since in the following case the negative voltages are obtained by fuel starvation. Note the behaviour of the current density of segments 11 and 12. For both segments the current has a peak when the segment voltage reaches 0.6 V and another some 5 minutes later.

Before the experiment as well as afterwards an i-V curve was taken. After 10 minutes of negative voltage no great difference could be seen in the local characteristic curves. The experiment was repeated and the negative voltages kept constant for 30 minutes. Afterwards a difference in the i-V curves was visible. As shown in Figure 9-2 segments that had been exposed to negative voltages showed a drop in the characteristic curves at lower current densities. Especially the curve of segment 11 changed even though segment 12 was exposed to more negative voltages. For the segments that were not exposed to negative voltages the polarisation curves even show a slight improvement.

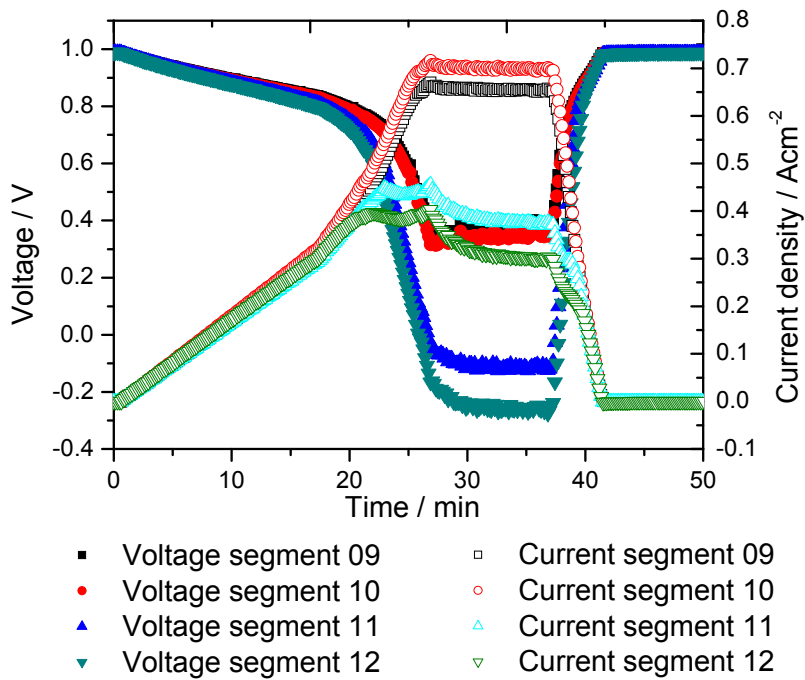


Figure 9-1: Voltage and current density during operation at negative voltages at segments close to the exit of the fuel. T = 800°C; anode: 0.3 l/min H₂, 1.2 l/min N₂, 0.015 l/min H₂O; cathode: 4 l/min air.

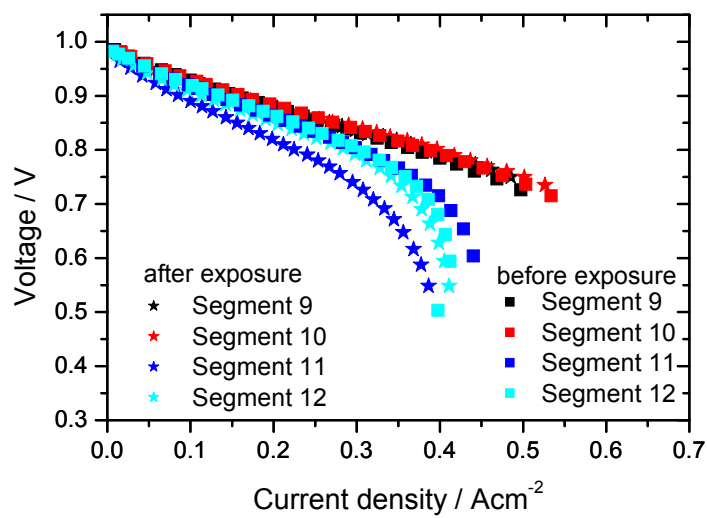


Figure 9-2: Local characteristic curves before and after exposure to negative voltages.

Before and after the exposure to negative voltages impedance spectra were taken at one cell for the different segments. These spectra are shown in Figure 9-4. The first measurement was taken before the exposure to negative voltages, the second after the short exposure and number 3 after the longer exposure. The impedance diagrams of segments 9 and 10 which were not exposed to negative voltages do not show a great difference in the Bode plot. The arcs in the Nyquist diagrams of these two segments show a decreasing arch from the first to the last measurement. For segments 11 and 12 which were exposed to negative voltages changes can be seen between the three measurements. Segment 11 showed higher impedances for low frequencies than the other segments from the beginning and the differences observed in the impedance spectra are greatest for this segment. The change visible for segments 11 and 12 shows a similar tendency although the change is far greater for segment 11 that already showed higher impedances at low frequencies. The arch in the Nyquist diagram also gets smaller for the second measurement after a short exposure to negative voltages. After the long exposure the arch at lower real parts of the impedance has increased for both segments and the whole spectra has moved towards higher real parts that is higher resistances. The increased resistance can also be seen in the corresponding Bode plot especially for segment 11.

For further interpretation of the obtained impedance spectra an equivalent circuit model was used as shown in Figure 9-3 consisting of an inductivity (1), an ohmic resistance (2) and three RC components, for anode (3 and 4), cathode (5 and 6) and gas concentration (7 and 8).

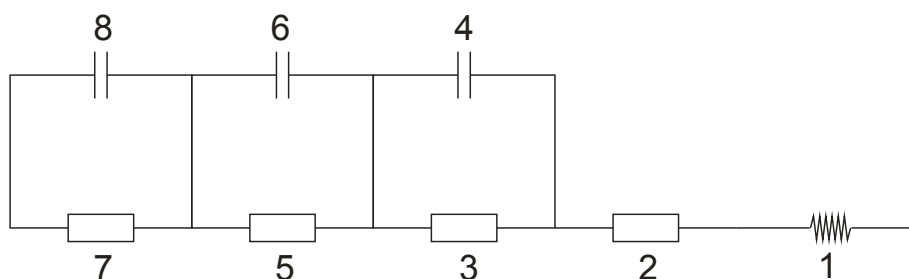


Figure 9-3: Equivalent circuit model for impedance analysis

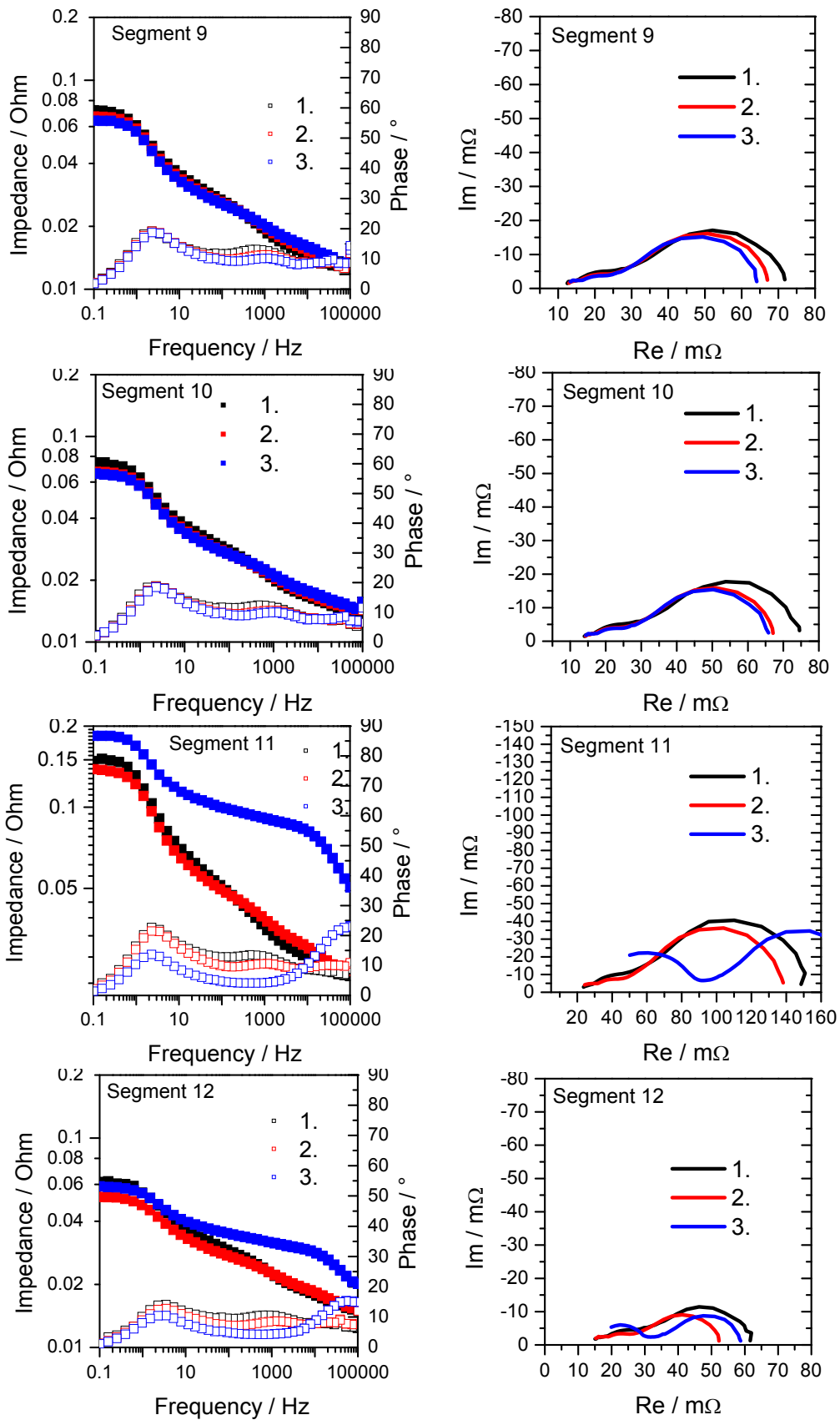


Figure 9-4: Impedance spectra of segments 9 to 12 before (1) and after exposure (2: 10 min., 3: 30 min.) to negative voltages.

The results of the fitting of the equivalent circuit to the experimental spectra are shown in Figure 9-5 where each diagram shows the resistances for all three measurements before (1) and after (2 and 3) exposure to negative voltages for one segment. It can be seen that segments 9 and 10 show a decreasing total resistance from measurement 1 to 3. This decrease is according to Figure 9-5 mainly due to the decrease of gas concentration resistance and cathode resistance. Anode resistance and ohmic resistance hardly change. For segments 11 and 12 which were exposed to negative voltages the total resistance decreases between measurements 1 and 2, that is after a short exposure to negative voltages. Segment 11 shows greater resistances than all of the other segments. After the long exposure to negative voltages the total resistance of segments 11 and 12 has increased again (measurement 3). All resistances except gas concentration contribute to this increase. For segment 11 anodic resistance shows the greatest increase while for segment 12 the greatest increase is observed for ohmic resistance.

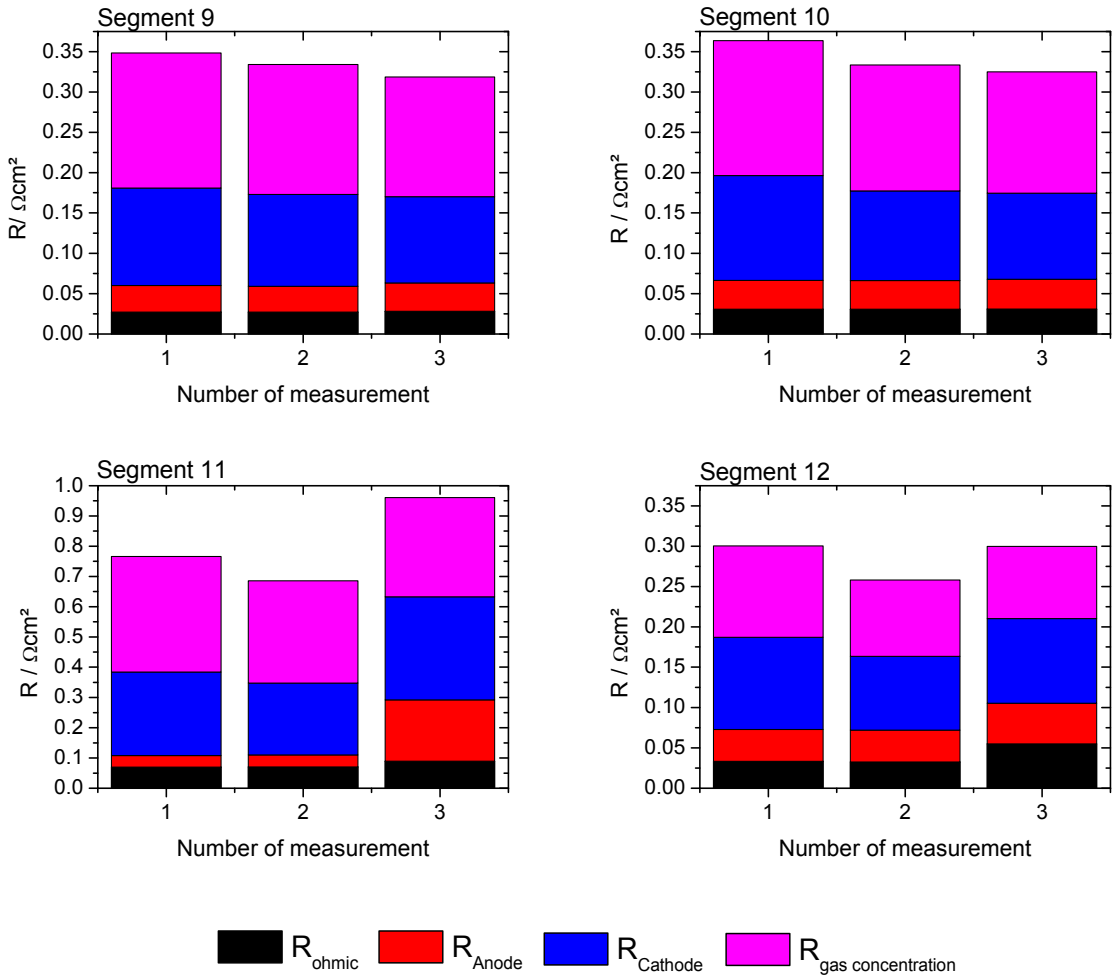


Figure 9-5: Resistances before (1) and after (2, 3) exposure to negative voltages

These measurements show that negative voltages are damaging a cell especially when the cell or segment already shows an increased resistance as did segment 11. A short exposure did not damage the cell and even increased the performance slightly as can be seen by the reduction of the arches in the Nyquist plot for all segments after the second measurement.

In a non-segmented cell it is not to be expected that the cell is operated locally at negative voltages due to the more equal voltage distribution within a non-segmented cell as was explained in chapter 5.6.4. The measurements show nevertheless that short exposures to negative voltages do not damage the cell and that for longer exposures a locally increased cell resistance can lead to a stronger local degradation under these extreme conditions than what would otherwise be seen.

After the second exposure to negative voltages the cell was cooled down and taken out of the setup. Figure 9-6 shows SEM micrographs of fractures of segments 9 and 11 of the cell. The micrograph on the left shows segment 9 that was not exposed to negative voltages while the one on the right shows segment 11 that was and that showed a major decrease in performance. A delamination of the anode can be seen on the right hand picture that didn't occur to the other segment on the left. No cracks or other changes within the anode were observed.

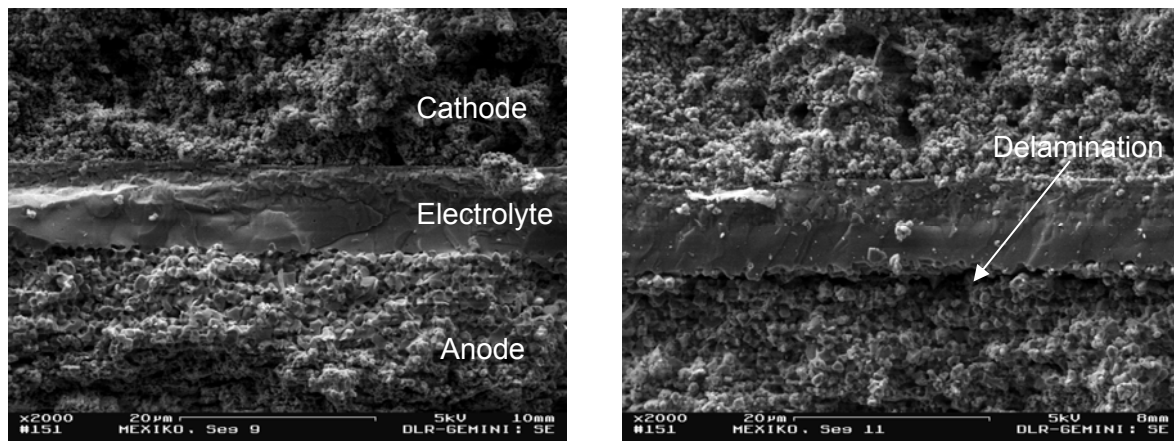


Figure 9-6: SEM micrographs. Left: segment after operation under positive voltage. Right: segment after exposure to negative voltages.

10 Obtaining a more even distribution

It was shown in chapter 8 that an increase in cell performance for example through a rise in temperature or an LSCF cathode leads to increasing gradients of performance within the cell. This is because segments at the fuel entrance perform better and therefore consume more fuel which is then not available at the segments towards the end of the flow path. It was also shown in chapter 9 that extreme local conditions can damage the cell and have to be avoided.

The easiest way of avoiding local variations is a low fuel utilisation. If nevertheless a very high fuel utilisation is required a possibility to achieve a more homogeneous distribution within the cell would be to improve the fuel supply of the end part of the cell. This might be done by reducing fuel consumption at the entrance so that more fuel is then still available at the end part of the cell. A possibility would be to introduce a fuel distributor (e.g. a mesh, net or porous paste etc.) between the gas channels and the cell with smaller porosity at the entrance and higher porosity at the end of the cell. A scheme of such a distributor can be seen in Figure 10-1.

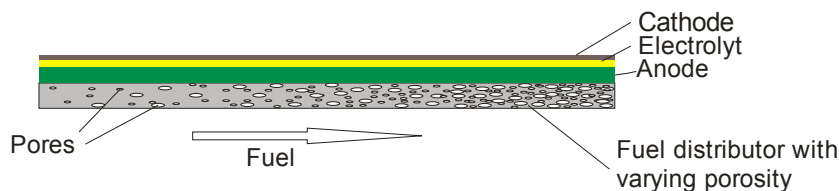


Figure 10-1: Scheme of a fuel cell with fuel distributor with varying porosity.

A varying porosity and pore size of the anode substrate or a varying content of catalyst and catalyst size within the anode or cathode might have the same effect.

Flow field design might also be examined to obtain a more even distribution. The flow velocity might perhaps be modified along the cell by introducing smaller gas channels at the entrance that widen towards the end. A higher flow velocity at the entrance would reduce the time the fuel remains at the entrance segments. If that time is short enough the consumption of fuel at the cell entrance could be reduced. The flow field should also be improved to have a more similar performance of side and middle rows [55].

11 Summary

To meet the challenge of a sustainable energy supply new methods of energy conversion are necessary. Fuel cells offer high electrical efficiencies and the solid oxide fuel cell is particularly interesting because not only hydrogen can be used as fuel but also fuels containing hydrocarbons like natural gas, biogas or diesel and kerosene reformates can be used without a prereformer. These fuels are easily accessible. For the commercial use of fuel cells a high electrical efficiency and low degradation are necessary. High efficiency and high fuel utilisation lead to strong gradients in gas composition along the cell which can in turn lead to lower power densities and increased local degradation.

To better understand the local distribution and its effects a combined experimental and modelling study was done. Segmented planar anode-supported cells were characterised in a setup with 4 x 4 segments and a detailed two-dimensional model representing this setup was developed and validated.

Since hydrogen is the fuel presenting the least problems the model was at first calibrated for hydrogen/nitrogen mixtures with various water contents. A very good agreement between the model and the experiments was achieved. The model was then used to study the influence of several cell parameters. A variation of the gas channels did not show a significant influence. A variation of the electrode thickness showed an increase of power density for thinner electrodes. The effect of the segmentation in comparison to a non-segmented cell is a more even distribution of voltage and a greater variance of current density in the non-segmented cell while the gas composition along the flow path is similar for segmented and unsegmented cells.

The second step was to calibrate the model also for CO as fuel to be able to simulate not only H₂/N₂ mixtures but also reformat gases. Here the influence of very high fuel dilution could also be observed that led to the oxidation of nickel at the anode and a plateau-like behaviour in the current-voltages curves.

As a third step the model was validated for more complex methane/steam mixtures and internal reforming. Here water-gas shift, reforming reactions and cell reactions take place at the anode and are coupled to diffusive and convective transport processes. The agreement obtained between model and experiments is good. The methane is reformed at the entrance to the cell leading to an additional variation in gas phase species along the flow path. A great part of the reforming process takes place at the nickel contact mesh and not at the anode of the cell which could be seen in comparison to experiments with a non-catalytic contact mesh. It was also shown that a dilution of the fuel with water or nitrogen and consequent increase in

flow rate can lead to a more homogenous distribution within the cell depending on the control parameters used for the cell.

Furthermore a variation of flow rate and temperature was performed and the gas composition along the cell was measured. The higher the load the stronger is the decrease of the fuel content along the cell. At lower temperatures this decrease is smaller. The rows of segments located at the side of the cell showed a different performance than those in the middle, especially the last segment, due to an unequal distribution of the fuel into the flow field. This influence increases with lower flow rates. A correlation between electrolyte defects, poor local performance and increased nickel oxidation at the anode was observed. The comparison of cells with LSM and LSCF cathodes showed that those with LSCF as cathode were prone to stronger gradients within the cell.

When operating the cell at low voltages some segments may show negative voltages while the total cell voltage remains positive. Locally negative voltages were found to cause damage only at long exposures (30 min). Segments that already showed high cell resistances suffered stronger degradation than segments with low initial resistances under these extreme conditions.

The validated model can be used further to determine optimal operating parameters for performance under given framework requirements and also what conditions have to be avoided. The model does not help to assess degradation since degradation phenomena are not yet included but critical operating parameters can be estimated. Further measurements with low fuel content and low voltages to investigate the chemical and electrochemical formation of nickel oxide might yield interesting results and long-term measurements to understand the influence of local critical parameters or electrolyte defects on cell degradation should be performed. The gas distribution into the flow field should also be examined to reduce differences between the edge and middle rows.

12 References

1. Larminie, J. and Dicks, A., *Fuel cell systems explained* 2003, Chichester, West Sussex: J. Wiley.
2. Hamann, C.H. and Vielstich, W., *Elektrochemie*. 3. vollständig überarbeitete Auflage ed. 1998, Weinheim: Wiley-VCH.
3. Srinivasan, S., *Fuel cells: From fundamentals to applications*. 2006: Springer Verlag.
4. Noren, D.A. and Hoffman, M.A., *Clarifying the Butler-Volmer equation and related approximations for calculating activation losses in solid oxide fuel cell models*. Journal of Power Sources, 2005. **152**: p. 175-181.
5. Boer, B.d., *SOFC Anode: Hydrogen oxidation at porous nickel and nickel/yttria-stabilized zirconia cermet electrodes*. Doctoral thesis, 1998, University of Twente.
6. Singhal, S.C. and Kendall, K., *High Temperature Solid Oxide Fuel Cells, Fundamentals, Design and Applications*. 2006, Oxford: Elsevier.
7. Duangmanee, T., Wannakitti, S., Suwanwarangkul, R. and Charojrochkul, S., *Electrical Property of Thick Film Electrolyte for Solid Oxide Fuel Cell*. Journal of Metals, Materials and Minerals, 2008. **18(2)**: p. 7-11.
8. Müller, A., *Mehrschicht-Anode für die Hochtemperatur-Brennstoffzelle (SOFC)*. Doctoral thesis, 2004, Karlsruhe.
9. Stehlík, K.B., *Zur Degradation oxidkeramischer Brennstoffzellen*, Doctoral thesis, 2009, Technische Universität München: München.
10. Mai, A., *Katalytische und elektrochemische Eigenschaften von eisen- und kobalthaltigen Perowskiten als Kathoden für die oxidkeramische Brennstoffzelle (SOFC)*. Schriften des Forschungszentrums Jülich. Reihe Energietechnik/Energy Technology 31. 2004 Forschungszentrum Jülich, Zentralbibliothek, Verlag.
11. Tanaka, Y. and Kato, T., *Reforming of methane, ethylene, and desulfurized kerosene over Ni-8YSZ catalyst*. Applied Catalysis A: General, 2008. **348(2)**: p. 229-235.
12. Leinfelder, R., *Reaktionskinetische Untersuchungen zur Methan-Dampf-Reformierung und Shift-Reaktion an Anoden oxidkeramischer Brennstoffzellen*. Doctoral thesis, 2004, Friedrich-Alexander-Universität: Erlangen-Nürnberg.
13. Neumann, D. and Vesper, G., *Catalytic partial oxidation of methane in a high-temperature reverse-flow reactor*. AIChE Journal, 2005. **51(1)**: p. 210-223.
14. Cheekatamarla, P.K. and Finnerty, C.M., *Synthesis gas production via catalytic partial oxidation reforming of liquid fuels*. International Journal of Hydrogen Energy, 2008. **33(19)**: p. 5012-5019.
15. Staniforth, J. and Ormerod, R.M., *Implications for Using Biogas as a Fuel Source for Solid Oxide Fuel Cells: Internal Dry Reforming in a Small Tubular Solid Oxide Fuel Cell*. Catalysis Letters, 2002. **81(1)**: p. 19-23.
16. Tao, X., Bai, M., Li, X., Long, H., Shang, S., Yin, Y. and Dai, X., *CH₄-CO₂ reforming by plasma - challenges and opportunities*. Progress in Energy and Combustion Science, 2011. **37(2)**: p. 113-124.
17. Timmermann, H., Sawady, W., Campbell, D., Weber, A., Reimert, R. and Ivers-Tiffée, E., *Coke formation and degradation in SOFC operation with a model reformat from liquid hydrocarbons*. 2008. p. B356-B359.

18. Walker, D.G. and Hadley-Coates, L., *Boudouard carbon an alternate to gasoline and diesel oil*. International Journal of Energy Research, 1988. **12**: p. 243-251.
19. Sasaki, K. and Teraoka, Y., *Equilibria in fuel cell gases II: The C-H-O Ternary Diagrams*. Journal of The Electrochemical Society, 2003. **150**(7): p. A885-A888.
20. Goodwin, D.G. *An Open-Source, Extensible Software Suite for CVD Process Simulation*. in *Proceedings of Chemical Vapor Deposition XVI and EUROCVI 14, Electrochemical Society*. 2003.
21. Murray, E.P., Tsai, T. and Barnett, S.A., *A direct-methane fuel cell with a ceria-based anode*. Nature, 1999. **400**: p. 649-651.
22. Rolle, A. and Irvine, J.T.S., *Electrical, Microstructural Properties and Sulphur Tolerance of Anodes for SOFCs*, in *7th European SOFC Forum*. 2006.
23. Dong, J., Cheng, Z., Zha, S. and Liu, M., *Identification of nickel sulfides on Ni-YSZ cermet exposed to H₂ fuel containing H₂S using Raman spectroscopy*. Journal of Power Sources, 2006. **156**(2): p. 461-465.
24. Sarantaridis, D., Rudkin, R.A. and Atkinson, A., *Oxidation failure modes of anode-supported solid oxide fuel cells*. Journal of Power Sources, 2008. **180**(2): p. 704-710.
25. Nehter, P., *A high fuel utilizing solid oxide fuel cell cycle with regard to the formation of nickel oxide and power density*. Journal of Power Sources, 2007. **164**(1): p. 252-259.
26. Wiberg, E., *Die chemische Affinität*. 2 ed. 1972, New York: W. de Gruyter Berlin.
27. Job, G. *Tabelle chemischer Potenziale*. [cited 27.07.2010]; Available from: http://job-stiftung.de/pdf/datensammlung/chem_pot.pdf.
28. *DoITPoMS Teaching and Learning Packages, Department of Materials Science and Metallurgy, University of Cambridge*. 2010 [cited 15.09.2010]; Available from: http://www.doitpoms.ac.uk/tlplib/ellingham_diagrams/ellingham.php.
29. Ellingham, H.J.T., *Journal of the Society of Chemical Industry*, London, 1944. **63**(125).
30. Metzger, P., *Ortsaufgelöste Charakterisierung von Festelektrolyt-Brennstoffzellen (SOFC) durch Messung betriebsrelevanter Größen entlang des Strömungsweges*, Doctoral thesis, 2010, Universität Stuttgart: Stuttgart.
31. Wagner, N., *Electrochemical power sources - Fuel cells*, in *Impedance Spectroscopy: Theory, Experiment, and Applications, 2nd Edition*, J.R.M. Evgenij Barsoukov, Editor. 2005, Wiley-Interscience.
32. Huang, Q.A., Hui, R., Wang, B.W. and Zhang, H.J., *A review of AC impedance modeling and validation in SOFC diagnosis*. 2007. p. 8144-8164.
33. Arbeitskreis K. Funke, *Impedanzspektroskopie*. 2002, Institut für Physikalische Chemie Münster: Münster.
34. *Basics & Applications*, in *Zahner Messsysteme Thales IM6 & IM6eX User Manual*. 2007: Kronach.
35. Macdonald, J.R. and Johnson, W.B., *Fundamentals of Impedance Spectroscopy*, in *Impedance Spectroscopy: Theory, Experiment, and Applications*. 2005, Wiley-Interscience: New York. p. 1-26.
36. Adler, S.B., Henderson, B.T., Wilson, M.A., Taylor, D.M. and Richards, R.E., *Reference electrode placement and seals in electrochemical oxygen generators*. Solid State Ionics, 2000. **134**(1-2): p. 35-42.

37. Winkler, J., Hendriksen, P.V., Bonanos, N. and Mogensen, M., *Geometric Requirements of Solid Electrolyte Cells with a Reference Electrode*. Journal of The Electrochemical Society, 1998. **145**(4): p. 1184-1192.
38. Adler, S.B., *Reference Electrode Placement in Thin Solid Electrolytes*. Journal of The Electrochemical Society, 2002. **149**(5): p. E166-E172.
39. Nie, H., Huang, W., Wen, T.-L., Tu, H. and Zhan, Z., *LSM cathodes for SOFC prepared by plasma spraying*. Journal of Materials Science Letters, 2002. **21**(24): p. 1951-1953.
40. Suzuki, T., Awano, M., Jasinski, P., Petrovsky, V. and Anderson, H.U., *Composite (La, Sr)MnO₃-YSZ cathode for SOFC*. Solid State Ionics, 2006. **177**(19-25): p. 2071-2074.
41. Zhang, C., Li, W.Y., Liao, H., Li, C.J., Li, C.X. and Coddet, C., *Microstructure and Electrical Conductivity of Atmospheric Plasma-Sprayed LSM/YSZ Composite Cathode Materials*. Journal of Thermal Spray Technology, 2007. **16**(5): p. 1005-1010.
42. Bessler, W.G., Gewies, S. and Vogler, M., *A new framework for physically based modeling of solid oxide fuel cells*. Electrochimica Acta, 2007. **53**(4): p. 1782-1800.
43. Gewies, S., *Modellgestützte Interpretation der elektrochemischen Charakteristik von Festoxid-Brennstoffzellen mit Ni/YSZ-Cermetanoden*. 2009, Ruprecht-Karls-Universität: Heidelberg.
44. Bessler, W.G. and Gewies, S., *Gas Concentration Impedance of Solid Oxide Fuel Cell Anodes*. Journal of The Electrochemical Society, 2007. **154**(6): p. B548-B559.
45. Bessler, W.G., Gewies, S., Willich, C., Schiller, G. and Friedrich, K.A., *Spatial Distribution of Electrochemical Performance in a Segmented SOFC: A Combined Modeling and Experimental Study*. Fuel Cells, 2010. **10**(3): p. 331 - 477
46. Gewies, S. and Bessler, W.G., *Physically based impedance modeling of Ni/YSZ cermet anodes*. Journal of The Electrochemical Society, 2008. **155**: p. B937-B952.
47. Bessler, W.G., *Hydrocarbon Direct Oxidation or Internal Reforming? A Critical Discussion from an Elementary Kinetic Viewpoint in 8th European Solid Oxide Fuel Cell Forum*. 2008: Lucerne, Switzerland.
48. Baumann, F.S., Fleig, J., Habermeier, H.-U. and Maier, J., *Impedance spectroscopic study on well-defined (La,Sr)(Co,Fe)O_{3-δ} model electrodes*. Solid State Ionics, 2006. **177**: p. 1071-1081.
49. Janardhanan, V.M. and Deutschmann, O., *CFD analysis of a solid oxide fuel cell with internal reforming: Coupled interactions of transport, heterogeneous catalysis and electrochemical processes*. Journal of Power Sources, 2006. **162**(2): p. 1192-1202.
50. Zhu, H., Kee, R.J., Janardhanan, V.M., Deutschmann, O. and Goodwin, D.G., *Modeling elementary heterogeneous chemistry and electrochemistry in solid-oxide fuel cells*. J. Electrochemical Soc., 2005. **152**: p. A2427-A2440.
51. Bessler, W.G., Warnatz, J. and Goodwin, D.G., *The influence of equilibrium potential on the hydrogen oxidation kinetics of SOFC anodes*. Solid State Ionics, 2007. **177**(39-40): p. 3371-3383.
52. Konyshva, E., Mertens, J., Penkalla, H., Singheiser, L. and Hilpert, K., *Chromium Poisoning of the Porous Composite Cathode*. Journal of The Electrochemical Society, 2007. **154**(12): p. B1252-B1264.
53. Brandt, C.M., *Oxidation und epitaktische Oxidation von Nickel und Nickellegierungen*. Doctoral thesis, 2002, Georg-August-Universität Göttingen.
54. Virkar, A.V., *A model for solid oxide fuel cell (SOFC) stack degradation*. Journal of Power Sources, 2007. **172**(2): p. 713-724.

55. DE Patent Application No. 10 2011 0530 550.0, unpublished (filing date Sep. 13. 2011)

Curriculum vitae

Caroline Willich,

born 18th March 1981 in Munich

- 05/2000 Bilingual (German, English) Abitur (university entrance qualification),
Immanuel Kant Gymnasium, Münster, Germany
- 10/2000-08/2001 Student of English and linguistics at the University of
Münster, Germany
- 10/2001-10/2003 Intermediate diploma of Mechanical Engineering (Technical University
of Munich, Germany)
- 10/2003-03/2005 Participation in a double degree program (TIME) in Mechanical
engineering, (Escuela Técnica Superior de Ingenieros Industriales,
Madrid, Spain)
- 04/2005-12/2006 Diploma of Mechanical Engineering, (Technical University of Munich,
Germany)
- Focus: Sustainable energy systems
- Flight propulsion and turbomachinery
- Diploma thesis: Analysis of the microstructure of a solid oxide
 fuel cell (SOFC)
- 01/2007-07/2012 Ph.D. work (Institute for Technical Thermodynamics, German
Aerospace Centre, Stuttgart, Germany)
- Topic: Local characterization of solid oxide fuel cells
- since 04/2011 Researcher at the Institute for Technical Thermodynamics, German
Aerospace Centre, Stuttgart, Germany
- Topic: Pressurized solid oxide fuel cells